Abstract

WARD, JR., LINTON BRIGGS. An Experimental Study of the $^{3}He(n,\gamma)^{4}He$ Reaction. (Under the direction of D. R. Tilley)

An investigation of fast neutron capture by ^{3}He has been undertaken. In an effort to resolve major discrepancies in the published values for the total $^{4}He(\gamma,n)^{3}He$ cross section, the 90^{o} cross section of the $^{3}He(n,\gamma)^{4}He$ reaction was measured for incident neutron energies ranging from 6.0 MeV to 18.0 MeV, corresponding to excitation energies of 25.1 MeV to 34.1 MeV in ^{4}He. These data when converted by the principle of detailed balance implies a total $^{4}He(\gamma,n)^{3}He$ cross section of ~ 1 mb throughout the energy region. This result agrees with the most recently published (γ,n) data, but is in disagreement with earlier published values. When combined with published $^{4}He(\gamma,p)^{3}H$ cross section data, a (γ,p) to (γ,n) cross section ratio is obtained which rises from ~ 1 at E_{x} = 34 MeV to ~ 1.8 at E_{x} = 25 MeV. This result is not predicted by current reaction theories as applied to this nucleus, and has been used by some authors to infer the existence of a Charge Symmetry Breaking component of the nuclear force. Comparison of this result is made to calculations using a) the direct model b) a direct-plus-charge-exchange model and c) a continuum-recoil-corrected shell model. Further calculations are needed to determine whether the Coulomb interaction is responsible or whether some component of the short range nuclear force produces this result.

Angular distributions of cross section and analyzing power were measured at a neutron energy of 9 MeV. The cross section was measured

at 7 angles and the analyzing power at 3 angles. An analysis was made based on the assumption that only S = 0,1 E1 and S = 0 E2 transition matrix elements contribute to the reaction. This analysis suggests that there is about the same relative S = 1 to S = 0 E1 strength for the $^{3}H(p,\gamma)^{4}He$ and the $^{3}He(n,\gamma)^{4}He$ reaction and that the E2 amplitude is about the same magnitude for both reactions.

AN EXPERIMENTAL STUDY

OF THE $^{3}He(n,\gamma)^{4}He$

REACTION

by

Linton B. Ward, Jr.

A thesis submitted to the Graduate Faculty of
North Carolina State University
in partial fulfillment of the
requirements for the Degree of
Doctor of Philosophy

DEPARTMENT OF PHYSICS

Raleigh

1 9 8 1

APPROVED BY:

_____ _____

_____ _____

Chairman of Advisory Committee

BIOGRAPHY

Linton Briggs Ward Jr., was born in Raleigh, North Carolina on January 5, 1953. He was reared in Richmond, Virginia and graduated from D. S. Freeman H. S. in 1971. He then attended Ferrum Colege in Ferrum, Virginia and received an A.S. degree in 1973. In 1975 he received a B.S. degree from Roanoke College. While at Roanoke, he served as a laboratory assistant. The lord Jesus Christ revealed himself to Linton during the summer of 1975. In August, 1976 he enrolled in a graduate program in Physics, taking a one-half time teaching assistantship and a part time internship with the Department of Human Resources of the state of North Carolina. Since 1978 he has held a research assistant from NCSU. In 1978 he was married to Michele Alice Struble, and now has one son.

ACKNOWLEDGEMENTS

Without the grace of the lord Jesus Christ, I would not have completed this project. I wish to thank my wife, Michele for her help and backing.

I would like to thank my advisor, Dr. D. R. Tilley for his encouragement and patient direction, and the members of the capture group, Drs. N. R. Roberson, H. R. Weller and S. A. Wender for their guidance and assistance. The help and discussion of Dr. Mark Jensen and Dr. Steve Manglos as well as the other graduate students is appreciated.

The help of Dr. S. Cotanch in providing the computer codes Radcap and Excap used in the analysis, Dr. H. Hasan for adapting Excap and performing the coupled-channels calculation, as well as Dr. P. P. Delsanto for the continuum shell model calculation, Dr. L. C. Biedenharn and R. Y. Cusson for discussions of the analysis is greatly appreciated.

The technical assistance of Mrs. Joseph Bailey in preparation of the figures and that of C. Floyd in photographing them is appreciated. The assistance of Mr. S. E. Edwards, Mr. R. L. Rummel and P. Carter is appreciated. I appreciate the patience and promptness of A. L. Lovette and the members of the instrument shop.

I gratefully acknowledge the assistance of Mr. Ed Morgan and members of the Duke Low-Temperature group in handling the liquid helium for target preparation.

This work was supported in part by the U. S. Department of Energy.

TABLE OF CONTENTS

LIST OF TABLES

LIST OF FIGURES

1. PHOTODISINTEGRATION OF SELF CONJUGATE NUCLEI

In the photo-absorption cross section of nearly all nuclei at energies above the particle separation threshold there is observed a large resonance-like structure whose properties are systematic in the nuclear mass, A. This corresponds mainly to the absorption of electric dipole (E1) radiation hence its name, Giant Dipole Resonance (GDR). The GDR comprises most of the dipole oscillator strength in a given nucleus.

For light nuclei ($A \leq 40$) the explanation of this phenomenon is based on the independent particle model (Wilkinson, 1956) in which the GDR corresponds to the promotion of a nucleon to the next opposite parity level in the shell model. Refinements (Elliot and Flowers, 1957; Brown et al., 1961) more nearly reproduce its features by including a residual interaction. For the 1s shell nuclei, the shape of the GDR is very smooth; presumably due to their low level densities and simplicity. In particular, the photodisintegration of ^{4}He is thought to procede through a single-particle excitation due to the few particles involved. In the present work, the photodisintegration of ^{4}He through the n-^{3}He channel has been studied by the radiative capture of neutrons by ^{3}He. This channel is the time-inverse of the photodisintegration process whose cross section

may be inferred with the use of the principle of detailed balance (eq. (6.1)). Neutron bombarding energies of 6 to 18 MeV corresponding to excitation energies of 25 to 34 MeV were used, allowing investigation in the GDR region. Angular distributions of cross section and cross section times analyzing power were measured at E_n = 9 MeV to deduce the transition matrix elements.

The motivation for this cross section measurement arises from the important implications which it holds for nuclear structure theory. The simplest model of this reaction would place equal strengths in the neutron and proton decay channels. Some photoneutron experiments have cast doubts as to their equality, but problems of a technical nature made some of these experiments suspect. Any explanation of this inequality must embrace the simplicity of the A=4 system, yet a possible explanation arises from the effect which is seen in heavier nuclei where the coulomb force is responsible for the isospin mixing in the states which comprise the GDR. ^{4}He is one of a class of self conjugate nuclei (N=Z) which plays an important role in the development of the theory of isospin.

Since the photonuclear cross section is dominated by the GDR, selection rules for radiative transitions from the ground state of self conjugate nuclei provide a test of the isospin mixing in the resonance region. These nuclei with generally pure ground state wave functions ($J^\pi = 0^+$, T = 0) have giant resonances with a spin assignment of 1^- and T = 1. The selection rule for a dipole transition is $\Delta T = 1$ as is evident when one writes the operator in the isospin formalism (eg. Eisenberg and Greiner, 1970). The presence of

broad, underlying T = 0 strength can mix with the T = 1 resonance for a variety of reasons and produce observable effects.

The concept that the nuclear Hamiltonian is nearly charge independent is central to nuclear structure analysis. Components which do not preserve isospin lead to violations of the selection rules which are imposed on reactions. Nuclear wave functions may have components which have a different total isospin quantum number. Interactions which mix wave functions of good isospin are outlined by Warburton and Weneser (1969). By far, the largest isospin-violating potential is that of the Coulomb interaction; smaller factors are present, introduced by the neutron-proton mass difference and even possibly the nucleon-nucleon interaction. Because of its long range effect, the Coulomb interaction produces the greatest isospin mixing which has been observed. Generally an analysis of isospin-violating phenomena centers on whether or not the coulomb interaction is capable of producing that effect. Warburton and Weneser show that mixing in the excited state governs the admixture in a given (E1) transition to the ground state. For narrow, isolated resonances where first order perturbation theory is applicable the mixing of T = 1 and T = 0 states due to the coulomb interaction is inversely proportional to the energy difference. So isospin mixing is expected to be greater for excited states than for the ground state.

In the case of photonuclear reactions, Barker and Mann (1957) stated that a T = 0 admixture in the predominantly T = 1 giant dipole resonance of a self-conjugate nucleus could lead to a large difference in the proton and neutron emission from the constituent state or

states. The amount of mixing would be difficult to determine from radiative transitions or reactions involving T = 0 particles since the amplitudes involve the squares of the mixing coefficients. For neutron and proton emission from self-conjugate nuclei the mixing coefficients enter linearly into the transition amplitudes. They point out additionally that reactions such as (d,p) or (d,n) would not be useful as stripping contributions would mask this compound nuclear effect. They claim that the GDR is a good candidate for a study of isospin mixing. It is expected that mixing would be greater for states of higher excitation since the mixing is dependent on the proximity of states of isospin T = 0. In the GDR region, the radiation is predominantly E1; other multipoles could excite both T = 1 and T = 0 states which could cause interference. Of course the interference from other multipoles would appear in the differential but not in the integrated cross section.

The relationship between the transition probabilities for neutrons and protons was obtained by operating on the ground state (oscillator) wave function with the electric dipole operator. Then, after introduction of a T = 0 component of the wave function, the cross section for proton and neutron emissions was obtained. The phase of the Clebsch-Gordan coefficients causes the isospin amplitudes to add in the case of proton emission and subtract in the case of neutron emmision so that the ratio of these cross sections is

$$\frac{\sigma(\gamma,p)}{\sigma(\gamma,n)} = \frac{P_p}{P_n}\left|\frac{a_1 + a_0}{a_1 - a_0}\right|^2 \qquad (1.1)$$

Where α_T is the amplitude for the isospin T = 0,1 component of the wave function and P_p, P_n are the proton and neutron penetrabilities respectively. Since the coefficients add linearly, this ratio is very sensitive to the isospin mixed amplitude; a 3% T = 0 component in the dominant T = 1 wave function would produce a (γ,p) to (γ,n) cross section ratio R = 2 if the penetrabilities were equal.

A review of the application of this formula to various light self-conjugate nuclei is presented by Segel (1966) who tabulates the experimental results. This is represented in figure 1-1; the ratio of the integrated (γ,p) to (γ,n) cross sections is seen to increase with increasing A. An explanation of this feature is that the coulomb mixing of the states which comprise the GDR increases with A (or Z). The figure indicates clearly that the value of this ratio should be small for the lightest self-conjugate nucleus ^{4}He.

In some respects the photodisintegration of ^{4}He is an ideal case to test equation (1.1), however, the difficulty is that a direct process accounts for nearly all of the cross section. This is discussed in section 2.2. States which could be said to comprise the GDR in ^{4}He are inferred from particle scattering phase shifts; the analysis of the ^{3}He$(p,\gamma)^4$He reaction (King, 1978) also gives information on this. In the energy region 25 - 31 MeV, there are 3 1^- states, two of which are T = 1. The lower T = 1 state is thought to contain most of the strength seen in E1 decay to the ground state. It must be stated, however, that these states are very broad and overlap with other levels. They are observed through the energy dependence of

Figure 1-1 Ratio of integrated photoproton to photoneutron cross sections of self conjugate nuclei. Data are from the review of Segel (1966).

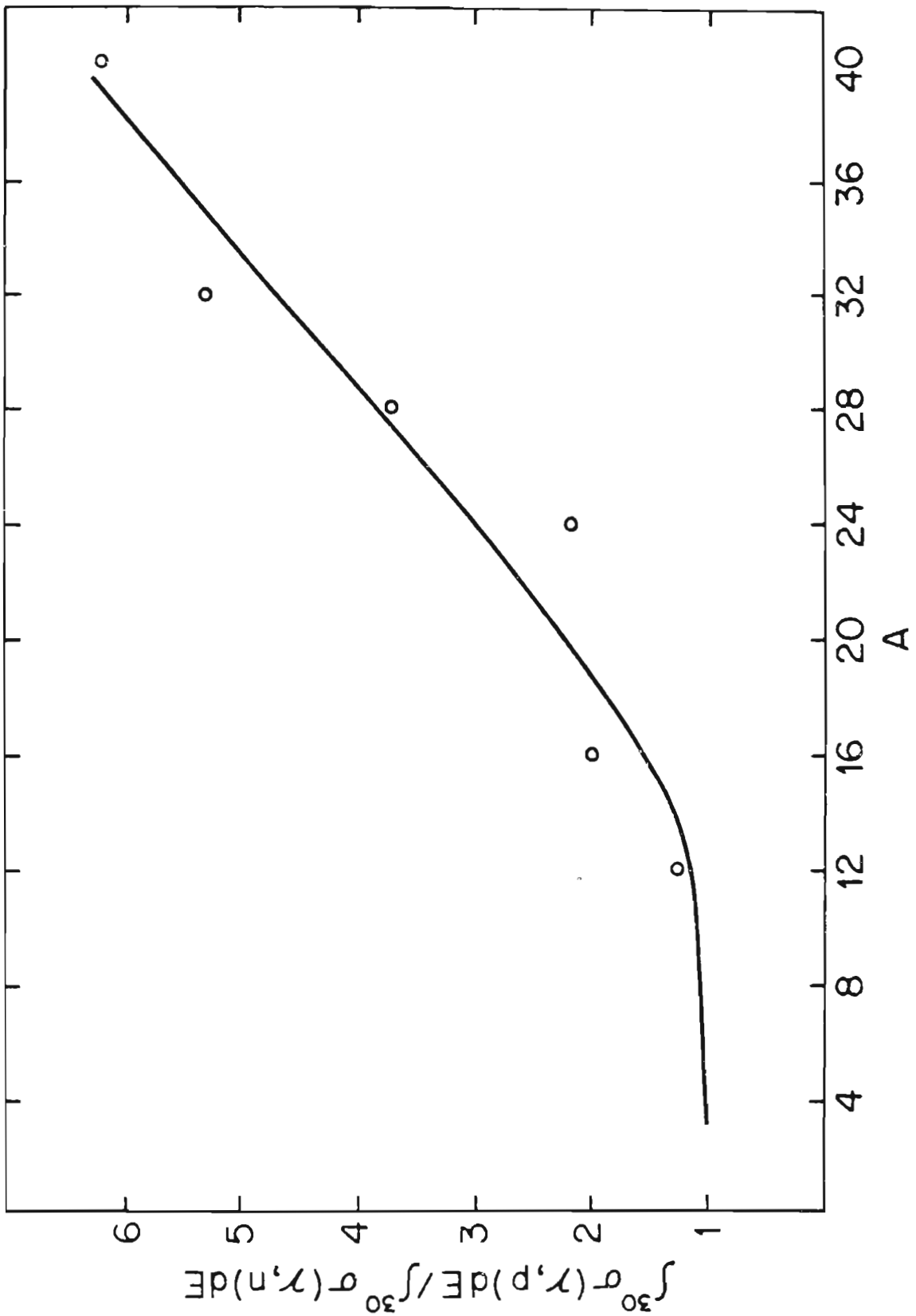
$\int^{30}\sigma(\gamma,p)dE/\int^{30}\sigma(\gamma,n)dE$
1
2
3
4
5
6
4
8
12
16
20
24
28
32
36
40
A

the phase shifts (Fiarman and Meyerhof, 1973). The photodisintegration of ^{4}He is consistent with the existence of a broad (~5 MeV) 1^- T = 1 state located at E_x = 28 MeV. This T = 1 state and the nearby T = 0 state overlap; this could lead to a high degree of mixing. A prediction of the ratio of proton to neutron emission from this state based on this evidence would not necessarily indicate a value of one.

Other effects which could lead to differences in proton and neutron emission are the purity of the ground state wave functions of ^{3}H, ^{3}He and ^{4}He. These are believed to be isospin states having T = 1/2, 1/2 and 0 respectively.

2. PHOTODISINTEGRATION OF ^{4}He

Inasmuch as the photodisintegration of ^{4}He is expected to proceed through a relatively simple mechanism and bears great implications on the understanding of nuclear structure, the experimental controversy over the magnitude of the $^4He(\gamma,n_0)^3He$ cross section has sparked intense theoretical interest and has been followed closely. While the photoproton cross section has a fairly well agreed upon value the photoneutron cross section has had a rather colorful history. In the period of 1970 to the present there have been ~ 10 measurements, most of which fall into two groups; those which indicate near equality with the (γ,p) cross section and those which indicate a value which is approximately one-half of the (γ,p) cross section. There have admittedly been experimental difficulties which obscured the problem but there also exists some truly contradictory experimental evidence. Of course, one can not hope to evaluate the merits of all these experiments in detail, but at least a brief review will help to clarify the situation. Table 2-1 contains a partial listing of the experimental approaches; some of the material is from similar compilations in Malcolm (1972) and McBroom (1977). The photoproton and inverse data are presented first since they exhibit a higher degree of consistency. The photoneutron data are then reviewed. Some

Table 2-1 Summary of photodisintegration experiments.

Reference	Excitation Energy (MeV)	Source (Range)	Target	Detector	Angle	Maximum σ_T (mb)
(p,γ)						
Perry and Bame, 1955	20 - 24			NaI	Dist (90°)	1.8
Gemmel and Jones, 1962				NaI	Dist	1.8
Gardner and Anderson, 1962	24 - 27			NaI	Dist	1.8
Meyerhoff et al., 1970	22 - 34			NaI	Dist (90°)	1.8
(γ,p)						
Fuller, 1954	21 - 40				Dist	1.8
Milone, 1960	23 - 32	Annih (32)		Emulsions	90°	1.8
Sanada et al., 1970	23 - 32	Brems (32)		Emulsions	Dist	1.7
Clerc et al., 1965	24 - 56	Brems (40-60)		S. St.	90°	1.7
Arkatov et al., 1971	20 - 120	Brems (20-120)		Cloud Ch.	Dist	1.8
(n,γ)						
Zurmühle et al., 1963	24		Gaseous			

Table 2-1 Continued

Reference	Excitation Energy (MeV)	Source (Range)	Target	Detector	Angle	Maximum σ_T (mb)
(γ,n)						
Ferguson et al., 1954	20 - 26	Brems	Gaseous	BF_3	90^o	1.3
Ferrero et al., 1966	20 - 80	Brems (20-80)	Gaseous	BF_3	4π	1.3
Berman et al., 1971	20 - 31	Annih	Liquid	BF_3	4π	0.9
Berman et al., 1972	22 - 32	Brems (35)	Liquid	n-TOF	90^o	1.0
Malcolm et al., 1973	24 - 72	Brems (110)	Liq/Gas	n-TOF	Dist	2.1
Irish et al., 1975	22 - 32	Brems (22-33)	Liq/Gas	n-TOF	Dist	1.65
Berman et al., 1980	20 - 47	Annih	Gaseous	BF_3	4π	1.1
(γ,p) and (γ,n) or Ratio						
Gorbunov and Spiridonov, 1958 Gorbunov and Spiridonov, 1968	22 - 260	Brems (170/260)		Cloud Ch.	Dist	p - 1.7 n - 1.6
Balestra et al., 1977	25 - 80	Brems (80)		Cloud Ch.	Dist	p - 1.7 n - 1.35
Busso et al., 1971	25 - 80	Brems (80)		Cloud Ch.	Dist	p - 1.8 n - 1.1

Table 2-1 Continued

Reference	Excitation Energy (MeV)	Source (Range)	Target	Detector	Angle	Maximum σ_T (mb)
(γ,p) and (γ,n) or Ratio						
Dodge and Murphy, 1972	30 - 52	90 MeV e	Gaseous	Mag. Spect	^3H, ^3He $\theta_{LAB}=90^o$	
Arkatov et al., 1978	20 -150	Brems	Gaseous	Cloud Ch.	Dist	p - 1.7 n - 1.3
Phillips et al., 1979	31 - 51	Brems (56)	Gaseous	S. St.	^3H, ^3He $\theta_{LAB}=90^o$	

of these experiments were performed as ratio measurements in which only the relative cross sections were reported; others report an absolute cross section for both reactions which were measured nearly simultaneously. Systematic errors will cancel in a ratio formed in this manner. Theoretical approaches to these reactions are considered last.

2.1 Experimental

Possibly the highest precision value of the photoproton cross section is derived using radiative capture data and the principle of detailed balance (eq. 6-1). Perry and Bame (1955) presented precision measurements up to E_γ = 24 MeV; the work of Meyerhof *et al.* (MSF) extends the measurement to higher energies. The deduced value of the cross section agrees well with the measurement of photoproton cross sections. The early work of Gorbunov is in agreement with these data, and inspection of the results which are tabulated indicates the general agreement as to the shape and magnitude of the cross section.

The photoneutron cross section has presented the greatest experimental difficulty. Several reviews of this situation have been given, a recent one is presented in Phillips *et al.* (1979). Even some of the earliest work hinted at a discrepancy (Ferguson, 1954) in which the highest value of the (γ,n) cross section was ~ 30% less than that reported for (γ,p). The sole capture measurement also indicated a low value (Zurmühle *et al.*, 1963). However, attention was focused on

these cross sections when Berman, Fultz and Kelly (1971) (BFK) reported a total photoneutron cross section measurement which was approximately one-half of the photoproton cross section at all energies (Threshold to 31 MeV), and suggested that this result was due to isospin mixing in the GDR region. This result was supported by the $\sigma(90^{o})$ (n-TOF) measurement by Berman, Firk and Wu (1972) (BFW) except that the latter cross section at higher energies (>30 MeV) remained nearly constant, almost approaching the (γ,p) value. The BFK result seemed to simply have a normalization error, but the BFW result indicated that possibly a different shape described the neutron data. Malcolm et al. (1973) also reported a low value. The validity of these results was questioned when Irish et al. (1975) found that the photoneutron yield varied with beam current due to bubbling in the liquid helium target. This problem possibly would hamper all of these measurements except those of BFK who used a liquid target, but had low beam currents.

Meanwhile, other groups using cloud chambers reported measurements of these cross sections which indicated that the ratio of the photoproton to the photoneutron cross section, R was greater than one for energies less than $\simeq$ 31 MeV. The total photoneutron cross section measured by the Torino group with a thermalized neutron detector was slightly lower than the (γ,p) cross section below 28 MeV (Ferrero et al., 1966). They then measured the cross sections simultaneously using a cloud chamber. The preliminary results (Busso et al., 1971) indicated that the ratio, R was significantly greater than one for $E_{\gamma} < 28$ MeV, and $R \simeq 1$ for $E_{\gamma} > 30$ MeV. The latter

results are reported in BBB, the value of R in the region of the peak (< 30 MeV) in apparent agreement with the results of Arkatov et al. Simultaneous measurement of these cross sections by Arkatov et al. (1976, 1978) indicated that the photoneutron cross section was lower than the photoproton cross section below E_γ = 32 MeV.

Measurements of the ratio, or measurements of both (γ,n) and (γ,p) cross sections simultaneously, indicate that they are nearly equal down to $E_\gamma \simeq 34$ MeV. The major discrepancy is in the region of 24 to 34 MeV in excitation energy. The cross section ratio presented by BFK seemed to be inconsistent with the measurements above 34 MeV; a sharp discontinuity would be required to reconcile them. At these lower energies, the cloud chamber experiments suffer problems because of the short range of the recoiling ^3H and ^3He. Other measurements (Dodge and Murphy, 1972; Phillips et al., 1979) have similar problems below ~ 34 MeV, but indicate that R is ~ 1 for E_γ > 34 MeV. The most recent total photoneutron cross section measurement (Berman et al., 1980) yields a value of ~ 1 mb throughout the energy region of 24 to 34 MeV.

2.2 Theoretical

The earliest theoretical approach to the two body photodisintegration of ^4He was in the form of a direct-capture calculation using Gaussian and Exponential wave functions (Gunn and Irving, 1951; Flowers and Mandl, 1950). The general features of the

$^4He(\gamma,p)^3H$ cross section were reproduced leading to the claim that the reaction was primarily direct, proceeding through a single nucleon. There were problems however, namely the inability of the calculation to obtain the proper peak position while maintaining the experimentally determined charge distribution. This problem is reviewed by Dixon (1960) who states that two-particle correlations in the α particle wave function may alleviate these problems. Whatever the cause for disagreement, it seems that the consensus was that the wave functions were inadequate.

When in 1972 experimental evidence was produced which indicated that the $^4He(\gamma,n)^3He$ cross section was only half of $^4He(\gamma,p)^3H$ cross section, a number of calculations were performed to try to explain that result. Subsequent experimental controversies tended to quench the theoretical effort, however and to date there is no mechanism which has been applied to this reaction which reproduces that experimental discrepancy. The shell-model calculation of Gibson (1972) produces this ratio but only when components of different channel spins were allowed to interfere. In an attempt to explain the $R > 1$ result, Londergan and Shakin (1972) included charge dependent effects in a continuum shell model calculation but to no avail. Their value for R is ~ 1 near 26 MeV; it rises dramatically at lower energies because of threshold effects. Similarly, the continuum calculations of Chung et al. (1974), Delsanto et al. (1977) and Halderson and Philpott (1977) produce general agreement with the experimental (γ,p) cross section, and a ratio of ~ 1 above 24 MeV.

3. EXPERIMENTAL APPARATUS

The measurements in this study were performed with the neutron capture facility which has been developed at TUNL. deuterons incident upon a gaseous Deuterium target provided the fast neutron flux via the $^{2}H(d,n)^{3}He$ reaction. The target mounted at 0^{o} with respect to the incident beam and coincident with the center of rotation of the γ-spectrometer allowed angular distributions involving the (n,γ) and $(\vec{n},\gamma)$ reactions to be measured.

3.1 Deuteron Beam

For the yield curve and $\sigma(\theta)$ measurements, the deuteron beam was produced by the Direct Extraction Negative Ion Source (DENIS II). The beam was pulsed with an RF chopping and bunching system. A pulse width of ~ 2 nS was typical with a repetition rate of 2 Mhz. and a RMS intensity of of ~ 500 nA on target.

Polarized deuterons were produced by the TUNL Lamb-shift polarized ion source for the $A(\theta)$ measurement. Descriptions of this type of source have been given (Clegg et al., 1974; Ohlsen, 1970), and a detailed description of the operational mode for the production

of polarized neutrons via the $^2\vec{H}(\vec{d},n)^3He$ reaction has also been given (Lisowski, 1973). Selection of the deuteron hyperfine state $m_I = +1$ in the spin filter cavity allowed alignment of the deuteron spin along the beam direction. The spin direction remained unchanged while the beam was deflected thru 90^o. Subsequent precession of the spin direction allowed alignment of the spin in either the up or down direction. Typical vector and tensor polarizations of $p_3 = p_{33} = 0.7$ were obtained as measured on target by the DC Quench technique. Source operation was monitored to prevent any charged beam in the spin filter cavity which would give an erroneous deuteron beam polarization measurement. The polarized beam was not pulsed; the beam intensity was typically 100 - 200 nA.

The beams were accelerated with the TUNL FN model Tandem Van de Graaff accelerator, providing beams which ranged in energy from 3.5 to 15.5 MeV. A pair of 90^o bending magnets was used to momentum analyze the beam insuring a well defined deuteron energy. The beam was transported to the target with the use of electromagnetic steerers and quadrupole lenses.

3.2 Neutron Beam

A large and rather precisely determined cross section has made the $^2H(d,n)^3He$ reaction well suited as a source of fast neutrons for particle reaction studies. Figure 3-1 shows a time of flight spectrum of the neutrons produced at 0^o. The peak corresponds to neutrons from

Figure 3-1 TOF spectrum from 0^{o} monitor. Gamma-ray peak is suppressed by PSD. The continuum is from break-up reactions.

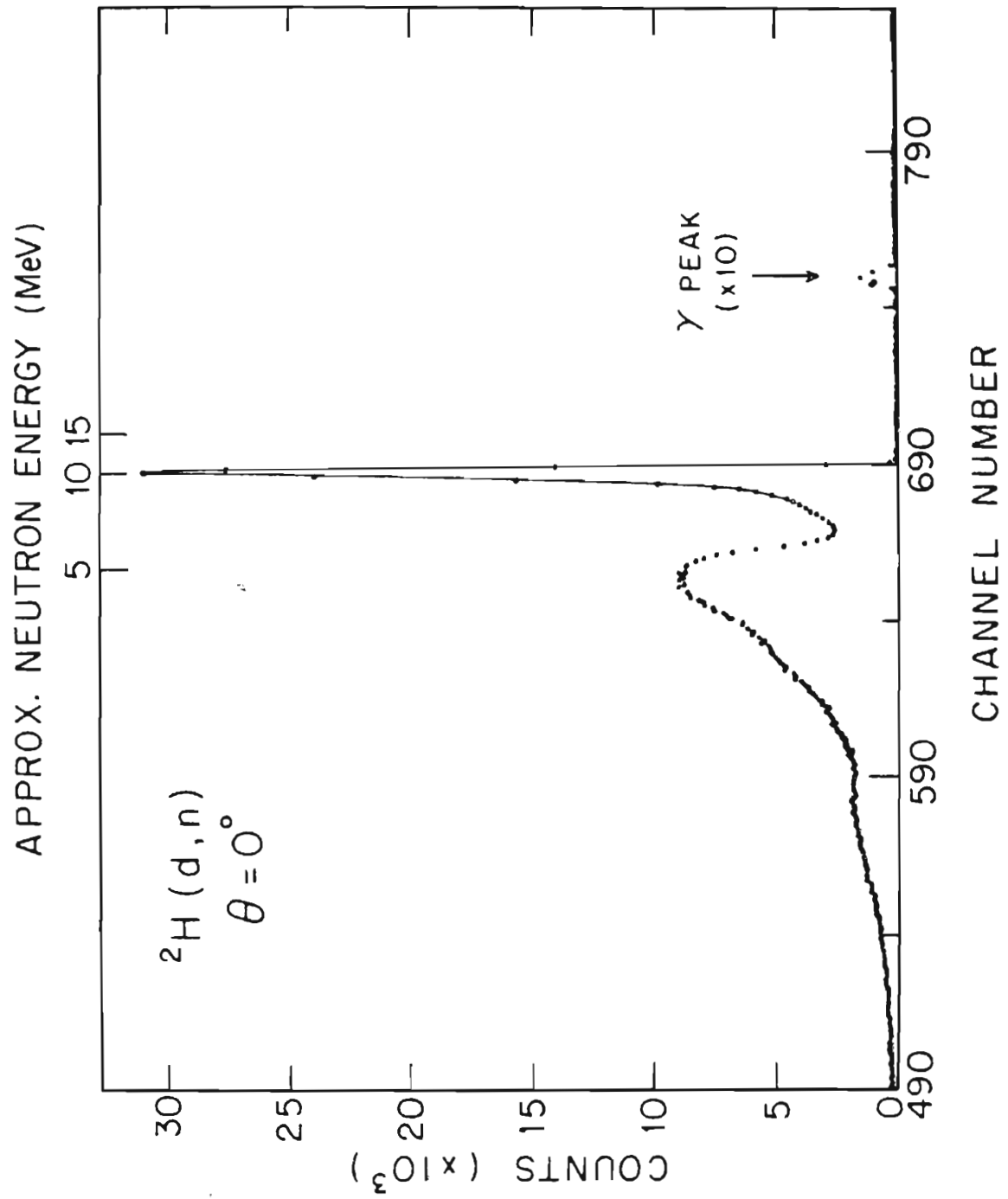
APPROX. NEUTRON ENERGY (MeV)
5
10
15
$^2H(d,n)$
$\theta = 0°$
γ PEAK
(x10)
COUNTS (x10³)
30
25
20
15
10
5
0
490
590
690
790
CHANNEL NUMBER

the $^{2}H(d,n)^{3}He$ reaction, and the continuum is from breakup reactions. Hence, the neutron spectrum is not monoenergetic, but the portion of interest is separated in energy from the continuum at forward angles by the kinematics and Q-value of the reaction. Reaction kinematics also dictate that the cross section as well as the energy of neutrons produced vary as a function of angle. Figure 3-2 depicts the dependence of the differential cross section on scattering angle in the lab frame; the angle at which the lab cross section is one half of the 0^{o} cross section is $(\theta_{1/2}) = 15.6^{o}$ at this energy $E_{n}(0^{o}) = 9$ MeV This half angle is a function of energy and ranges from $\sim 10^{o}$ at $E_{n}(0^{o}) = 6$ MeV to $\sim 6^{o}$ at $E_{n}(0^{o}) = 18$ MeV. Some indication of the energy variation of the neutrons with angle is given by comparing $E(\theta_{1/2})$ with the energy of the 0^{o} neutrons. At $E_{n}(0^{o}) = 6$ MeV, $E_{n}(\theta_{1/2})$ = 60 keV less than $E_{n}(0^{o})$, similarly at $E_{n}(0^{o}) = 18$ MeV $E(0^{o}) - E(\theta_{1/2}) = 100$ keV. This variation over the target is less than other sources of neutron energy spreading which will be discussed later. For reference, the target subtends an angle of $\sim$ 26 degrees. Another favorable feature of this reaction is that the pertinent quantity $\sigma(\theta,E)$ is a smooth, slowly varying function of energy. The zero degree cross section as a function of energy is presented in figure 3-3. Indeed, it has a structureless shape, well suited for a neutron source. The error in this quantity is discussed in section 4.1. If a Legendre polynomial fit is made to $\sigma(\theta)$, the coefficients are also slowly varying functions of energy, allowing interpolation in energy.

Figure 3-2 Differential cross section as observed in laboratory frame for $^{2}H(d,n)^{3}He$ reaction. The dashed line represents the angle subtended by the target.

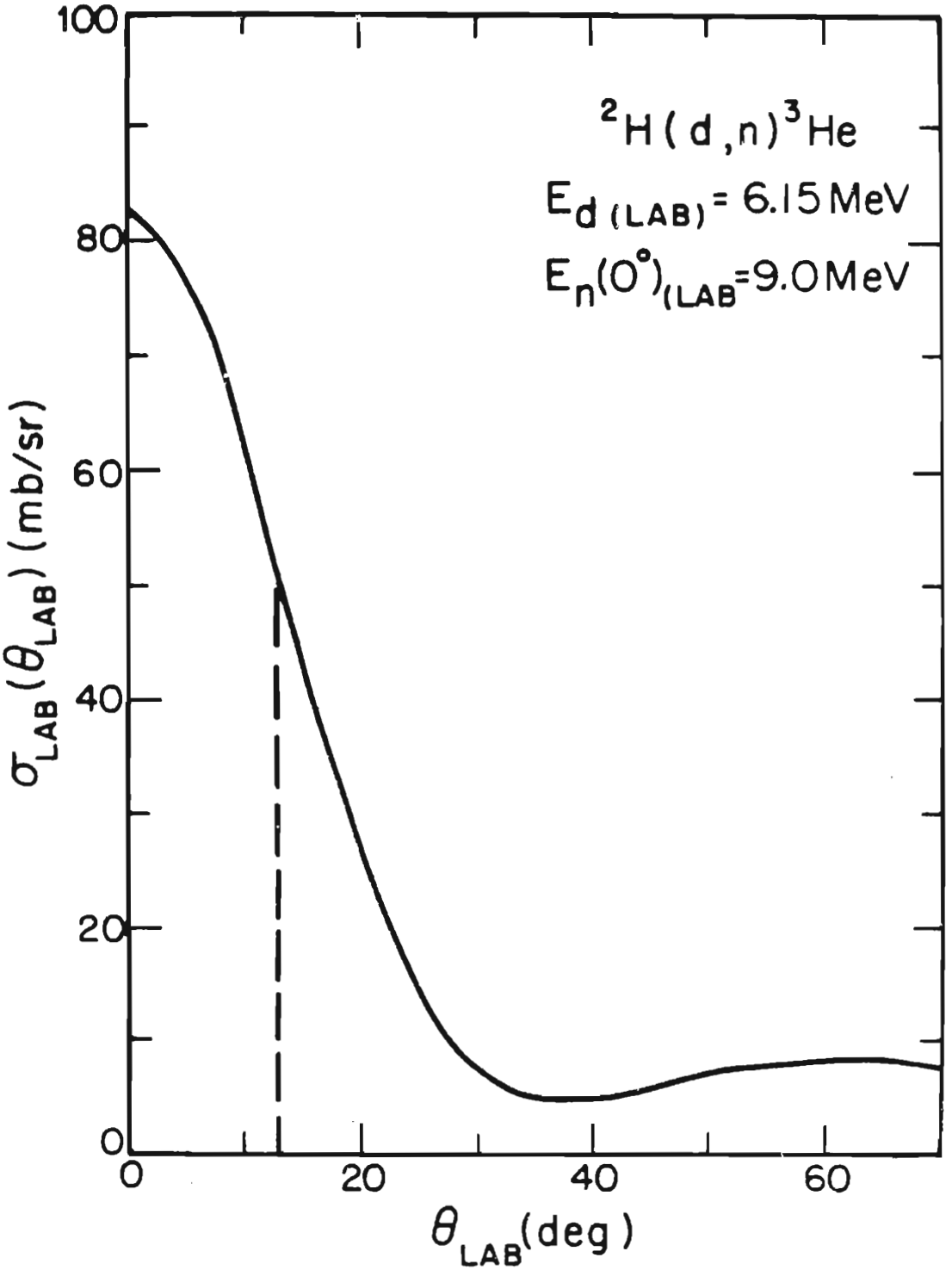
$^2H(d,n)^3He$
$E_{d\,(LAB)} = 6.15\,MeV$
$E_n(0°)_{(LAB} = 9.0\,MeV$
$\sigma_{LAB}(\theta_{LAB})$ (mb/sr)
θ_{LAB}(deg)
0
20
40
60
80
100

Figure 3-3 Zero-degree cross section as observed in laboratory frame for the $^{2}H(d,n)^{3}He$ reaction. The energy of the outgoing neutrons is indicated along the top axis.

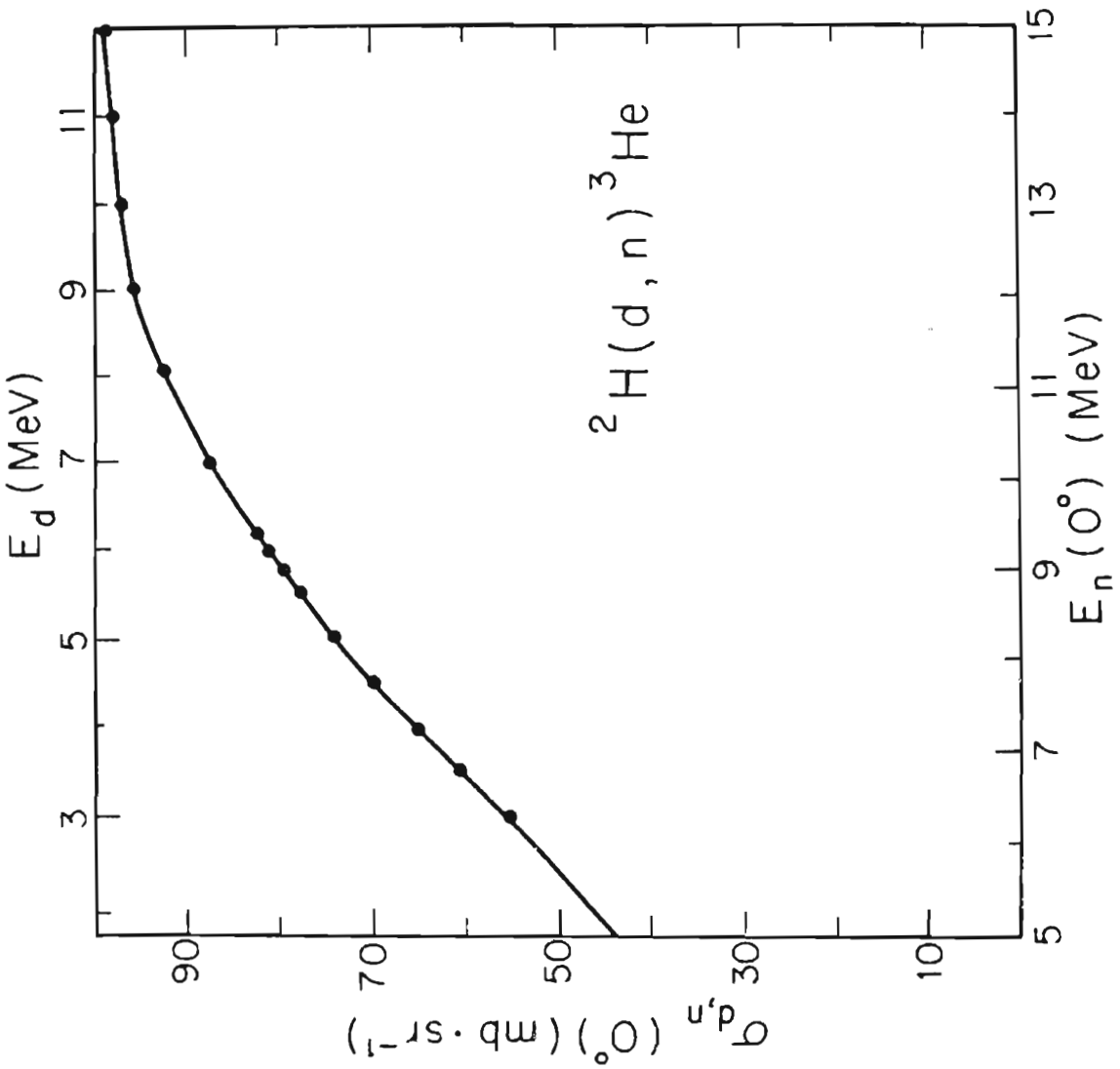
$^2H(d,n)^3He$
E_d (MeV)
$E_n(0°)$ (MeV)
$\sigma_{d,n}$ $(0°)$ (mb · sr^{-1})
3
5
7
9
11
5
7
9
11
13
15
10
30
50
70
90

This reaction is suited for polarized neutron capture in that the transfer polarization is large, and is nearly constant as a function of energy. Lisowski et al. (1975) have measured the 0^{o} transfer polarization in the energy region of interest. For a deuteron beam with its spin in a direction which is transverse to the beam direction, the neutron polarization at zero degrees is given by:

$$P_{y'}(0^{o}) = \frac{\frac{3}{2}p_3 K_y^{y'}(0^{o})}{1-\frac{1}{4}p_{33}A_{zz}(0^{o})}$$

where p_3 and p_{33} refer to the vector and tensor polarization with respect to the quantization axis at the polarized ion source, K_y^y is the vector polarization transfer coefficient, and A_{zz} is a tensor analyzing power. $A_{zz}(0^{o})$ was found to be a constant (-0.461) as a function of energy above E_d = 3 MeV; K_y^y was parameterized as

$$K_y^y(0^{o},E_d) = 0.6624 - 0.0032E_d.$$

Thus, for $p_3 = p_{33}$ $P_y(0^{o}) = 0.966/(\frac{1}{p_3} + 0.115)$ at $E_n(E_d)$ = 9(5.8) MeV. The polarization across the target is assumed to be constant, but a recent measurement (Tornow et al., 1981) indicates that this is not the case. However the effective variation in P_y, as a function of angle is smaller than our error. This has been verified empirically by the use of the $^{12}C(n,n')$ reaction (Jensen et al., 1979).

The gaseous deuterium target was developed to allow relatively high pressures to be used, and to provide a dependable entrance foil mounting. Figure 3-4 shows the cell and inductive time pickoff unit.

Figure 3-4 Neutron production cell and inductive time pickoff.

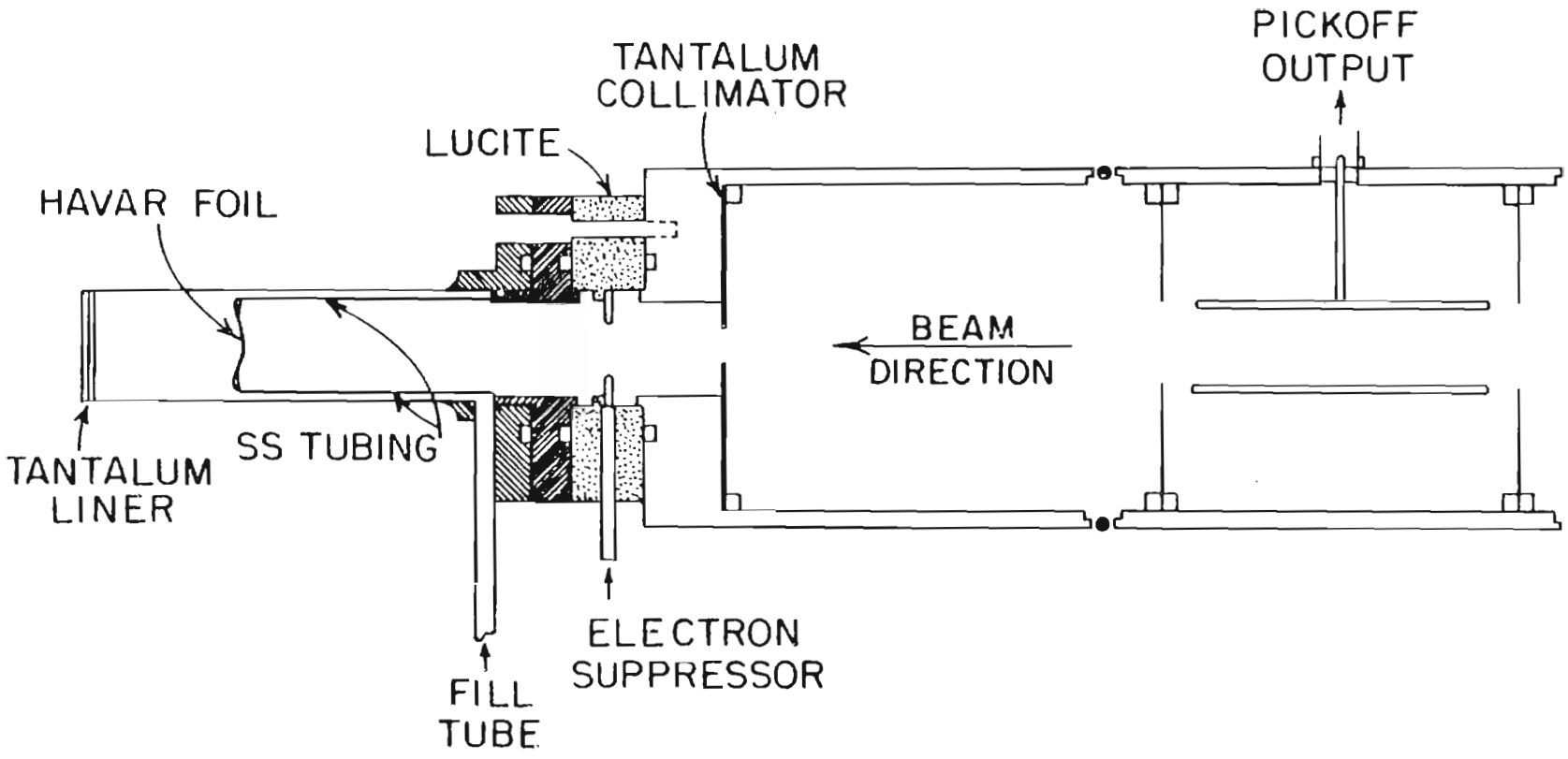
PICKOFF
OUTPUT
TANTALUM
COLLIMATOR
LUCITE
HAVAR FOIL
BEAM
DIRECTION
TANTALUM
LINER
SS TUBING
ELECTRON
SUPPRESSOR
FILL
TUBE

A beam pulse moving through the pickup induces a charge on the tube. Hence a small pulse is produced and is amplified by high gain preamplifiers. A collimating aperture defines the beam size and prevents the beam from striking the foil holder. Good charge integration is assured by the electron suppression ring which is kept at -500 V, and by the well-shaped foil holder. This combination serves as an efficient Faraday cup from which no secondary electron current is observed. The 5.6 μm Havar entrance foil is fastened to the holder with epoxy. This arrangement has allowed a deuterium pressure of 6 ATM to be maintained continuously for two weeks of running. The beam is stopped in a 760 μm end cap liner, which is changed periodically to prevent any significant accumulation of deuterium driven into the tantalum. Stainless steel construction allows the system to be kept clean. The gas handling system is also stainless steel with a liquid Nitrogen trap. Deuterium gas is supplied as research grade and has a purity of 99.9%. This cell has the advantage that there is not a high concentration of mass surrounding the region of neutron production, thus reducing the number of multiply-scattered neutrons. As the deuterons traverse the cell, they lose energy so that the neutrons produced via the $^{2}H(d,n)^{3}He$ reaction have a spread in energy. This spread is the dominant source of neutron energy spread at the target. This energy spread is nearly uniformly distributed, corresponding to a deuteron energy loss of 760 keV at $E_n(0^o)$ = 6 MeV, and 170 Kev at $E_n(0^o)$ = 18 MeV, for a one inch cell at 6 atmospheres cell pressure. A computer code used to calculate the energy loss was based on fits to energy loss data of

Barkas and Berger (1964). Effects of the energy loss of the beam in the entrance foil are also taken into account. The construction allows a rather precise alignment of the cell as well as an accurate determination of the target thickness which is important in neutron flux calculations. (see section 4.2)

3.3 ^{3}He Target

The high pressure gas target vessel design was based on a design used (Walter, 1979) for Helium scintillators. Figure 3-5 shows the pressure vessel along with the Deuterium cell, indicating their relative alignment. The vessel was machined from a single piece of type 304 stainless steel; the bottom flange was Heli-arc welded to the top. The dome shape allows even distribution of stress over the top; a sharp corner would fracture. The wall thickness was 1.6mm. Stress analysis of the wall indicates that there is a bursting safety factor of ~ 4; nevertheless care was exercised to prevent the cell from fracturing.

High purity, research grade ^{3}He was obtained from Mound labs in one-half liter cylinders at a pressure of ~ 400 psi. The quoted purity was 99.9%. A cryogenic pumping technique was used to attain relatively high target pressures without contaminating the ^{3}He gas. A small volume trap containing activated charcoal was cooled to liquid Helium(4) temperature, then the ^{3}He was allowed to enter from the cylinder and condense on the charcoal. The cylinder was valved off

Figure 3-5 Neutron production cell and target cell.

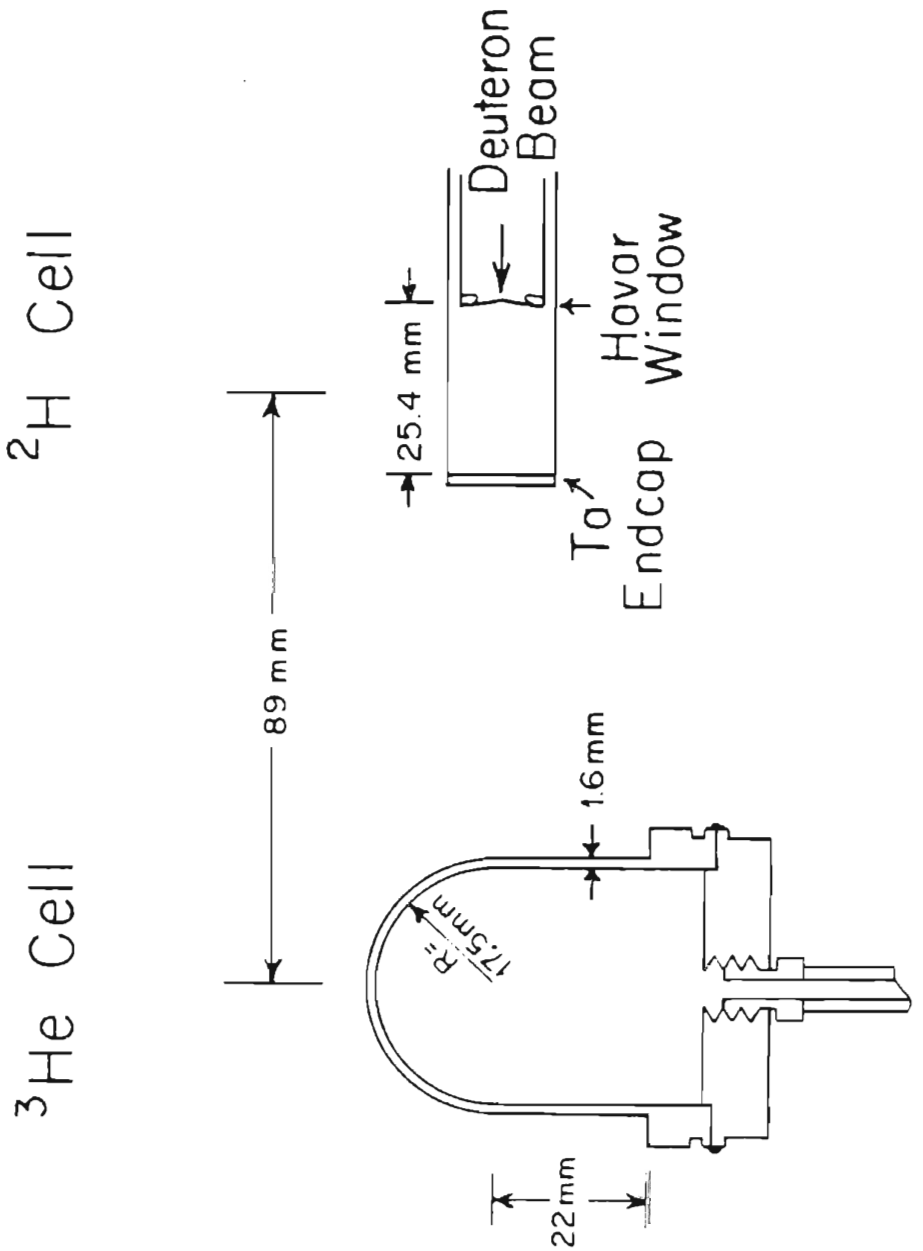
^{2}H Cell
^{3}He Cell
89 mm
25.4 mm
Deuteron Beam
Havar Window
To Endcap
1.6mm
R= 17.5mm
22mm

and upon warming, the gas was allowed to enter the target vessel. An increase in pressure resulted from the difference in volumes. In order to achieve a target pressure of ~ 2000 psia, two cycles and ~ 0.75 ℓ of supply gas were required to fill the 40.0 cm^3 vessel.

3.4 Detectors

A diagram of the spectrometer is shown in figure 3-6. Its relation to the neutron source and target is also shown. The center detector is a 24cm x 24cm NaI crystal. It is shielded from the intense flux from the $^2H_2$ gas cell as well as multiply scattered neutrons. Primary shielding from the gas cell is provided by the tungsten shadow bar which prevents neutrons and gammas from entering directly through the aperture in the lead shielding. Moderation and capture of neutrons is provided by the paraffin doped (50% by weight) with lithium carbonate which surrounds the assembly. A 1/8 inch sheet of cadmium supplies additional shielding from thermal neutrons on the front face. Finally γ-ray attenuation is provided by the four inches of lead shielding which surround the front and sides of the detector. The aperture in the Pb shield defines the solid angle which the detector subtends such that a point source at the center of the target would illuminate the full rear face of the NaI crystal. The effective acceptance angle of this system is ~ 18^o. Active shielding is provided by operating the well-shaped plastic scintillator in anticoincidence with the NaI detector. The NE-110 scintillator is

Figure 3-6 Diagram of spectrometer viewed from above.

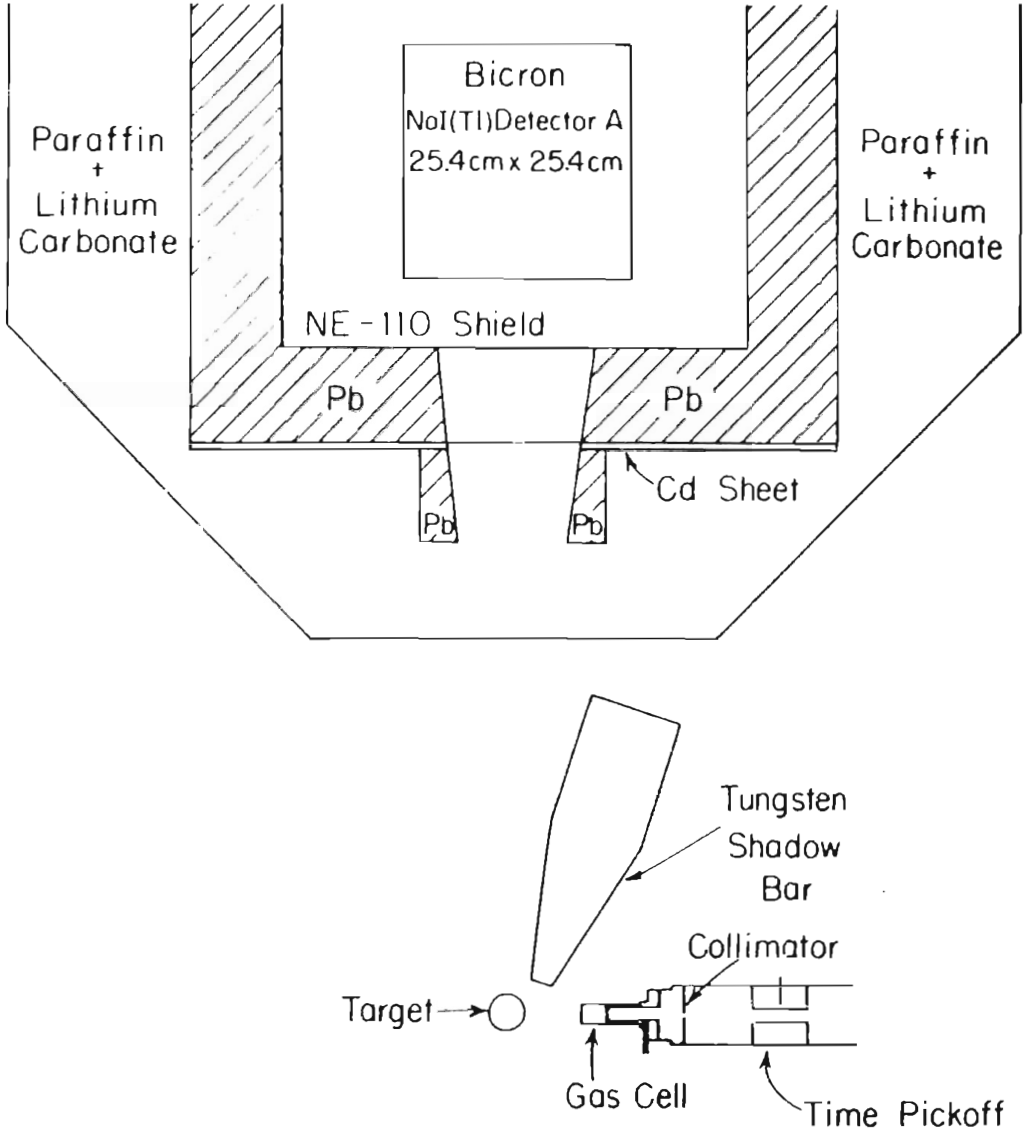
Bicron
NaI(Tl)Detector A
25.4cm x 25.4cm
Paraffin
+
Lithium
Carbonate
Paraffin
+
Lithium
Carbonate
NE-110 Shield
Pb
Pb
Pb
Pb
Cd Sheet
Tungsten
Shadow
Bar
Collimator
Target
Gas Cell
Time Pickoff

viewed by eight XP-1031 photomultiplier tubes, two in front, six in the rear. The crystal is viewed from the rear by six RCA 8575 photomultiplier tubes with transistorized bases which serve to stabilize the gain for moderately high counting rates (Turner, 1978).

Two NE-213 liquid scintillation detectors were used as monitors of the beam conditions. One, at 0^{o}, was used to monitor the neutron flux. The other at $\sim 90^{o}$ was used to optimize the timing in the pulsed beam experiments and to monitor the neutron polarization during the polarized beam experiments. These scintillators were viewed by RCA 8575 photomultiplier tubes with transistorized bases which provide a signal from the eighth dynode as well as from the anode. The bases were adjusted for the best neutron-γ pulse-shape discrimination. (see section 3.5).

3.5 Electronics

The main objective of the spectrometer electronics is to achieve good γ-ray energy resolution. A block diagram of these electronics is shown in figure 3-7. The bases of the six 8575's are gain matched for the highest resolution of the anode signals. After mixing, the signal is clipped to $\sim$ 350 nS with a partially open clipping line. In the Control Room, the signal is fanned out. One path is through a fast timing amplifier and a fast leading edge discriminator; a valid event generates a 400 nS gate and a routing pulse which enables the signal

Figure 3-7 Block diagram of spectrometer electronics.

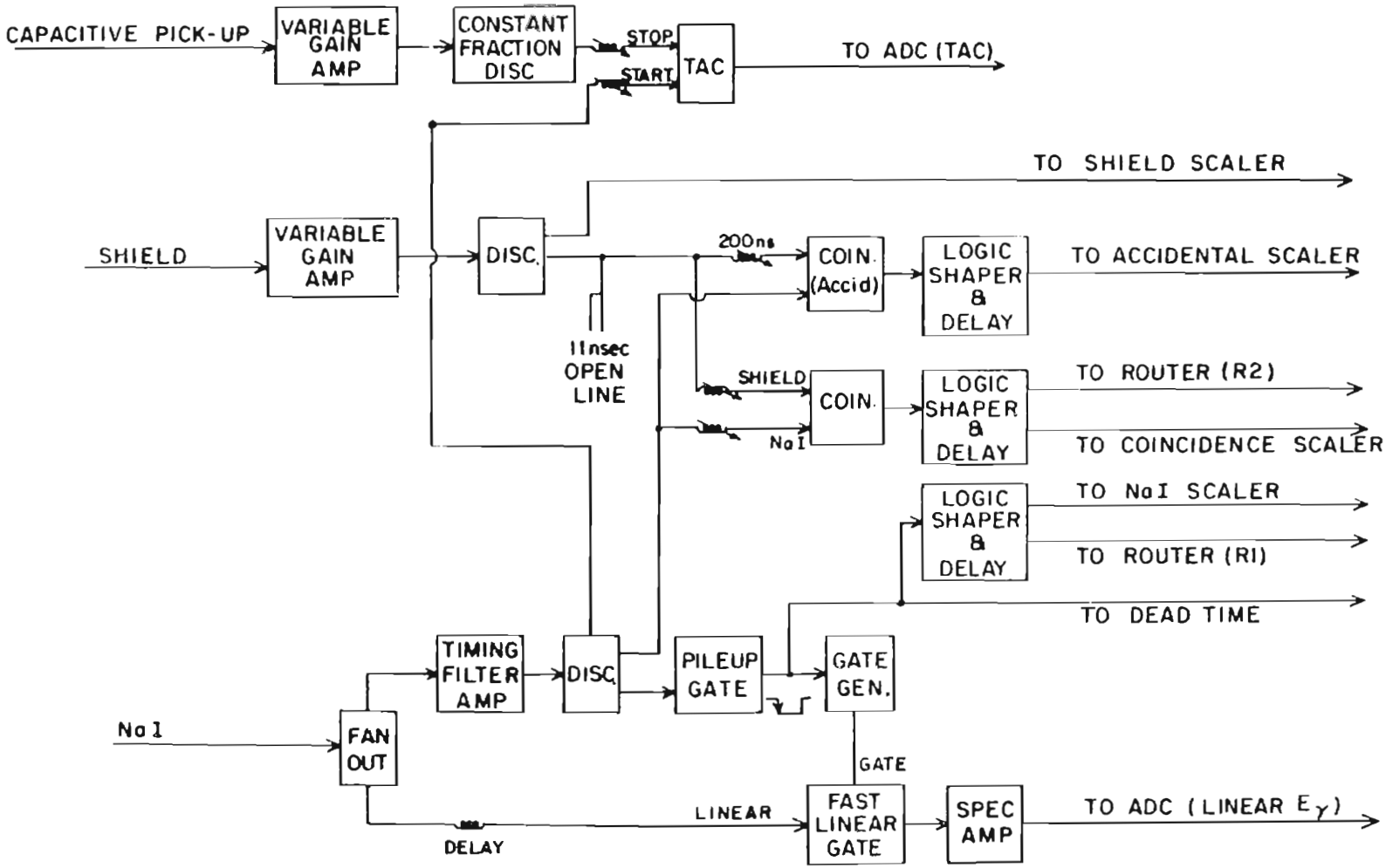
CAPACITIVE PICK-UP
VARIABLE GAIN AMP
CONSTANT FRACTION DISC
STOP
START
TAC
TO ADC (TAC)
TO SHIELD SCALER
SHIELD
VARIABLE GAIN AMP
DISC.
200ns
COIN. (Accid)
LOGIC SHAPER & DELAY
TO ACCIDENTAL SCALER
11nsec OPEN LINE
SHIELD
COIN.
NaI
LOGIC SHAPER & DELAY
TO ROUTER (R2)
TO COINCIDENCE SCALER
LOGIC SHAPER & DELAY
TO NaI SCALER
TO ROUTER (RI)
TO DEAD TIME
TIMING FILTER AMP
DISC.
PILEUP GATE
GATE GEN.
NaI
FAN OUT
GATE
LINEAR
FAST LINEAR GATE
SPEC AMP
TO ADC (LINEAR E_γ)
DELAY

from the other branch to pass to the linear amplifier and shaper. This fast discrimination serves to reduce pileup effects in that two small pulses which occur in a time greater than ~ 20 nS will not fire the discriminator. When a valid event is received, the gate is inhibited for the signal processing time (~ 10 μS). To achieve the anticoincidence rejection, the output of the fast discriminator is checked for overlap coincidence with the shield signal.

The eight XP-1031 anode signals are amplified by a gain of four, mixed, again amplified by a gain of four, limited, and clipped in the target area. In the Control Room the signal is presented to a fast amplifier with either a gain of one or five. The amplified signal is amplitude discriminated, again by a fast leading edge discriminator. This signal is checked for overlap coincidence with the NaI pulse as mentioned above; a valid coincidence generates a reject routing pulse for the computer. The resolving time of this coincidence is ~35 nS. The rejection efficiency (hence the resolution and efficiency of the spectrometer) is dependent upon the amplification in the shield line. This is discussed in section 4.5.

The pulsed beam (unpolarized) experiments allowed the gating of the NaI to eliminate or reduce the neutron-induced events which generally occur at a later time than the γ-ray events. To enable this gating, a time-to-amplitude converter was used. A start pulse was taken from the output of the fast discriminator in the NaI circuitry, and a stop pulse obtained from the time pickoff in the beam line (figure 3-4). Sorting was performed in the computer according to a selected time window.

The energy and time linear signals were presented to analog to digital converters and the data acquisition program read them in along with the routing pulses. Data sorting of the events was performed by the computer into valid and rejected spectra. Accidental coincidences between the shield and NaI were monitored by delaying a valid shield pulse so that only non-correlated coincidences were recorded. This accidentals rate was kept below seven percent of the true coincidence rate (see section 3.6). Detection count rates and dead times were also monitored.

The monitor electronics consisted of pulse-shape discrimination circuitry and time of flight circuitry. The low-energy bias was set half way up the Compton shoulder of ^{137}Cs. The detection efficiency is strongly dependent upon this setting as well as the geometrical alignment of the detector, so absolute normalization to these monitors was not possible; however, the relative yield at a given energy was useful for flux monitoring.

Neutron-γ-ray pulse shape discrimination is accomplished by using leading edge-to-crossover timing to measure the rise time of the pulses. Since neutrons deposit their energy in a manner which has a longer characteristic time for the light output than for γ-rays in NE-213, the output pulse rise time is longer for neutrons than gammas. To utilize this time difference, a time-to-amplitude converter is started by the crossover of the bipolar output of a delay line amplifier. The stop pulse is generated by sending the anode signal through a constant fraction discriminator. This output is insensitive to the rise time of the pulse. The resulting pulse-shape

discrimination was used to gate the time-of-flight signal which was presented to the computer. The stored data were dumped onto magnetic tape for later summing and analysis.

3.6 Summing Techniques

The relatively large Q-value of the $^{3}He(n,\gamma_0)^{4}He$ reaction makes the task of extracting sums comparatively straightforward; the background from neutron induced events is low and there are no low lying excited states in ^{4}He which would produce γ-rays in the region of interest. Figure 3-8 is a typical γ-ray energy spectrum; the contribution of (the intense) γ-rays from the radiative capture in the stainless steel target vessel appear as the dramatic rise in counts at the low energy end of the spectrum.

The sums were extracted using the program Roto4B for the low-rejection (Shield gain = 4) data and the program Rotofeed for the high-rejection (Shield gain = 80) data to the sum region. These programs are identical except for the line shape used in fitting the spectra. The line shapes are defined by the following function

$$F(x) = \begin{cases} \exp\left(\sum_{i=1}^{4} c_i x^{i-1}\right) & x < x_0 \\ \exp\left(\sum_{i=5}^{8} c_i x^{i-1}\right) & x \geq x_0 \end{cases}$$

Figure 3-8 Pulse-height spectrum for the $^{3}He(n,\gamma)^{4}He$ reaction. The rise at lower energies is from neutron radiative capture in the steel pressure vessel.

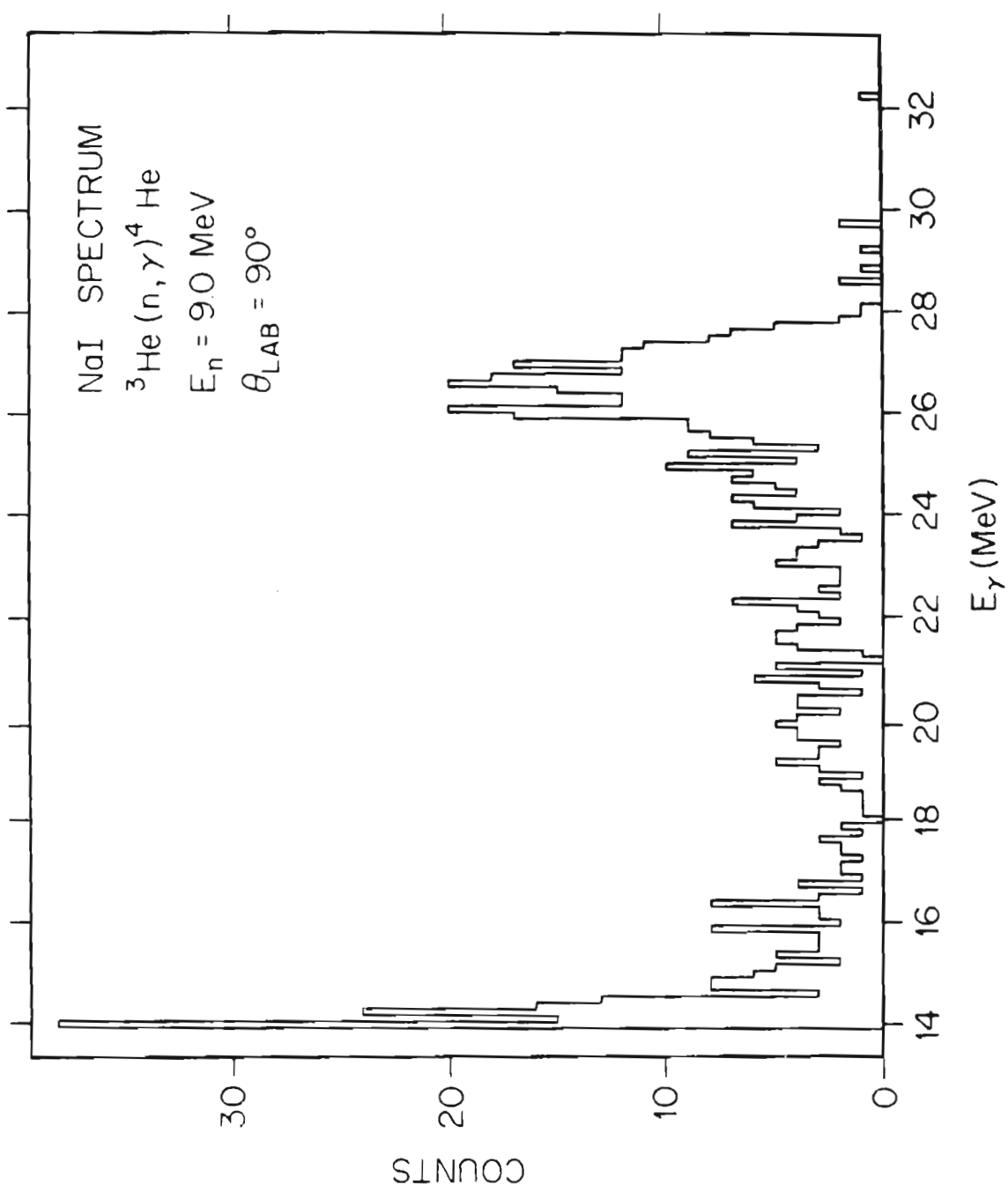
NaI SPECTRUM
$^3He(n,\gamma)^4He$
$E_n = 9.0$ MeV
$\theta_{LAB} = 90°$
COUNTS
0
10
20
30
14
16
18
20
22
24
26
28
30
32
E_γ (MeV)

The coefficients were determined (McBroom, Turner, 1978) by fits to a $^{3}H(p,\gamma)^{4}He$ γ-ray spectrum obtained at low bombarding energy. These coefficients are listed in table 3-1. The difference in the two line shapes arises from differences in rejecting the bremsstrahlung tail of the NaI response function. The high-rejection mode eliminates most of this tail from the spectrum, whereas the low-rejection mode does not.

Since the polarized data were taken with a DC beam, the cosmic-ray background was significant and had to be subtracted. This background is constant in energy in this region. Therefore these spectra were summed with a linear background fitted to the region immediately above the peak. The statistical error was simply determined as the square root of the sum in both cases. The γ-ray yields were corrected for the accidental rejection rate using the scaler sums which are described above in section 3.5.

Table 3-1 Coefficients of lineshape response function for NaI spectrometer.

Coefficient	Low-Rejection	High-Rejection
c_1	-3.6393	$-2.1858\ 10^{+1}$
c_2	$8.9809\ 10^{-2}$	$1.9262\ 10^{-1}$
c_3	$-4.8943\ 10^{-4}$	$-6.2133\ 10^{-4}$
c_4	$9.1427\ 10^{-7}$	$8.8137\ 10^{-7}$
c_5	$1.4269\ 10^{+3}$	$1.4269\ 10^{+3}$
c_6	$-1.4676\ 10^{+1}$	$-1.4675\ 10^{+1}$
c_7	$5.0242\ 10^{-2}$	$5.0238\ 10^{-2}$
c_8	$-5.7104\ 10^{-5}$	$-5.7108\ 10^{-5}$

4. ABSOLUTE CROSS SECTION

Because of its importance, the determination of the magnitude of the absolute cross section will be discussed in some depth. Factors included in this calculation account for the physical extent and characteristics of the experimental apparatus. The absolute intensity and spatial distribution of the neutron flux must be known. Interactions of the neutron and γ-ray flux with the steel pressure vessel must be evaluated. The target thickness is of course central to the calculation, and in this case presented some special problems since a gaseous sample was used. Finally, the detection efficiency affects the measurement directly. The expressions used in evaluating the cross section are outlined first.

4.1 Evaluation of Cross Section

It is useful to outline the procedure followed in determining a capture cross section, and to indicate the factors involved. If those neutrons which scatter and then interact in a $^3He(n,\gamma)^4He$ reaction are neglected, the γ-ray counting rate in the detector is given by

$$N_\gamma = \rho_T \rho_S \varphi_S \varepsilon_\gamma(E_\gamma) \int_{V_S} \int_{V_T} \int_{A_D} \sigma_{n,\gamma}(\theta,E_n)\ \sigma_{d,n}(\theta',E_d')\ T_\gamma\ T_n \times r_{ST}^{-2}\ r_{SD}^{-2}\ dV_S\ dV_T\ dA_D \qquad (4.1)$$

where

N_γ = number of γ ray events observed in detector s^{-1}

ρ_T = nuclear density of target cm^{-3}

ρ_S = nuclear density of source cm^{-3}

φ_S = flux of deuterons $s^{-1}\ cm^{-2}$

ε_γ = detection efficiency of Spectrometer

$\sigma_{n,\gamma}$ = capture cross section

$\sigma_{d,n}$ = lab cross section of source reaction

T = transmission function $e^{-\Sigma x}$

where x is the path length thru the absorber

r_{ST} = distance from source site to target site

r_{SD} = distance from target site to detector site

Integrals over the source, target and detector account for their finite size. The areal integral over the detector is indicative of the fact that any γ-ray scattered into the solid angle of the detector

will be recorded with efficiency $\varepsilon_\gamma(E_\gamma)$. In reality, a fourth integral over the neutron energies must be included, but has been omitted for clarity.

Neutrons that scatter in the target or pressure vessel will contribute an additional counting rate to the detector. For most capture experiments, the absorption of the neutron and γ-ray flux by the target material is significant and must be evaluated. For the gaseous ^{3}He target the attenuation and multiple scattering effects are small. The steel shell however must be taken into account. The flux of neutrons into the target volume originating from scattering off the lower flange and walls of the cell is evaluated in section 4.3.

Following the development of Kinney (1970), the expression for the counting rate may be written as

$$N_\gamma = \rho_T \rho_S \varphi_S \varepsilon_\gamma(E_\gamma) \frac{1}{R_{TD}^2} \frac{1}{R_{ST}^2} e^{-\Sigma_\gamma \ell_\gamma} e^{-\Sigma_n \ell_n} \times \sigma_{n,\gamma}(\theta,\overline{E_n}) \sigma_d(0^\circ,\overline{E_d'}) V_S V_T A_D C(\theta,E) \qquad (4.2)$$

$$C(\theta,E) = \frac{\int_{V_S}\int_{V_T}\int_{A_D} \sigma_{n,\gamma}(\theta,E_n) \sigma_{d,n}(\theta',E_d') T_\gamma T_n r_{ST}^{-2} r_{SD}^{-2} dV_S dV_T dA_D}{[A_D R_{TD}^{-2} R_{ST}^{-2} e^{-\Sigma_\gamma \ell_\gamma} e^{-\Sigma_n \ell_n}] \sigma_{n,\gamma}(\theta,\overline{E_n}) \sigma_d(0^\circ,\overline{E_d'}) V_S V_T} \qquad (4.3)$$

$C(\theta,E)$ is discussed in section 4.3. The mean path length through the absorber ℓ_γ and ℓ_n for γ-rays and neutrons respectively is evaluated in section 4.4. The expression for the γ-ray counting rate may be

written in the more convenient form

$$N_\gamma = N_T\, n_S\, S_S\, \varepsilon_\gamma(E_\gamma)\, \Omega_\gamma\, T_\gamma\, T_n\, \sigma_{n,\gamma}(\theta,E_n)\, C(\theta,E) \qquad (4.4)$$

N_T = number of target nuclei

n_S = number of deuterium nuclei per area

S_S = deuteron current s^{-1}

$\Omega_\gamma = \frac{A_D}{R_{TD}^2}$ solid angle subtended by detector

The following sections contain discussions of these factors; the determination of the 0° neutron flux is discussed first.

4.2 Neutron Flux

Without a convenient way to monitor the flux of neutrons at the target, it is desirable to calculate the flux from the deuteron beam current and the deuterium target thickness. The $^2H(d,n)^3He$ cross section evaluated by Drosg (1978) provides a starting point for such a calculation. Experimental uncertainties, however make it desirable to measure the zero-degree flux to compare to this calculation. The details of this measurement have been presented (King et al., 1980). By using a polyethylene foil of known thickness, the recoil proton flux from the neutron beam was measured with a silicon surface barrier detector at $E_n(0^\circ)$ = 9, 12 MeV. Since the n-p differential cross section is known, the neutron flux can be determined. The flux was found to vary linearly with the gas cell pressure and deuteron beam

current. This indicates that there is no reduction of neutron flux from beam heating effects in this range of current, ($\leq$ 500 nA). The 0^{o} flux was then calculated from the expression

$$F_n = \sigma_{d,n}(0^{o},E_d) \frac{N_A}{v} L \frac{J}{e} \qquad (4.5)$$

where

F_n = flux of neutrons $sr^{-1} \cdot s^{-1}$

N_A = Avogadro's number

$\frac{1}{v}$ = molar density cm^{-3}

L = nominal gas cell length cm

J = deuteron current $Coul \cdot s^{-1}$

e = electronic charge Coul

Agreement between the measurement and calculation was found to within the statistical error of 5p in the recoil measurement. The scale error quoted by Drosg is $\pm$ 1% and the relative error in the angular distribution is $\pm$ 1%. The deuterium target pressure is known to better than $\pm$ 1%, but the target length is uncertain due to the stretching of the Havar entrance window. Beam integration is better than $\pm$ 3%.

4.3 Finite Geometry Corrections

A computer code, Fixer has been developed (Jensen, 1980) to calculate the effect of 1)finite geometry, 2)neutron attenuation and multiple scattering, 3)γ-ray attenuation. The program utilizes a

Monte-Carlo numerical integration technique to calculate averaged or "observed" cross sections from microscopic or "true" cross sections. The ratio of these cross sections as a function of angle is used to correct the experimental data, and corresponds to the $C(\theta,E)$ as defined in equation (4.3). A trial cross section is obtained by assuming that 1)the source is a point source 2)the target is small enough that the neutron flux is uniform over the target, and 3) the detector is far away from the target. The program then calculates an observed cross section from this guess. Thus, the ratio, $C(\theta,E) = \sigma_T(\theta,E)/\sigma_0(\theta,E)$ can be obtained at each detector position. This ratio depends upon the true cross section and its rate of change with respect to angle, but convergence is found with one pass since our (n,γ) angular distributions typically do not exhibit dramatic fluctuations. The mean neutron flux at the target is less than the flux at zero degrees as is demonstrated in figure 3-2. Hence the correction ratio is generally greater than one as this is the largest factor involved in the calculation.

Attenuation of the neutron and γ-ray flux as well as multiple scattering in the target are functions of target density. These corrections were not included in the Fixer calculation since the target density was low. The target density was 17.1 mg/cm^3. The neutron macroscopic total cross section was 0.010 cm^{-1} (ENDF/b-IV), and the gamma macroscopic cross section was $1.4X10^{-4}$ cm^{-1} at E_γ = 30. MeV (Storm and Israel, 1970). The program Fixer was modified to accept the domed shape of the ^3He target. Figure 4-1 shows the energy dependence of $C(90^o,E)$. Its increase with energy reflects the

Figure 4-1 Finite-geometry correction factor.

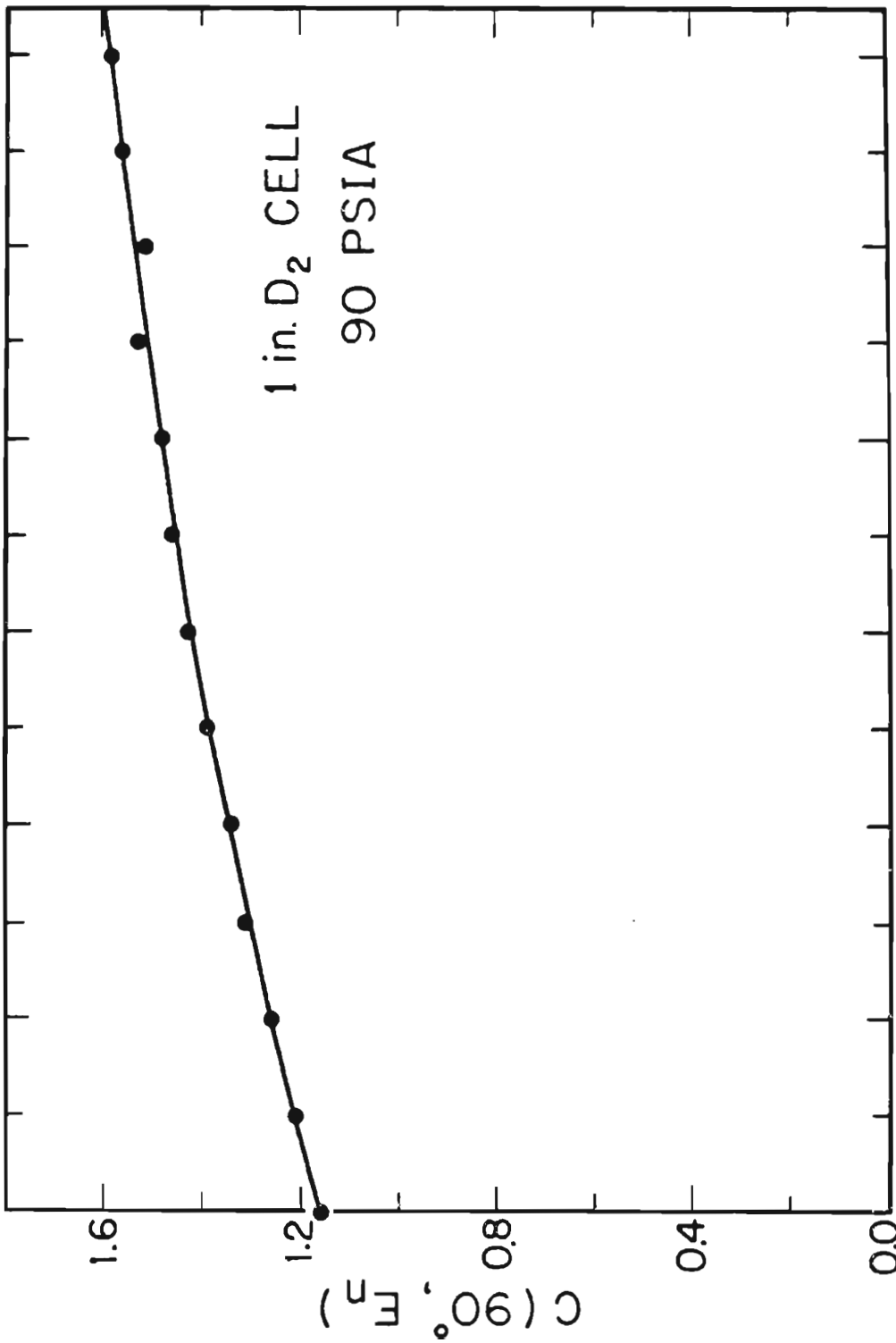
1 in. D_2 CELL
90 PSIA
C (90°, E_n)
E_n (MeV)
0.0
0.4
0.8
1.2
1.6
6
8
10
12
14
16
18

increase in kinematic forward peaking of the $^{2}H(d,n)^{3}He$ reaction in the laboratory frame. A sufficient number of histories was run in order to obtain statistical scatter of less than 1%.

4.4 Effects of Steel

The effects considered in this calculation are: 1)the attenuation of the neutron flux by the vessel wall, 2)the scattering into the target volume of neutrons by the wall and bottom flange and 3)the attenuation of the gamma-ray flux by the wall. An analytic approximation made to estimate these is based on the disc approximation of Kinney et al. (1970). in which the target is assumed to be disc-shaped, and the neutron flux is assumed to be uniform. To obtain the transmission factors, the mean chord length corresponding to a neutron or γ-ray path length thru the steel shell was computed using the relation

$$\bar{\ell} = \frac{\int \ell \, \ell' \, dy}{\int \ell' \, dy} \tag{4.6}$$

The relationship of the path length to the sample volume is shown in figure 4-2(b). For the neutron flux, this is a path length weighted by the target element that path would intercept. If the γ-rays are assumed to be uniformly generated in the target disc then the same argument applies. This calculation was performed for the two regions as indicated in figure 4-2(a). The steel shoulder of region II

Figure 4-2 Geometry for correction for effects of steel.

a)

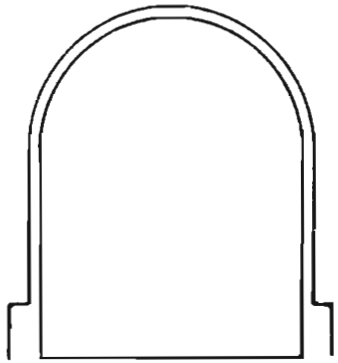

REGION I

REGION II

b)

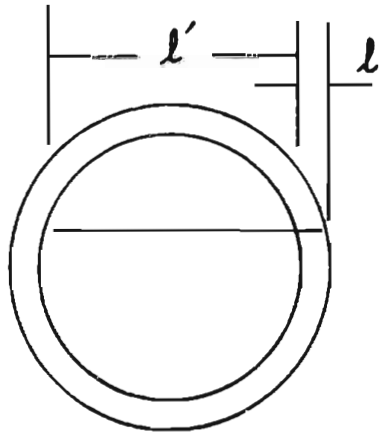

attenuates the flux significantly more than the shell of region I. The flux of neutrons scattered off of the steel into the target volume was estimated by using the elastic cross section averaged over $\cos\theta = +0.6$ to -0.6. The mass was assumed to be at the center of the flange and to scatter neutrons into 2π steradians. On the basis of this approximation, the secondary flux is less than 0.1 % of the average primary flux thru the target volume.

4.5 Target Thickness

Of central importance to the absolute cross section measurement is the determination of the ^{3}He target density. Pressure gauges used in this determination had only a nominal precision of 5% of full scale (3000 psi) which is 7% in the region that was used. Therefore an alternate method of determining the target thickness was necessary in order to check the gauge. A Metler E200 balance was used to weigh the cell, first evacuated, then pressurized with ^{3}He. This balance has the capacity to measure the mass of the steel pressure vessel yet also the precision to accurately determine the mass of ^{3}He. Since the cell was fabricated to precise dimensions the interior volume was known rather well (40.0 ± 0.1 cm^3) and a gas law could be used to compare to the measured pressure. The law employed takes the compressibility of the gas into account: $PV/nRT = z$ where z is the compressibility of the gas. This is an empirical equation and the value of the compressibility for Helium is $z = 1.068$ at 70 degrees Fahrenheit and

2000 psia (Braker and Mossman, 1971). By using this formula, a pressure of 2125 PSI is equivalent to 0.230 moles of ^{3}He in the cell (including 1 cm^3 in the fill tube). The amount of ^{3}He from weighing the cell is 0.225 moles.

4.6 Spectrometer Efficiency

A knowledge of the behavior of the detection efficiency as a function of energy is essential to a determination of an absolute cross section. In order to evaluate the detection efficiency $\varepsilon \cdot \Omega$ of the spectrometer system, the solid angle Ω is assumed to be fixed by the Pb collimator which is chosen so that a point source would exactly illuminate the rear face of the 24.5cm X 24.5cm NaI crystal. The spectral response of the system to a monoenergetic γ-ray is characterized by a function which is fitted to a spectrum from the $^3H(p,\gamma_0)^4He$ reaction. This line shape then serves to define the portion of the peak to be summed in measuring ε. The procedure for its determination has been outlined elsewhere (Weller and Roberson 1980); however, its central importance to the present work dictates that the pertinent features be outlined here. There are few calibration sources for γ-rays of these energies (E_γ = 24 to 34 MeV); however, the yield of γ-rays per proton for the $^{12}C(p,\gamma_0)^{13}N$ at 15.1 MeV proton bombarding energy has been measured (Marrs et al., 1975), and can be used as a calibration. To obtain the efficiency at other γ-ray energies several effects must be taken into account, namely the

γ-ray absorption of the Li_6CO_3, paraffin, and plastic shield as well as the rejection efficiency. Figure 4-3 shows the energy dependence of the detection efficiency as extrapolated, the shaded area reflects the error in the measurement at 15.1 MeV. The rejection efficiency of the system is dependent upon the gain in the shield anode signal which is presented to the fast discriminator. In order to obtain a lower rejection efficiency and therefore higher detection efficiency the gain was lowered to X4. This mode of operation however makes the efficiency more sensitive to shifts in the gain (or discriminator threshold). This sensitivity can be seen in figure 4-4, the rate of change of the efficiency is large for the gain shown. Consequently the discriminator threshold was checked regularly in the setup procedure to insure that the discriminator had not drifted. Additionally, the yield from $^{40}Ca(n,\gamma)$ was measured at set up to be sure that no gross shift in efficiency was observed.

4.7 Yield Curve and Error Discussion

Absolute cross section measurements were made in two independent runs. Other differential cross section measurements were made and normalized to them. Table 4-1 gives a summary of the data, and factors which were used to obtain absolute cross sections from the yields. Figure 4-5 shows the $^3He(n,\gamma)^4He$ ninety degree cross section which was obtained in the present experiment. The error bars shown are statistical only and do not reflect any error in normalization.

Figure 4-3 Detection efficiency as a function of energy. The shaded region reflects the error in the measurement at E_γ = 15.1 MeV.

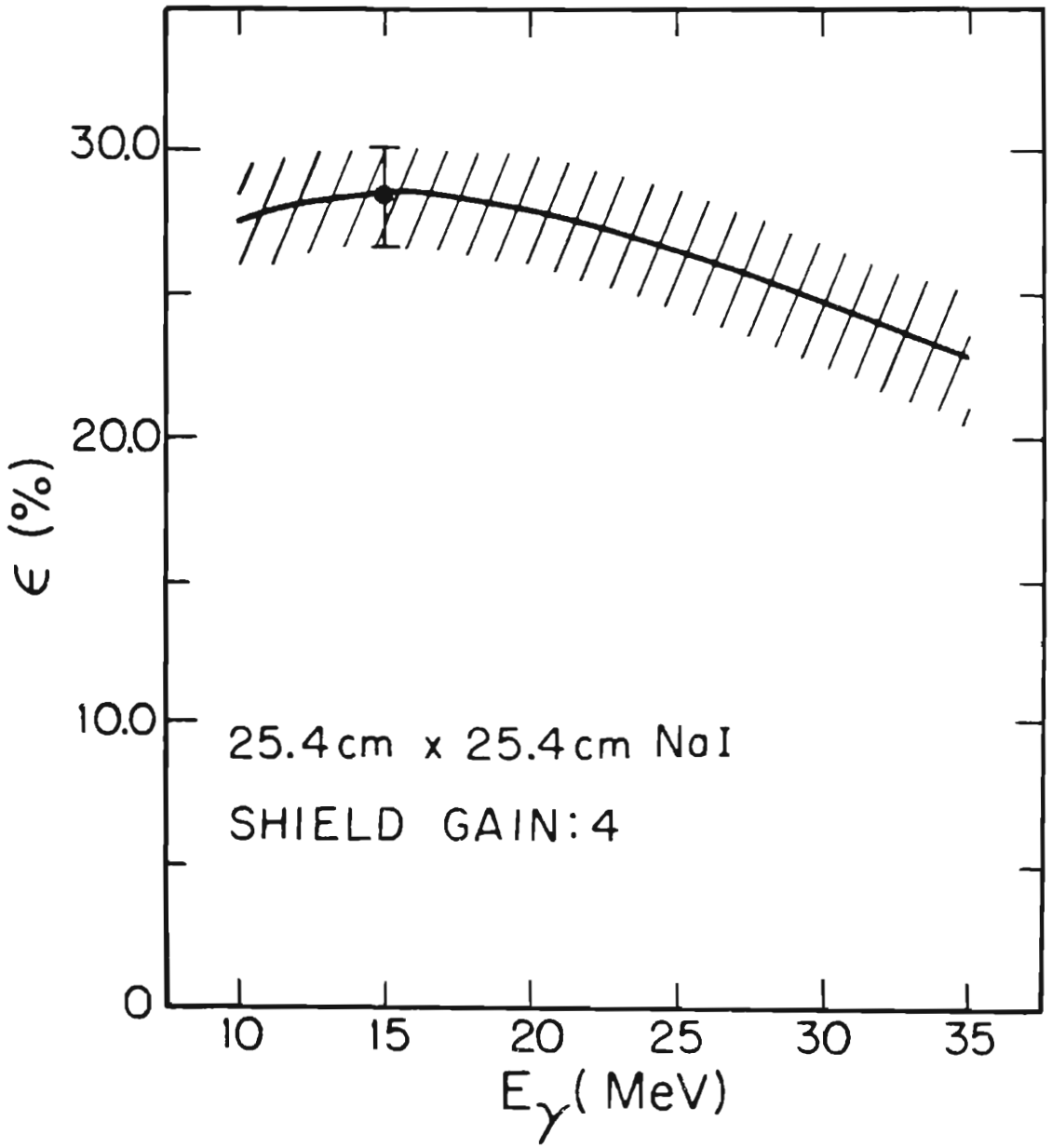
30.0
20.0
10.0
0
ε (%)
25.4cm x 25.4cm NaI
SHIELD GAIN: 4
10
15
20
25
30
35
E_γ (MeV)

Figure 4-4 Detection efficiency as a function of shield gain at E_γ = 15.1 MeV.

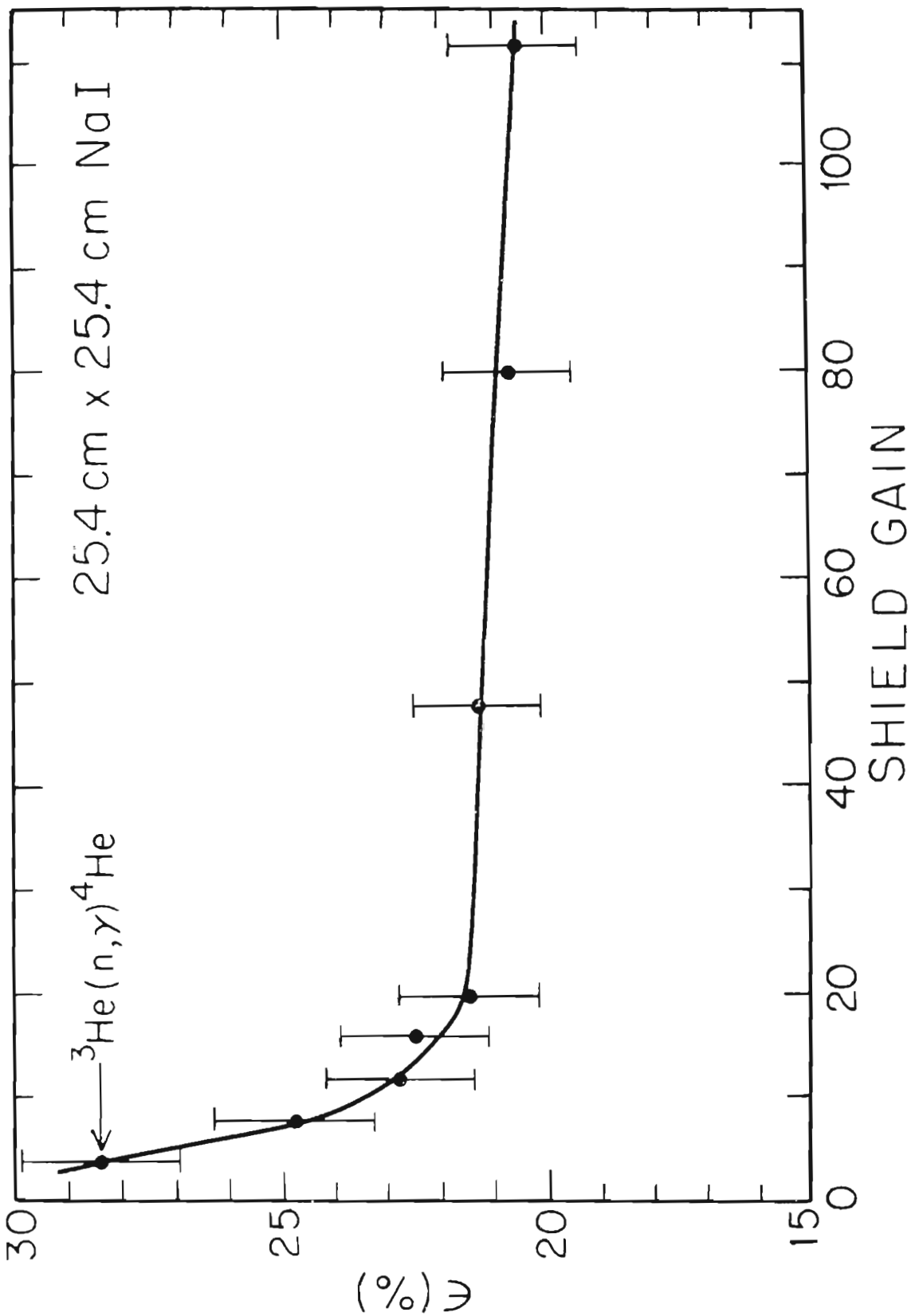
25.4 cm x 25.4 cm NaI
$^3He(n,\gamma)^4He$
ε (%)
SHIELD GAIN
30
25
20
15
0
20
40
60
80
100

Table 4-1 Summary of experimental ninety-degree cross section data. The inferred total photodisintegration cross section is given.

E_n (MeV)	$\frac{d\sigma}{d\Omega}\|_{CM}(90^\circ_{Lab})$ $(\frac{\mu b}{sr})$	Error	E_x (MeV)	σ_T (mb)	Error
6.0	5.9	0.3	25.1	0.99	0.05
6.5	5.4	0.3	25.5	0.96	0.05
7.0	5.2	0.3	25.8	0.97	0.05
7.5	6.0	0.4	26.2	1.15	0.08
8.0	5.0	0.3	26.6	1.01	0.06
8.5	5.3	0.3	27.0	1.09	0.06
9.0	5.0	0.3	27.3	1.06	0.06
9.5	4.6	0.1	27.7	1.00	0.03
10.0	4.9	0.1	28.1	1.09	0.03
10.5	4.8	0.3	28.5	1.10	0.06
11.0	4.5	0.3	28.8	1.05	0.06
11.5	3.6	0.2	29.2	0.85	0.04
12.0	3.6	0.2	29.6	0.87	0.05
12.5	3.8	0.1	30.0	0.93	0.03
13.0	3.9	0.1	30.3	0.98	0.03
13.5	4.2	0.2	30.7	1.05	0.04
14.0	4.1	0.2	31.1	1.06	0.05
14.5	3.9	0.2	31.5	1.01	0.05
17.0	3.7	0.4	33.3	1.0	0.1
18.0	3.1	0.4	34.1	0.85	0.1

Figure 4-5 Ninety degree cross section for $^{3}He(n,\gamma)^{4}He$ and $^{3}H(p,\gamma)^{4}He$ reactions. Proton capture data is from Meyerhof (1970).

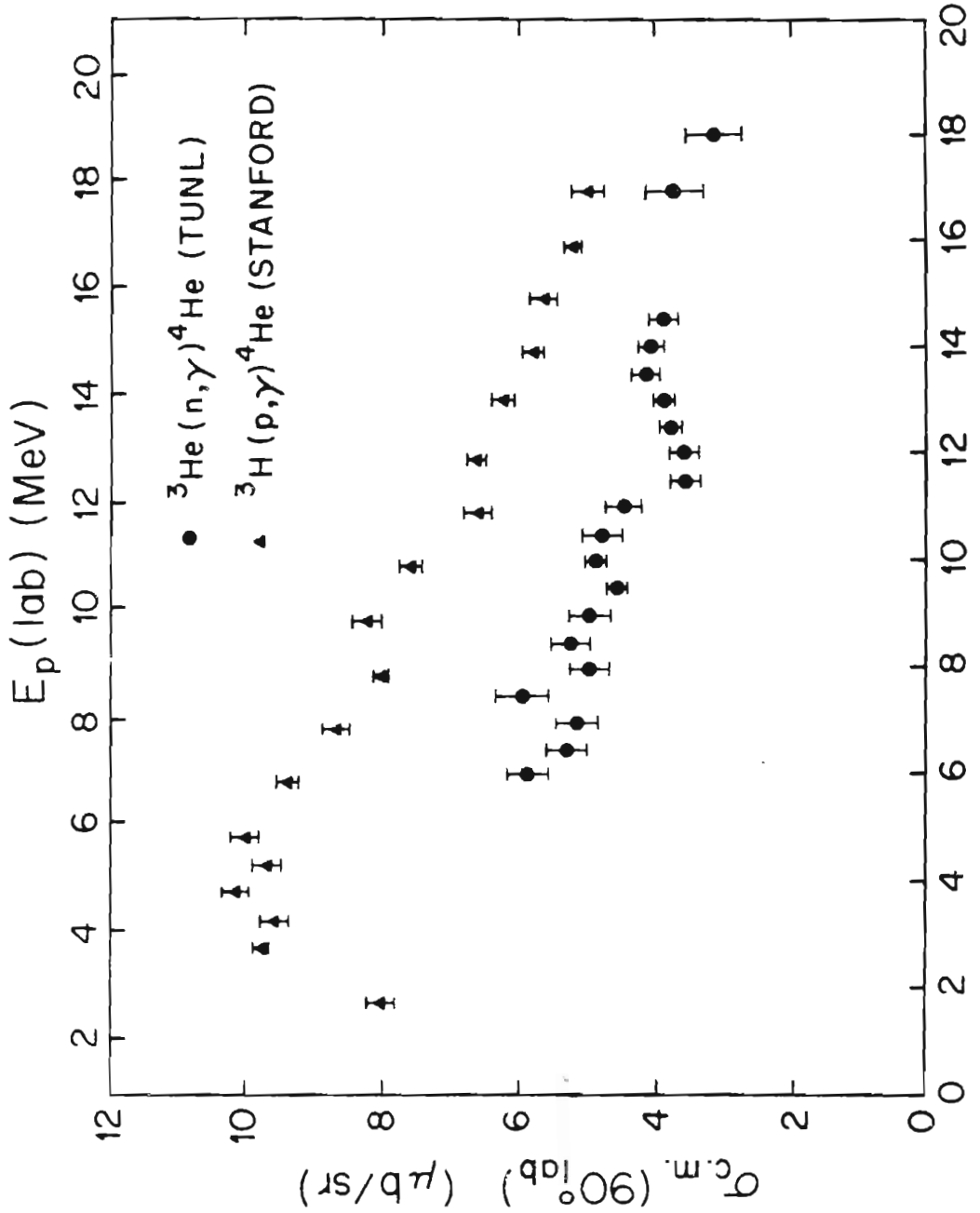
E_p (lab) (MeV)
E_n (lab) (MeV)
$\sigma_{c.m.}(90°_{lab})$ (μb/sr)
^{3}He(n,γ)^{4}He (TUNL)
^{3}H(p,γ)^{4}He (STANFORD)

The $^{3}H(p,\gamma)^{4}He$ ninety degree cross section obtained by Meyerhof *et al.* (1970), which was normalized to the data of Perry and Bame (1955) is also shown.

4.8 $^{3}H(p,\gamma)^{4}He$ Measurement

Since it is the ratio, R, of the $^{4}He(\gamma,p_0)^{3}H$ cross section to the $^{4}He(\gamma,n_0)^{3}He$ cross section that is of interest, a remeasurement of the $^{3}H(p,\gamma)^{4}He$ differential cross section is of value, even though previous measurements of this cross section have been in agreement. By measuring both of these cross sections with the same instrument, the systematic scale errors which would arise from the detection efficiency are eliminated in the ratio. Of course, this measurement does not eliminate errors which would arise from uncertainties in target densities or incident flux. A previous measurement of the 90^{o} differential cross section at this lab (McBroom, 1977) was in good agreement (to within statistical error) with the measurement of Meyerhof *et al.* (1970).

Measurement of the 90^{o} differential cross section was made at an energy of E_p= 9 MeV. The (p,γ) cross section was normalized to the yield of elastically scattered protons monitored with a pair of silicon surface barrier detectors at $\theta_{LAB}= \pm 160^{o}$ with respect to the beam. The resulting cross section is $\sigma(90) = 8.4 \pm 0.2\mu b/sr$. The elastic scattering cross section changes rapidly with angle and rather small collimators were used so that the uncertainty in this

measurement is ~ 20% but it gives a clear indication of the value of the ratio. The elastic scattering cross section deduced from the phase shifts of Kankowski (1972) were used for the normalization ($\sigma_{LAB}(160_{LAB})$ = 53.4 mb/sr). As a check of the detection efficiency, it was calculated from the rejection efficiency and the absorption coefficient of the material in front of the detector. Figure 4-6 shows the pulse height spectrum obtained from the $^{3}H(p,\gamma)^{4}He$ reaction. The rejected spectrum is obtained from those events which are in coincidence with an event in the shield. The sum of these spectra represents the response of NaI to the monoenergetic 26.6 MeV γ-rays. If this response were known over the entire energy range (0 to 27 MeV) the efficiency could be calculated from the absorption of the shielding material and the solid angle angle subtended by the detector. This response to a monoenergetic γ-ray is of course obscured by events produced by other sources. In practice, a fixed region is summed in the accepted spectrum, the efficiency then involves the ratio of this sum to the sum of the total response function. To estimate this ratio, the response was assumed to have a linear shape below the observed region which intercepts zero counts at at $E_{\gamma} = 0$. Based on this extrapolation, the estimated efficiency $\varepsilon_{\gamma}(26.6) = 0.245$. The efficiency extrapolated from 15.1 MeV is $\varepsilon_{\gamma}(26.6) = 0.256$. This agreement is well within the errors associated with the estimation of the bremsstrahlung tail. The expression used for the evaluation of the $\sigma_{cm}(90^{o})$ is

$$N_{\gamma} = \sigma_{p,\gamma}(\theta_{\gamma},E_{p})\ \Omega_{\gamma}\ \varepsilon_{\gamma}(E_{\gamma})\ n_{t}\ S_{p} \qquad (4.7)$$

Figure 4-6 Pulse height spectrum from $^{3}H(p,\gamma)^{4}He$ reaction.

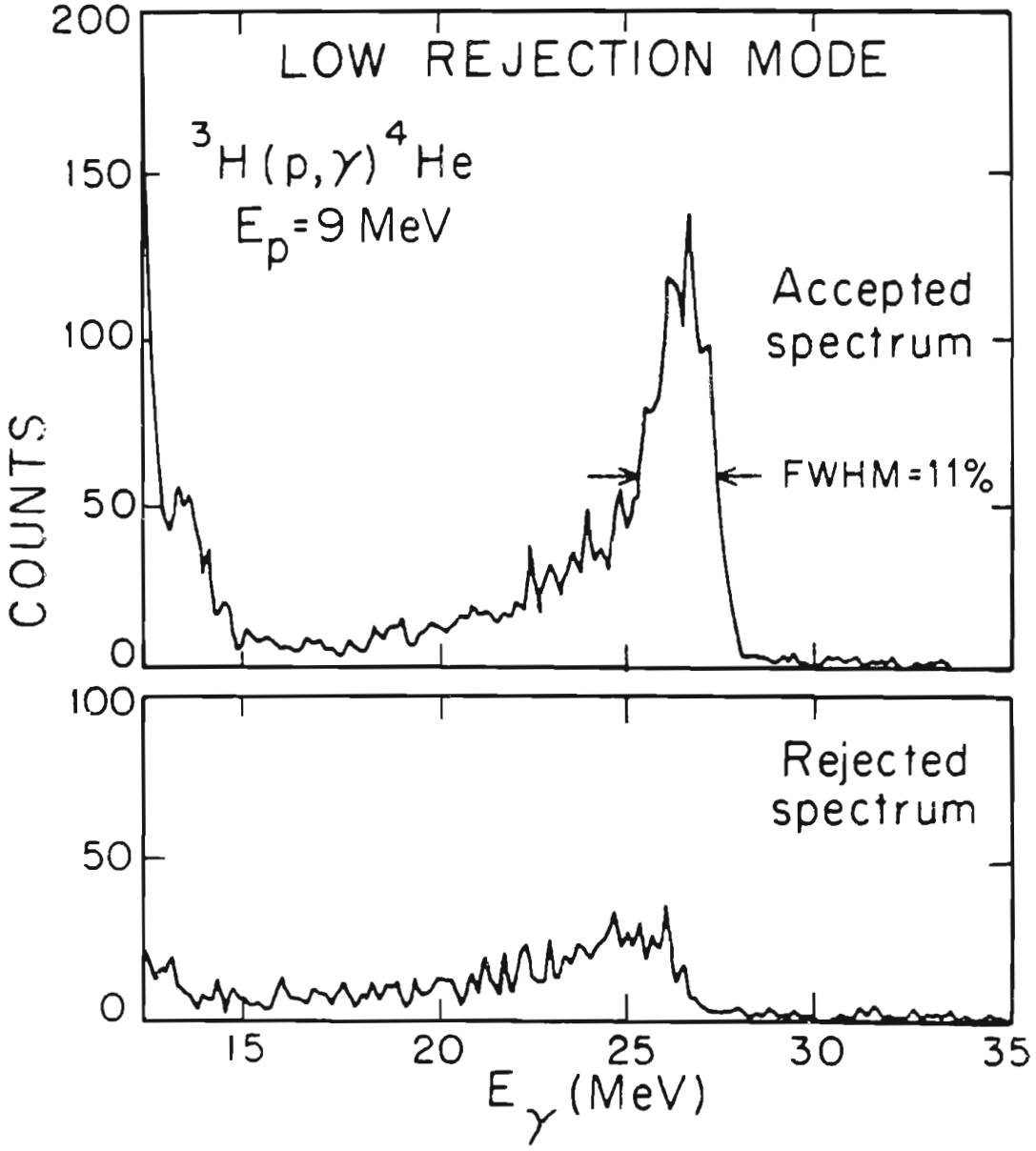
LOW REJECTION MODE
$^3H(p,\gamma)^4He$
E_p=9 MeV
Accepted spectrum
FWHM=11%
Rejected spectrum
COUNTS
200
150
100
50
0
100
50
0
15
20
25
30
35
E_γ (MeV)

where

$\sigma_{p,\gamma}$ = capture cross section

n_t = number of target nuclei per area

S_p = number of protons in beam per time

The target areal density was determined from

$$\tau = \frac{n_t A_t}{\cos\theta_t N_A}$$

$$= \frac{N_p}{\sigma_p(\theta_p, E_p)\ \Omega_p\ S_p\ \cos\theta_t} \frac{A_t}{N_A} \qquad (4.8)$$

where

A_t = nuclear mass of target

θ_t = angle between beam and normal to target

Ω_p = solid angle subtended by monitor

So that the (p,γ) cross section may be expressed in terms of the (p,p) yield.

5. ANGULAR DISTRIBUTION MEASUREMENT

Measurement of the observables $\sigma(\theta)$ and $A(\theta)$ yield information about the interaction which couples the incident particle channel with the γ-ray exit channel. In the case of a spin $\frac{1}{2}$ particle on a spin $\frac{1}{2}$ target, the interaction may be interpreted very simply in terms of four partial waves if only E1 and E2 radiation is included. The appeal of this situation is that if the cross section and analyzing power are known, well-determined information about the transition matrix elements may be extracted. In this study, the channel-spin coupling scheme is used and two of these matrix elements correspond to spin-flip for E1 and E2 transitions. Measurement of these terms allows evaluation of the spin dependent part of the interaction. This chapter contains discussions of the formalism as well as the data and fits. Interpretation of the results is made in chapter 6.

5.1 Angular Distribution Formalism

The measurement of cross section and analyzing power times cross section allows one to extract information about the partial cross sections and allow a more complete understanding of the reaction involved.

In order to effectively discuss the measurements, the notation and coupling scheme is defined. The expression for the differential cross section for polarized incident beam is given by

$$\sigma(\theta,\phi) = \sigma_u(\theta) \; [\; 1 + \vec{p}\cdot\vec{A}(\theta) \;],$$

in which σ_u is the unpolarized cross section, $\vec{p}$ is the beam polarization vector, and $\vec{A}$ is the analyzing power vector. A coordinate system is chosen so that y is along the direction $\vec{k}_{in} \times \vec{k}_{out}$ and z along $\vec{k}_{in}$. The beam polarization is parallel or antiparallel to the y axis, and the analyzing power

$$A_y = \frac{1}{p_y} \frac{N_+ - N_-}{N_+ + N_-}$$

can be measured. To extract the information on the partial reaction cross sections, the channel spin angular momentum coupling scheme was adopted. The angular momenta are given by : $a = \frac{1}{2}$ = spin of target, $x = \frac{1}{2}$ = spin of projectile which carries orbital angular momentum ℓ, b is the spin of the γ-emitting state, L is the multipolarity of the γ-ray with mode p (1 electric, 0 magnetic), and c is the spin of the

residual state. They are coupled in the following order

$$\vec{x} + \vec{a} = \vec{s} \qquad s = \text{channel spin}$$

$$\vec{\ell} + \vec{s} = \vec{b} \qquad b = \text{total angular momentum}$$

$$\vec{L} + \vec{c} = \vec{b},$$

and in the case of capture of spin one half on spin one half leading to a spin zero residual nucleus, the incident channel spin can be $s = 0$ or 1. Electromagnetic transitions of mode and multipolarity E1, E2 can occur only if the intermediate state has spin and parity 1^-, 2^+ respectively. The reduced transition matrix elements are denoted as

$$^{s}T_{\ell b} = \langle pL(c)b\pi' || R || \ell(xa)sa\pi \rangle$$

and

$$^{s}T'_{\ell b} = \langle p'L'(c)b'\pi' || R || \ell'(xa)s'b'\pi \rangle.$$

The complex radial matrix elements can be written as a real amplitude and a phase, and for capture to ^{4}He followed by γ-ray decay to the ground state the matrix elements may be denoted by

$$^{0}T_{11} = {}^{1}P_1 \exp(i\phi_{1P}) = \langle 11(0)- || R || 1(\tfrac{11}{22})01- \rangle$$

$$^{1}T_{11} = {}^{3}P_1 \exp(i\phi_{3P}) = \langle 11(0)- || R || 1(\tfrac{11}{22})11- \rangle$$

$$^{0}T_{22} = {}^{1}D_2 \exp(i\phi_{1D}) = \langle 12(0)- || R || 2(\tfrac{11}{22})02+ \rangle$$

$$^{1}T_{22} = {}^{3}D_2 \exp(i\phi_{1D}) = \langle 12(0)- || R || 2(\tfrac{11}{22})12+ \rangle$$

Here, the channel spin labeling by the incident partial wave completely determines the reaction matrix element, because of conservation of angular momenta and parity. The notation followed in labeling the amplitudes is $^{2s+1}\ell_{\ell+s}$. The expressions for cross

section and cross section times analyzing power may be expanded in terms of Legendre polynomials and associated Legendre polynomials.

$$\sigma_u(\theta) = (\lambda\!\!\!^{-}/2)^2 \tilde{x}^{-2} \tilde{a}^{-2} \left[1 + \sum_k a_k P_k \right]$$

and

$$\frac{\sigma(\theta)\cdot A(\theta)}{A_0} = \sum_{k=1}^{n} b_k P_k^1(\cos\theta).$$

The symbol $\tilde{y}$ denotes $\tilde{y} = \sqrt{2y+1}$.

The a_k and b_k coefficients of the Legendre expansions can be written in terms of the reduced transition matrix elements:

$$A_0 = (\lambda\!\!\!^{-}/2)^2 \tilde{x}^{-2} \tilde{a}^{-2} \sum_t b^2 |T|^2$$

$$a_k = \frac{(\lambda\!\!\!^{-}/2)^2 \tilde{x}^{-2} \tilde{a}^{-2}}{A_0} \left[\sum_{tt'} (-)^{s-c+1} [] \tilde{J}\tilde{J}' \tilde{L}\tilde{L}' \tilde{b}^2 \tilde{b}' \, ^2 (J0, J'0|k0) \right.$$

$$\times W(Jb J'b'; sk)(L1, L'-1|k0)$$

$$\left. \times W(LbL'b'; ck) \mathrm{Re}(TT'^{*}) \right]$$

and

$$b_k = \frac{(\lambda\!\!\!^{-}/2)^2 \tilde{x}^{-2} \tilde{a}^{-2}}{A_0}$$

$$\times \left[\frac{3\sqrt{x}\ \tilde{x}\tilde{k}}{[(x+1)k(k+1)]^{1/2}} \sum_{tt'} [] \tilde{s}\tilde{s}' \tilde{J}\tilde{J}' \tilde{L}\tilde{L}' \tilde{b}^2 \tilde{b}' \, ^2 \right.$$

$$\times (-1)^{a-x+c-b-s+1}(\ell 0,\ell' 0|k0)$$

$$\times W(xsxs';a_1)(L1,L'-1|k0)W(LbL'b';ck)$$

$$\times X(1sb;1's'b';k1k)\mathrm{Re}(iTT''^{*}) \Big] .$$

The indices t and t' are used for sums over pp'LL'bb'$\ell\ell$'s and s'. The empty bracket denotes the parity term

$$[] = \frac{1}{2}[1+(-)^{L+p+L'+p'+k}].$$

The evaluated expressions for the a_k and b_k coefficients for this case are

$$1 = 0.750(^1P_1{}^2 + {}^3P_1{}^2) + 1.250(^1D_2{}^2 + {}^3D_2{}^2) \quad \text{normalization}$$

$$a_1 = 2.598\,{}^1P_1\,{}^1D_2\cos(\phi_{1D}-\phi_{1P}) + 2.250\,{}^3P_1\,{}^3D_2\cos(\phi_{3D}-\phi_{3P})$$

$$a_2 = -0.750\,{}^1P_1{}^2 + 0.375\,{}^3P_1{}^2 + 0.893\,{}^1D_2{}^2 + 0.446\,{}^3D_2{}^2$$

$$a_3 = -2.598\,{}^1P_1\,{}^1D_2\cos(\phi_{1D}-\phi_{1P}) + 1.500\,{}^3P_1\,{}^3D_2\cos(\phi_{3D}-\phi_{3P})$$

$$a_4 = -2.143\,{}^1D_2{}^2 + 1.429\,{}^3D_2{}^2$$

$$b_1 = -1.591\,{}^1P_1\,{}^3D_2\sin(\phi_{3D}-\phi_{1P}) - 0.919\,{}^3P_1\,{}^1D_2\sin(\phi_{1D}-\phi_{3P})$$

$$b_2 = 0.530\,{}^1P_1\,{}^3P_1\sin(\phi_{3P}-\phi_{1P}) - 0.364\,{}^1D_2\,{}^3D_2\sin(\phi_{3D}-\phi_{1D})$$

$$b_3 = 0.707\,{}^1P_1\,{}^3D_2\sin(\phi_{3D}-\phi_{1P}) - 0.612\,{}^3P_1\,{}^1D_2\sin(\phi_{1D}-\phi_{3P})$$

$$b_4 = 0.875\,{}^1D_2\,{}^3D_2\sin(\phi_{3D}-\phi_{1D}) \qquad (5.1)$$

These equations differ by a sign in the b_k coefficients from those evaluated at Stanford (King 1978).

The partial cross sections can also be analyzed in terms of jj coupling partial waves and in fact many calculations are performed in this coupling scheme. It is possible to transform from one set of equations to the other, this transformation is given by Seyler and Weller (1979). Evaluated transformation equations for spin $\frac{1}{2}^+$ on spin $\frac{1}{2}^+$ going to spin 0^+ by E1 and E2 radiation are given by McBroom (1977). These have been checked and are

$$^0T_{11} = -\frac{\sqrt{3}}{3} T_{1,1/2} + \frac{\sqrt{6}}{3} T_{1,3/2}$$

$$^1T_{11} = \frac{\sqrt{6}}{3} T_{1,1/2} + \frac{\sqrt{3}}{3} T_{1,1/2}$$

$$^0T_{22} = -\frac{\sqrt{10}}{5} T_{2,3/2} + \frac{\sqrt{15}}{5} T_{2,5/2}$$

$$^0T_{22} = \frac{\sqrt{15}}{5} T_{2,3/2} + \frac{\sqrt{10}}{5} T_{2,5/2}.$$

and the evaluated expressions for the a_k and b_k coefficients are

$$1 = 0.750(p_{1/2}^2 + p_{3/2}^2) + 1.250(d_{3/2}^2 + d_{5/2}^2) \quad \text{normalization}$$

$$a_1 = 2.372p_{1/2}d_{3/2}\cos(\phi_{p_{1/2}}-\phi_{d_{3/2}}) - 0.335p_{3/2}d_{3/2}\cos(\phi_{p_{3/2}}-\phi_{d_{3/2}}) + 2.465p_{3/2}d_{5/2}\cos(\phi_{p_{3/2}}-\phi_{d_{5/2}})$$

$$a_2 = 1.061p_{1/2}p_{3/2}\cos(\phi_{p_{1/2}}-\phi_{d_{3/2}}) - 0.375p_{3/2}^2 + 0.625d_{3/2}^2 - 0.437d_{3/2}d_{5/2}\cos(\phi_{d_{3/2}}-\phi_{d_{5/2}}) + 0.714d_{5/2}^2$$

$$a_3 = 1.936p_{1/2}d_{5/2}\cos(\phi_{p_{1/2}}-\phi_{d_{5/2}}) + 2.012p_{3/2}d_{3/2}\cos(\phi_{p_{3/2}}-\phi_{d_{5/2}})$$

$$- 1.095 p_{3/2} d_{5/2} \cos(\varphi_{p_{3/2}} - \varphi_{d_{5/2}})$$

$$a_4 = 3.499 d_{3/2} d_{5/2} \cos(\varphi_{d_{3/2}} - \varphi_{d_{5/2}}) - 0.714 d_{5/2}^2$$

$$b_1 = -1.186 p_{1/2} d_{3/2} \sin(\varphi_{p_{1/2}} - \varphi_{d_{3/2}}) + 0.681 p_{3/2} d_{3/2} \sin(\varphi_{p_{3/2}} - \varphi_{d_{3/2}})$$

$$+ 1.232 p_{3/2} d_{5/2} \sin(\varphi_{p_{3/2}} - \varphi_{d_{5/2}})$$

$$b_2 = 0.530 p_{1/2} p_{3/2} \sin(\varphi_{p_{1/2}} - \varphi_{p_{3/2}}) - 0.364 d_{3/2} d_{5/2} \sin(\varphi_{d_{3/2}} - \varphi_{d_{5/2}})$$

$$b_3 = 0.646 p_{1/2} d_{5/2} \sin(\varphi_{p_{1/2}} - \varphi_{d_{5/2}}) - 0.671 p_{3/2} d_{3/2} \sin(\varphi_{p_{3/2}} - \varphi_{d_{3/2}})$$

$$- 0.0913 p_{3/2} d_{5/2} \sin(\varphi_{p_{3/2}} - \varphi_{d_{5/2}})$$

$$b_4 = 0.875 d_{3/2} d_{5/2} \sin(\varphi_{d_{3/2}} - \varphi_{d_{5/2}})$$

The interpretation of the reaction matrix elements is not as clear in the jj coupling scheme. In the absence of spin interactions the two E1 and E2 amplitudes are expected to have similar magnitudes, whereas in the ls coupling scheme, one of the amplitudes for both E1 and E2 is expected to dominate. These terms correspond to non-spin-flip interactions where the channel spin is unchanged. This corresponds to the $^1P_1$ and $^1D_2$ amplitudes for E1 and E2 radiation respectively. The spin-flip matrix elements $^3P_1$ and $^3D_2$ are expected to be smaller in magnitude than the non-spin-flip matrix elements.

Inspection of these equations reveals that the a_2 coefficient is expected to be ~ -1 if E1 radiation is dominant, and in fact earlier measurements indicate this. Many early workers in this field have expanded the unpolarized angular distribution in terms of the

following expression

$$\sigma(\theta) = A + B\sin^2\theta + C\sin^2\theta\cos\theta + D\sin^2\theta\cos^2\theta \qquad (5.2)$$

Comparison of this expansion with that of the Legendre basis reveals several fundamental aspects of the reaction. The coefficient A is the sum $A_0+A_2+A_4$ and is expected to be small if spin-flip ($\Delta s=1$) components of the reaction are small; it is a positive sum of the partial spin-flip cross sections. This isotropic component of the angular distribution is a direct measure of these spin-flip cross sections. Implicit in this expansion, however is the constraint that $a_1 = -a_3$, which forces the product

$$^3P_1\,^3D_2\cos(\phi_{3D}-\phi_{3P}) \qquad (5.3)$$

to be zero. This product is zero if the magnitude of at least one of the spin-flip matrix elements is negligibly small. In particular, the cross section at $\theta = 0^\circ$ is equal to the cross section at $\theta = 180^\circ$ if $a_1 = -a_3$. If in addition $a_2 + a_4 = -1$, the cross section is zero at 0° and 180°. Hence, the behavior of the unpolarized angular distribution at the extreme angles is sensitive to the presence of these spin-flip $\Delta s = 1$ transitions. However, to first order the angular distribution is expected to be nearly zero at 0° and 180° and to be dominated by the $\sin^2\theta$ distribution characteristic of dipole radiation. This would correspond to $a_2 \simeq -1$. The interference of E1 and E2 radiation should produce a fore-aft asymmetry. These characteristics are used in analyzing the distribution from $^3He(n,\gamma)^4He$.

5.2 Experimental Distributions

A seven-point angular distribution of cross section and a three-point polarization asymmetry measurement was performed at a nominal neutron bombarding energy of 9 MeV, corresponding to an excitation energy of 28.1 MeV. Since the angular distribution approximately follows a $\sin^2\theta$ distribution, the counting rate is low for angles away from 90°; therefore, in order to compensate for this, the deuterium cell length was increased to 5.1 cm. This had the effect of increasing the yield of neutrons, however, the energy spread of the neutron flux was also increased by the greater energy loss of the deuterons in traversing the cell. In this case, the energy loss of the E_d = 6.15 MeV deuterons was 770 KeV at 6 ATM for the production of 9 MeV neutrons.

The observed laboratory cross sections were converted to the center-of-mass frame by equations derived from the proper relativistic formulation (Jackson, 1962). The finite geometry correction to this data set was applied as described in section 4.3. The first guess for the true cross section was made by least-squares fitting the observed angular distribution with Legendre polynomials with the fit constrained to be near zero at $\theta = 0^\circ$ and 180°. The reduced coefficients and errors are shown in table 5-1a. Table 5-2 contains the yield as a function of laboratory scattering angle, the correction ratio and the corrected yields. The errors are statistical only and

Table 5-1 Fits of Legendre polynomials to the experimental unpolarized angular distribution at E_n = 9.0 MeV. The reduced chi square and the a_k coefficients are shown for the a) constrained, uncorrected data, and the corrected data b) constrained and c) unconstrained at 0 and 180 degrees.

χ^2_ν	a_1	Δ	a_2	Δ	a_3	Δ	a_4	Δ
a)								
1.16	-0.141	0.039	-0.892	0.046	0.121	0.046	-0.075	0.050
1.37	-0.143	0.039	-0.944	0.033	0.122			
b)								
1.02	-0.136	0.038	-0.929	0.045	0.122	0.043	-0.047	0.047
1.01	-0.138	0.038	-0.964	0.028	0.123	0.043		
c)								
0.503	-0.176	0.044	-0.875	0.073	-0.009	0.086	-0.018	0.109
0.344	-0.174	0.043	-0.881	0.062	-0.006	0.085		
0.259	-0.174	0.042	-0.882	0.061				

Table 5-2 E_n = 9.0 MeV unpolarized angular distribution yields. They are normalized to 9.0 mCoul integrated charge and 100.2 cm detector-to-target distance. The points shown at 0^o and 180^o were used to constrain the Legendre polynomial fit. The correction factor arises from the finite geometry averaging only as discussed in the text.

Angle	N	Δ	C(θ,9.0)	N.C	Δ.C
0.0	5.4	10.0		5.4	15.0
30.0	71.2	12.1	1.14	81.2	13.8
55.0	184.0	13.6	1.23	226.3	16.7
70.0	259.8	16.8	1.24	322.4	20.9
90.0	274.2	15.6	1.24	341.1	19.4
90.0	270.6	14.9	1.24	336.6	17.3
110.0	253.3	17.2	1.24	312.8	21.2
125.0	199.8	12.6	1.21	242.2	15.3
145.0	133.4	13.4	1.14	152.1	14.9
180.0	4.7	10.0		4.7	15.0

do not reflect any normalization or correction error. Inspection of the a_k coefficients obtained from the corrected distribution reveals the nature of the correction. The a_2 coefficient is increased slightly in magnitude and the a_4 coefficient is reduced. The increase in a_2 arises from the fact that the experimental distributions are angle averaged over the ~18° acceptance angle of the system, and the sharp peaking near 90° of P_2 is not fully observed. The effect of the correction on the fore-aft asymmetry is very small and has been previously checked using the $^{12}C(n,n'\gamma)$ reaction (Wender 1978). No corrections have been made for the effects of the steel vessel, any correction from this should not affect the angular distribution significantly. Since the gaseous ^3He target has a low density, the effect of attenuation and multiple scattering can be safely neglected.

Since the cross section is expected to be very nearly zero at 0° and 180°, the experimental yield was fit to the Legendre polynomials using a weighted chi square (χ^2) minimization routine. To effect the constraint, fictitious data points with large errors were introduced at those angles. The curves shown in figure 5-1 reflect the fit with and with out the constraint. This is, of course, consistent with the analysis contained in section 5.3 which neglects the E2 spin-flip matrix element. Inspection of the normalized coefficients in table 5-1b,c reveals the effect of the constraint; a_1 and a_2 are reasonably stable, but the constraint forces a_3 and a_4 to increase.

The analyzing power data were normalized so that the sum $(N_+ + N_-)$ was equal to the fit of the geometry-corrected $\sigma(\theta)$ data at

Figure 5-1 Angular distribution of cross section at E_n = 9 MeV.

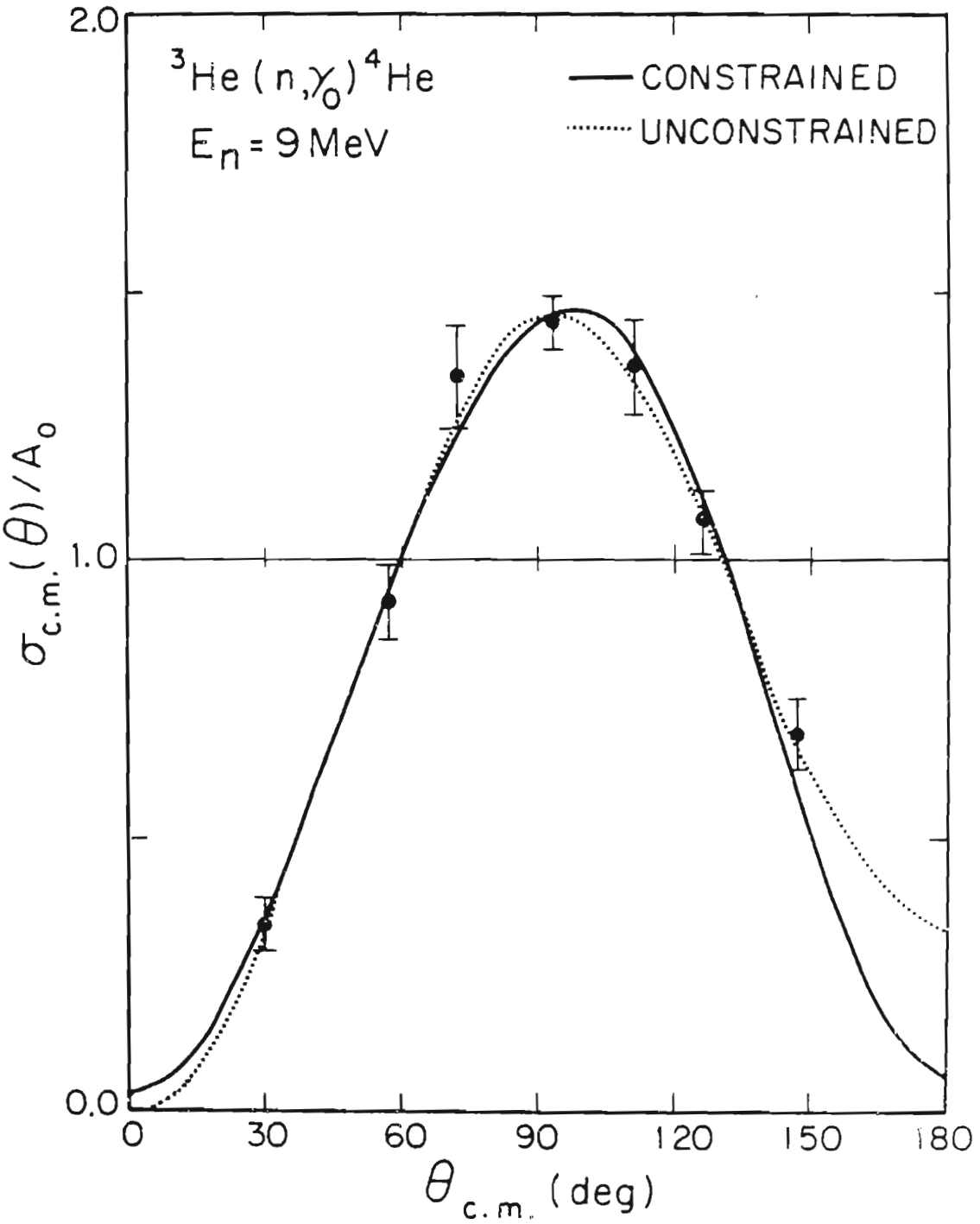
$^3He(n,\gamma_0)^4He$
$E_n = 9$ MeV
CONSTRAINED
UNCONSTRAINED
2.0
1.0
0.0
$\sigma_{c.m.}(\theta)/A_0$
0
30
60
90
120
150
180
$\theta_{c.m.}$ (deg)

the measured angles $\theta_{LAB} = 55^{o}, 88^{o}, 125^{o}$. Yields from these measurements are shown in table 5-3. No attempt was made to correct the individual $A(\theta)$ data for geometry, multiple scattering or attenuation effects. The correction to $A(\theta)$ due to the finite geometry has been shown to be of the order of a few percent (Jensen 1980). This correction is especially small in this case since the asymmetry is small. The effect of the multiple scattering in the steel has been investigated by Lisowski (1978) who found this correction also to be small. It is possible that further attempts to improve the variance of the data will warrant closer scrutiny of these effects.

Since only the b_2 coefficient is expected to be significant, the $A(\theta)\cdot\sigma(\theta)/A_0$ data were fit to $b_2 P_2^1$. The results of this fit are shown below.

Table 5-4 Coefficients and standard deviations from fit of Associated Legengre polynomials to polarized asymmetry data. Also indicated are the a_k coefficients which were used to determine $\sigma(\theta)$. The reduced chi-square for this fit is 0.152.

k	1		2		3		4	
a_k	-0.137	0.038	0.939	0.045	0.125	0.044	-0.049	0.049
b_k			0.057	0.039				

Table 5-3 Polarized beam angular distribution yields at E_n = 9.0 MeV. The sign listed under z indicates the alignment of the polarization in either the positive or negative z direction in the spin filter cavity in the polarized ion source. The yields are normalized to the constrained fit to the unpolarized data.

Angle	z	N	Δ	p_y	Norm N	Δ
55	+	108.0	11.9	0.62	110.7	12.2
	−	116.0	12.2		118.9	12.5
88	+	135.7	12.4	0.62	168.3	15.4
	−	137.1	12.3		170.0	15.2
125	+	143.0	13.1	0.63	131.3	10.9
	−	126.3	12.6		116.0	12.0
55	+	88.8	6.9	0.60	110.7	8.6
	−	95.3	7.1		18.8	8.8
88	+	126.0	9.6	0.59	165.2	12.6
	−	132.0	9.9		173.1	13.0
125	+	122.0	8.2	0.64	130.1	8.7
	−	110.0	7.6		117.3	8.1

5.3 Matrix Element Analysis

Information on the reaction matrix elements is useful not only for comparison to calculation, but also to shed light on the analysis of the ratio of the $^4He(\gamma,p)^3H$ cross sections. Specifically, one might ask how the other reaction partial waves compare in these two reactions, especially when the dominant $^1P_1$ cross section is dramatically different. Unfortunately, the statistical variance of the polarized asymmetry data does not allow us to make a thorough analysis of the spin-flip strength, but we are provided with an indication of the behavior. The triplet E2 amplitude has been arbitrarily set to zero, since we do not have enough information to determine it. The analysis of King (1978) seems to indicate an extraordinarily large $^3D_2$ amplitude, however its relative phase is apparently indeterminate. Previous experiments and calculations (Halderson and Philpott, 1979) have assigned a negligible strength to this matrix element.

In this analysis, the amplitudes and phases were fit directly to the data so that a proper evaluation of the errors would be possible. The fitting program used was a weighted non-linear least squares minimization routine. The fictitious data points at 0^o and 180^o were unnecessary since the constraint of $^3D_2 = 0$ was sufficient both to force the cross section to be positive at all angles and to produce $a_1 = -a_3$. Since the triplet E1 amplitude was allowed to vary from

zero, the fitted cross section is not necessarily zero at 0^{o} and 180^{o}. Table 5-5 indicates the resultant amplitudes and phases. The large error assigned to the $^{3}P_{1}$ matrix element is presumably due to the lack of polarization asymmetry data. The $^{3}He(\vec{p},\gamma)^{4}He$ analysis indicated the sensitivity of the ϕ_{3P} to the b_{3} coefficient (and thus also to the b_{1} coefficient in this case). By fixing this phase to that obtained in the (p,γ) case and also to the minimum found here, one sees that this does not affect the quality of the fit nor does it significantly affect the solution in terms of the other amplitudes and phases.

In an effort to analyze the surprisingly large error in the $^{1}D_{2}$ amplitude an F-test was applied to the chi square for the inclusion of the $^{1}D_{2}$ amplitude and phase. By analogy to the development of Bevington (1969) for the inclusion of one term, the two term test was formulated. The test is used to determine the necessity of inclusion of the E2 term in the fitting function. The chi-square associated with the fit for n-2 terms is $\chi^{2}(n-2)$ with $v = N-n-2$ degrees of freedom, where N is the number of data points. The difference $\Delta\chi^{2}() = \chi^{2}(n-2)-\chi^{2}(n)$ also follows the χ^{2} distribution with two degrees of freedom. The ratio of the reduced difference chi-square over the new reduced chi-square

$$F_{\chi} = \frac{\Delta\chi^{2}()}{\chi^{2}_{v}} = \frac{(\chi^{2}(n-2)-\chi^{2}(n))/2}{\chi^{2}(n)/(N-n)}$$

follows the f distribution, and is a measure of the improvement in χ^{2} when the new terms are added. In the case of fitting the angular

Table 5-5 Values of partial cross section and phase obtained by least squares fitting to the $\sigma(\theta)$ and $A(\theta)\cdot\sigma(\theta)/A_0$ experimental distributions. Also indicated, as the last set is the result found by fitting to the Legendre coefficients. Also indicated is the reduced chi-square for each fit. Those entries which have no error indicated were constrained to be that particular value in the fitting procedure. The partial cross sections are given in percent of the total capture cross section.

χ^2_ν	$^1P_1$	Δ	$^3P_1$	Δ	$\phi_{3P}-\phi_{1P}$	Δ	$^1D_2$	Δ	$\phi_{1D}-\phi_{1P}$	Δ
0.891	95.96	3.26	1.01	3.19	130.1	111.9	3.03	3.22	107.0	10.5
0.742	95.95	3.15	1.12	1.38	130.0	-	2.93	2.65	107.3	9.4
0.796	96.00	3.15	1.067	1.43	50.0	-	2.93	2.67	107.4	9.4
0.682	96.06	2.86	1.03	1.34	50.0	-	2.91	1.39	107.4	-
1.266	96.15	2.88	1.32	1.55	50.0	-	2.54	0.875	120.0	-
0.637	95.85	3.09	1.12	-	130.0	-	3.028	2.48	107.0	8.5
2.70	97.97	6.81	2.03	7.90	33.5	76.7	0.0	-	0.0	-
0.064	95.67	3.19	1.61	4.68	38.0	71.1	2.72	2.75	107.6	10.0

distribution data without the E2 terms $\chi^2 = 18.9$ and $v = 7$. Inclusion of this term yields $\chi^2 = 4.45$. with $v_2 = 5$. The value of F_χ is 8.1 which exceeds the 95% probability F. This result indicates that the E2 amplitude and phase should be included in fitting the observed angular distributions, despite the fact that the error in the $^1D_2$ amplitude would indicate that this amplitude is not significant. A more definitive analysis of the relative amplitudes and phases is clearly desirable, for which lower experimental errors are needed.

6. ANALYSIS OF RESULTS

In this chapter the total cross section as well as the experimental ratio of the $^4He(\gamma,p)^3H$ to $^4He(\gamma,n)^3He$ cross section is presented. Comparison of the partial reaction matrix elements and relative phases for these reactions at $E_n = E_p = 9$ MeV is also made. The relative cross sections and relative phases are compared to a direct capture calculation. The ratio is then analyzed by comparison to two calculations, one using a direct plus charge exchange model, the other using a recoil corrected continuum shell model.

The Direct model provides no mechanism for $R \neq 1$ except near the thresholds ($E_\gamma \lesssim 24$ MeV). In an effort to analyze the possible mechanisms that might account for the ratio of the (γ,p)-to-(γ,n) cross section being different from unity, a coupled channels calculation allowing a direct-plus-charge exchange reaction mechanism is presented. Recent shell model calculations indicate that as yet no mechanism as currently applied succeeds in explaining the inequality of the photodisintegration cross sections. To investigate the sensitivity of this ratio to the details of the parameters in shell model calculations, these parameters were varied in a continuum shell model calculation. The results demonstrate the difficulty in applying this technique to the ^4He well.

6.1 Experimental Results

6.1.1 Integrated Cross Sections

In order to use capture cross sections to compare the corresponding photodisintegration cross sections, they must be converted using the principle of detailed balance(reciprocity theorem). This procedure follows from the symmetry of the transition matrix (e.g. Feshbach, 1960), and involves only spin and linear momentum. For the case of calculating photoproduction cross sections $\sigma(\gamma,p_0)$ from radiative capture cross sections $\sigma(p,\gamma_0)$ the expression is given by (Buttlar, 1968; Fuller and Hayward, 1962)

$$\sigma_{\gamma,p_0} = \frac{2I_{A-1}+1}{2I_A+1}\,\frac{A'-1}{A'}\,\frac{2Mc^2}{E_\gamma^2}\,[E_\gamma - (SE)_p]\sigma_{p,\gamma_0} \qquad (6.1)$$

where the number of nucleons in the target nucleus (A) of the (γ,p) process differs by one from the target nucleus (A-1) of the (p,γ) process; I_A and I_{A-1} are the spins of nucleus A and A-1, respectively. $(SE)_p$ is the separation energy of the proton, and M is the nucleon rest mass.

The total cross section was inferred from our differential ($\theta_{LAB} = 90^o$) cross section by using the relation $\sigma_T = (8\pi/3)\,\sigma(90^o)$. The integrated cross section obtained in this way is essentially a dipole cross section. However, the presence of a small amount of E2 radiation will not greatly affect its validity since the E1 - E2

interference term vanishes at $\theta = 90^{\circ}$. This is seen by inspection of equation (5.2) for A = D = 0. If on the other hand a large amount of E2 radiation is present it will contribute directly and the coefficient D will be nonzero. Other multipoles such as M1, M2 or $\Delta S = 1$ E1 can cause the coefficient A to be nonzero. The relation's validity was verified at $E_n = 9$ MeV by our angular distribution measurement. The 90°_{LAB} ($\theta_{CM} = 92^{\circ}$) point in the relation $\sigma_T = 8\pi/3\ \sigma(90^{\circ})$, gives $\sigma_T = 41.9 \pm 1.6$ μb. The integrated cross section deduced from the Legendre fit using the relation $\sigma_T = 4\pi A_0$ is $\sigma_T = 43.5 \pm 2.1$ μb. Both of these cross sections have an absolute normalization which is derived from the yield curve measurement. The electric quadrupole transition strength increases with increasing energy, so that this relation will not well represent the integrated cross section at much higher excitation energies (for proton capture see for instance R.C. McBroom et al. (1980)).

Figure 6-1 indicates our inferred total photoneutron cross section as a function of excitation energy in ^{4}He. Also shown is the recent photoneutron data of Berman et al. (1980) (BFM), the detailed balanced data of Meyerhof et al. (1970) (MSF) and the cloud chamber data of Balestra et al. (1977) (BBB).

The data of BFM were obtained with a gaseous ^{4}He target, monoenergetic photons, and a 4π neutron detector. The gaseous target and monoenergetic beam eliminate much of the suspected cause of inconsistency in the earlier measurements. A systematic uncertainty of 10% or less is claimed by BFM for these data. The degree of agreement between this data set and the present one is exceptional.

Figure 6-1 Angle-integrated photodisintegration cross sections. Filled circles indicate intetegrated, detailed balanced data of present work. Crosses indicate recent total photoneutron measurement of BFM (Berman et al., 1980). Angle-integrated, detailed balanced proton capture data of MSF (Meyerhof et al., 1970) are represented by the solid circles, and cloud chamber photoproton data of BBB (Balestra et al., 1977) is represented by open circles.

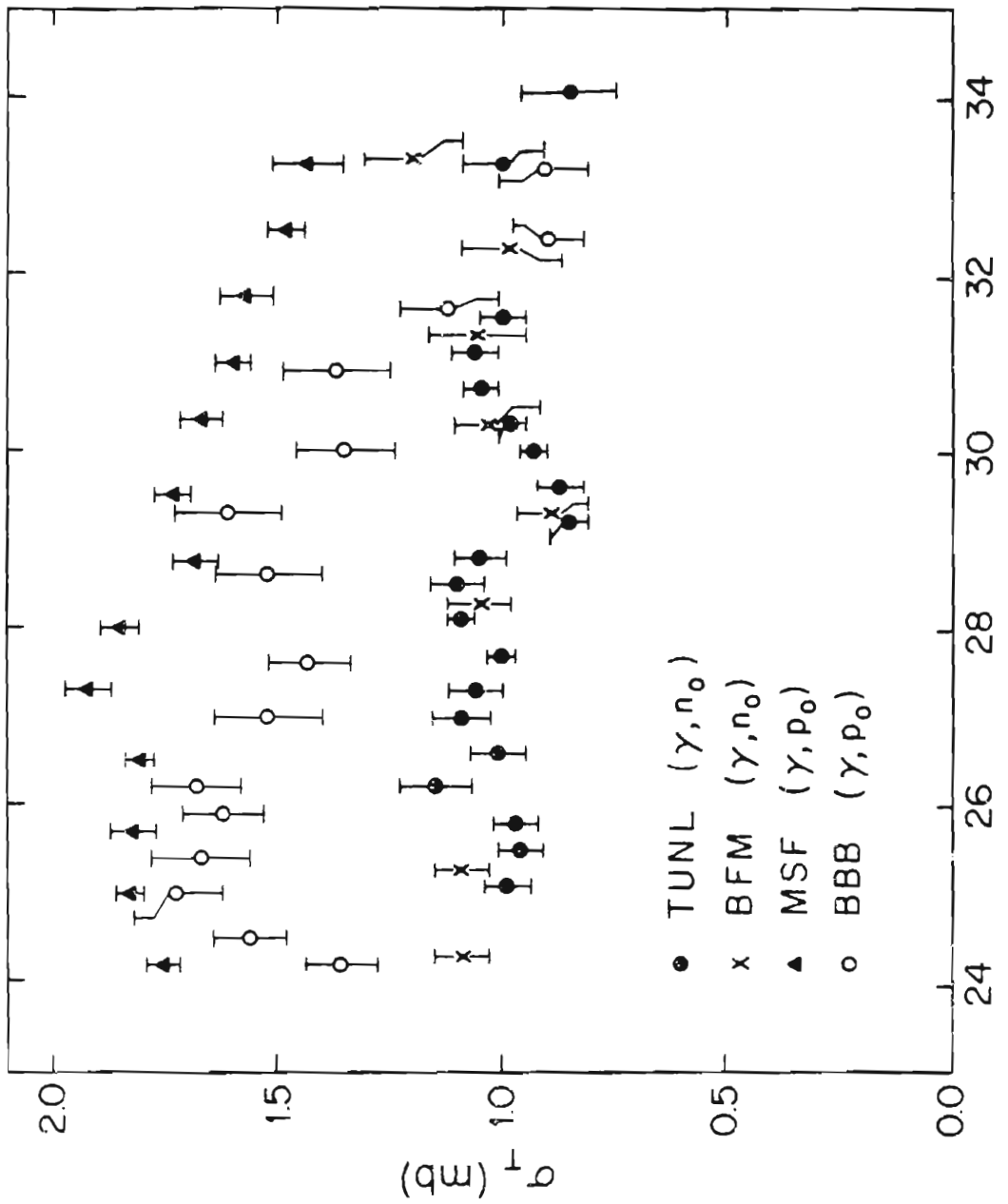
2.0
1.5
1.0
0.5
0.0
σ_τ (mb)
24
26
28
30
32
34
E_x (MeV)
• TUNL (γ, n_o)
x BFM (γ, n_o)
▲ MSF (γ, p_o)
o BBB (γ, p_o)

These experiments involve vastly different technologies yet the results are well within the experimental uncertainties.

It is important to note that the absolute scale of the MSF data is determined by normalization in the region of 4–6 MeV to the data of Perry and Bame (1953). Their method of determining the angle integrated cross section differed from the present work in that they subtracted out the isotropic component of the angular distribution which would arise from $\Delta S = 1$ transitions. However, this amounted to less than a 2% effect.

The photoproduction data of BBB were obtained with an 85 MeV bremsstrahlung beam incident on a 5 ATM He-filled cloud chamber. They obtained $^4He(\gamma,p)^3He$ and $^4He(\gamma,n)^3He$ cross sections of which only the former are shown. These data exhibit the same peak value of the cross section but tend to drop more rapidly than the result inferred from the MSF data. It should be pointed out that the BBB data presented here is their total $^4He(\gamma,^3H)$ cross section.

The (γ,p) data sets presented here are fairly representative of the available (γ,p) results and are intended to demonstrate the variation in shape which exists among the photoproduction data sets. As for the (γ,n) results presented, the present data have a 15% total error and the BFM data have a 10% error assigned to them. Therefore, this result is in contradiction to those measurements of the (γ,n_0) cross section which indicate a peak value of ~ 1.7 mb. See section 2.1 for a discussion of these data sets.

It can be seen that the (γ,p)-to-(γ,n) cross section ratio (R) indicated by these data is non unity in this region as indicated by

figure 6-2. The ratio of the MSF and BBB (γ,p) data to the (γ,n) data of the present study is shown. The uncertainty in this ratio, of course, depends upon the uncertainties in the constituent measurements and is of the order of 25%. These measurements however, indicate a trend in which the ratio has a maximum value of 1.6 to 1.8 near 25 MeV and drops to a value of ~ 1 in the vicinity of 34 MeV. Also shown in this figure are the ratio data of BBB, Dodge and Murphy (1972) (DM), and Philips et al. (1979) (PBF). The DM data were reanalyzed by PBF; it is those reanalyzed data points which are shown.

The ratio formed from the MSF and TUNL data is in some respects the more reliable since both were obtained from capture reactions with similar technologies. However, the shape of this curve is possibly its least known feature. Errors in detection efficiencies as a function of energy could lead to 10-20% shifts from one end of the range to the other. The ratio formed in this manner represents that due to the dipole strength only below 34 MeV; this should compare well with the ratio from the total integrated cross section. At higher energies electric quadrupole radiation becomes more significant and enters directly, not just as E1-E2 interference. The latter three data sets are direct measurements of R, in which $\sigma(\gamma,n)$ and $\sigma(\gamma,p)$ are measured simultaneously. BBB present a value of R which exceeds one, but not to the degree that our data would indicate. The most recent data of Arkatov et al. (1978) indicate a value of R = 1.3 at E_x = 26 MeV. These cloud-chamber data are extremely difficult to analyze at the lower energies due to the short range of the recoils. Both DM and PBF could not obtain values of R below 31 MeV, but obtain

Figure 6-2 Ratio, R of $^4He(\gamma,p)^3H$ to $^4He(\gamma,n)^3He$ cross section. Filled circles indicate ratio of MSF to present data, and open circles ratio of BBB to present data. Direct measurements of R: hourglass-shaped symbols represent ratio from BBB, filled squares indicate DM (Dodge and Murphy, 1972) data which was reanalyzed by PBF (Phillips et al., 1979) and diamond-shaped symbols represent values obtained by PBF.

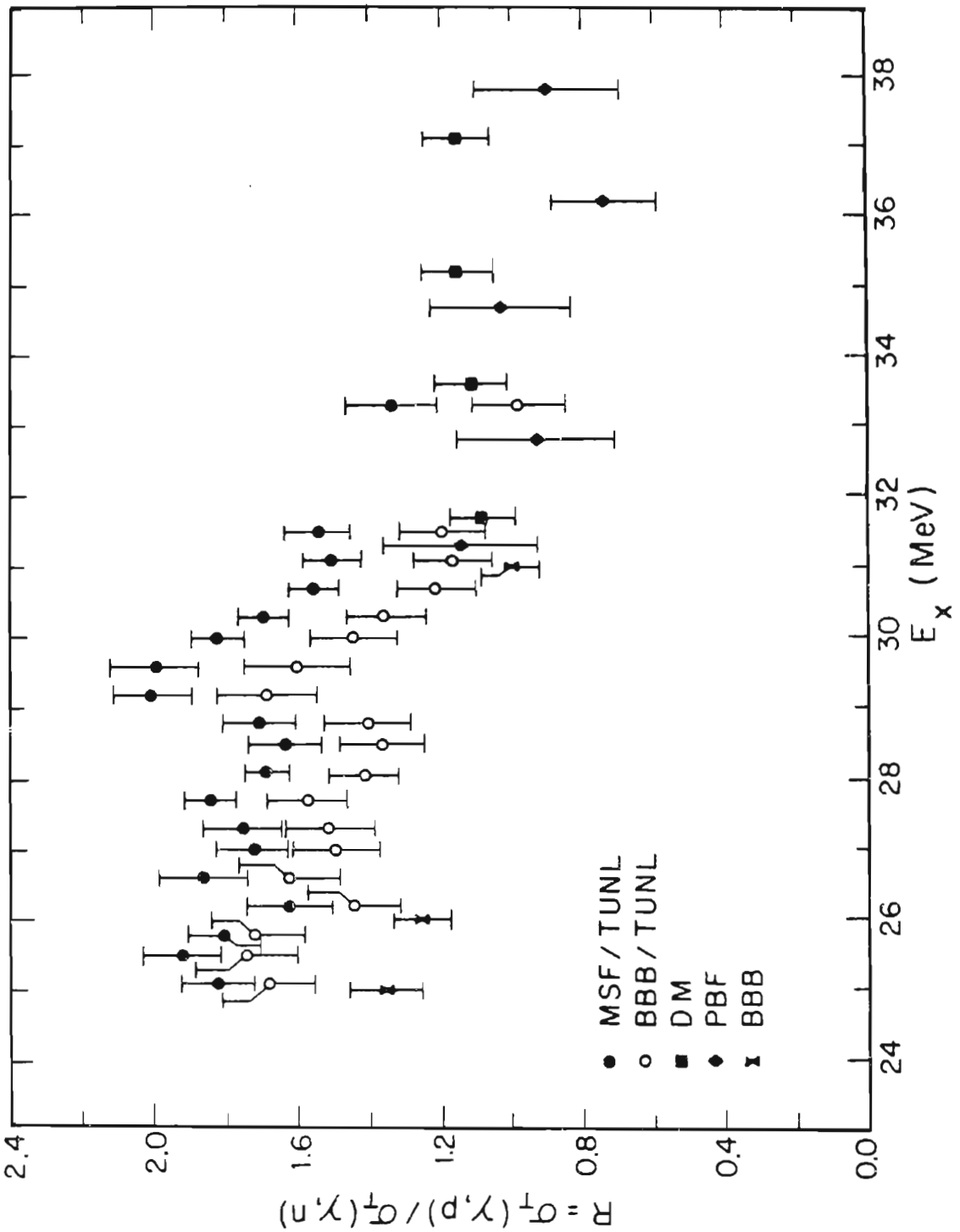
R = σT (γ,p) / σT (γ,n)
2.4
2.0
1.6
1.2
0.8
0.4
0.0
24
26
28
30
32
34
36
38
Ex (MeV)
MSF / TUNL
BBB / TUNL
DM
PBF
BBB

values slightly greater than one above this energy. They rely on angular distribution coefficients of the photodisintegration reaction for determining the integrated cross section. PBF reevaluated the DM result using a "consensus set" of coefficients to obtain the integrated cross section ratios from the measured $90^{o}3_{He-LAB}$ ratios. The ratio inferred from the present data is in agreement (within errors) with these measurements which indicate that the ratio is unity at ~ 34 MeV. The inferred ratio is 1.6 to 1.8 below ~ 30MeV.

6.1.2 Amplitudes and Phases

Any mechanism which would cause these two cross sections to be different by a factor of 1.6 to 1.8 must be operative through the dominant $^{1}P_{1}$ amplitude since it accounts for ~ 97% of the cross section. It is quite possible that an understanding of this mechanism is obtainable through an investigation of the other reaction matrix elements. A pertinent question is how these other partial cross sections and relative phases compare in the case of $^{3}H(p,\gamma_{0})^{4}He$ and $^{3}He(n,\gamma_{0})^{4}He$ when the dominant partial cross section must be different by about a factor of 1.6 to 1.8. A detailed study of the angular distribution of cross section and analyzing power times cross section has been made at Stanford (King, 1978). These data, together with the results of the present experiment allow this type of comparison.

The Stanford data taken at E_{p} = 9 MeV seem to be more consistent with the general trend of the amplitudes and relative phases with energy than the E_{p} = 9.8 MeV data. The 9.8 MeV data, however would correspond more nearly to the same excitation energy in ^{4}He as that of our mean neutron energy of 9 MeV. However, there is no sharp (~1 MeV)

structure expected in the excitation of a light nucleus such a ^{4}He, and there was none observed in either the (p,γ) or the current experiment.

Figure 6-3 shows the distribution of cross section and analyzing power times cross section divided by A_0 for the two reactions ^{3}H(p,γ_0)^{4}He and ^{3}He(n,γ_0)^{4}He. Also indicated are the coefficients obtained from Legendre fits to the experimental distributions. It is important to point out that while the Legendre fit to the (n,γ) distribution was artificially constrained at 0^o and 180^o, the (p,γ) data set includes a point at 0^o and no constraint at 180^o. Both unpolarized cross sections reflect the predominant $\sin^2\theta$ distribution characteristic of $\Delta S = 0$ E1 radiation; the interference of $\Delta S = 0$ E1 with $\Delta S = 0$ E2 radiation is evident in the a_1 and a_3 angular distribution coefficients. They are opposite in sign and nearly equal in magnitude for the two reactions. This may be understood in terms of the reaction models which are discussed in later sections.

The b_2 coefficient is sensitive to the presence of spin-flip strength. This can be seen in equation (5.1). The relative $^3P_1$ phase should be nearly the same for the two reactions; this amplitude arises from a spin-orbit interaction which should be similar for the two reactions. Polarization asymmetries for the two reactions indicate a very similar spin-flip amplitude.

The extracted amplitudes and relative phases, shown in table 6-1 enable a comparison of the two experiments. Procedures for analysing the present data are discusssed in section 5.2. Since the (n,γ_0) data were analyzed with no $^3D_2$ amplitude, the (p,γ_0) amplitudes and

Figure 6-3 Angular distributions for $^{3}He(\vec{n},\gamma_0)^{4}He$ and $^{3}H(\vec{p},\gamma_0)^{4}He$ reactions at E_n = Ep = 9 MeV.

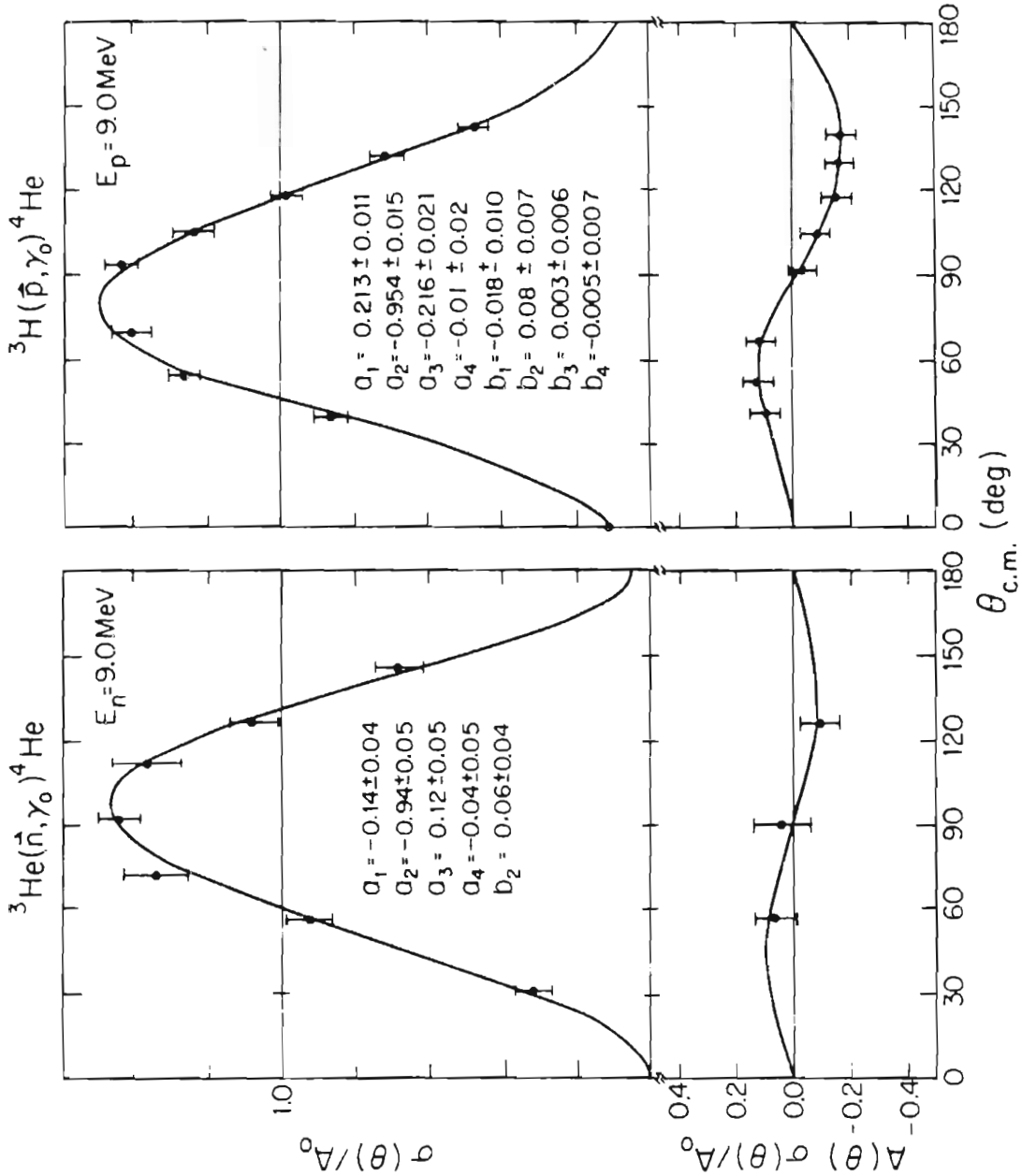
^{3}He($\vec{n}$,γ_0)^{4}He
E_n=9.0MeV
a_1 = −0.14±0.04
a_2 = −0.94±0.05
a_3 = 0.12±0.05
a_4 = −0.04±0.05
b_2 = 0.06±0.04
^{3}H($\vec{p}$,γ_0)^{4}He
E_p=9.0MeV
a_1 = 0.213±0.011
a_2 = −0.954±0.015
a_3 = −0.216±0.021
a_4 = −0.01 ± 0.02
b_1 = −0.018± 0.010
b_2 = 0.08 ± 0.007
b_3 = 0.003± 0.006
b_4 = −0.005±0.007
$\sigma(\theta)/A_0$
$A(\theta)\ \sigma(\theta)/A_0$
$\theta_{c.m.}$ (deg)

Table 6-1 Comparison of partial cross sections and phases for $^3He(\vec{n},\gamma_0)^4He$ and $^3H(\vec{p},\gamma_0)^4He$ at Ep = E_n = 9 MeV. The second Stanford data set is from a fit to their a_k and b_k coefficients with a $^3D_2$ amplitude of zero; the third consists of energy averaged values which more nearly reflect the general trend of the data. The results of a direct-capture calculation are included.

$^1P_1$	$^3P_1$	$\phi_{3P}-\phi_{1P}$	$^1D_2$	$\phi_{1D}-\phi_{1P}$	$^3D_2$
Experimental					
TUNL (n,γ)					
96.0 (3.2)	1.1 (1.4)	50 (-)	2.9 (2.7)	107 (9)	
Stanford (p,γ)					
97.5 (1.7)	1.7 (0.2)	62 (11)	1.1 (0.1)	-32 (9)	0.6 (0.6)
96.5 (0.9)	2.3 (1.0)	48 (14)	1.2 (0.6)	-42 (17)	
97.5	1.7	59	1.8	-57	0.9
Direct calculation					
(n,γ)					
98.8	1.2	-110	1.2X10-3	116	
(p,γ)					
98.0	1.1	-115	4. X10-2	-63	

relative phases were fit to the a_k and b_k coefficients with the constraint that the $^3D_2$ amplitude be zero. This constraint however does not significantly change the other amplitudes and relative phases as is seen in the table. For each of these reactions there are two solutions in which the $^3P_1$ and $^1D_2$ relative phases shift by about 90^o and 190^o respectively. The solutions which are presented are chosen so that the $^3P_1$ phase is approximately equal for the two reactions.

6.2 Comparison to Theory

6.2.1 Direct calculation

An analysis of these reactions may be performed within the framework of a direct-capture calculation. Interpretation of relative amplitudes and relative phases may be effected through a comparison of experimental values to calculated ones; the magnitude of the cross section may also be compared with theory although with less certainty because of its sensitivity to the model parameters. Nevertheless, the fact that a direct-capture mechanism describes the reaction was observed as early as 1951 when Gunn and Irving (1951) and Flowers and Mandl (1950) produced the essential features of the $^4He(\gamma,p)^3H$ cross section using gaussian wave functions. Many authors have posed the question of whether the photodisintegration proceeds through a direct or resonant mechanism (Meyerhof, 1980; Barker and Mann, 1957).

Our analysis shows that the direct mechanism exhibits a single particle resonance-like structure, and a more appropriate question is

whether the reaction is direct or direct-plus-other-resonances. The general features of the direct capture cross section follow from the opening up of the channel resonance which produces the rise in cross section followed by an asymptotic tail at higher energies.

Direct capture is the process in which an incoming nucleon undergoes a radiative transition from the continuum scattering state to a single-particle state in the residual nucleus (Rolfs, 1973). This is discussed in the review by Weller and Roberson (1980). The radial part of the transition amplitude is calculated as

$$\langle u_b | d^L | \chi^{(+)} \rangle$$

Here u_b is the radial wave function of the nucleon in the residual bound state, $\chi^{(+)}$ is the continuum state calculated using the optical model potential. The radial part of the single-particle electromagnetic operator of multipolarity L is represented by d^L. The calculation was performed using the code Radcap (Cotanch, 1979). Incident partial waves were computed using the optical model parameters of Lisowski (1973) obtained from a fit to polarized neutron scattering by ^{3}He. The form of the radial potential was

$$V(r) = V_C(r) + V_N(r) + W_N(r) + V_{SO}(r)\ \vec{l}\cdot\vec{S} \qquad (6.1)$$

with V_C, the coulomb potential, that of a uniformly charged sphere. A Woods-Saxon potential was used for the real central potential

$$V_N = V_0\ f(r, r_0, a_0)$$

with form factor

$$f(r,r_0,a_0) = \left[1 + \exp[(r-r_0)/a_0] \right]^{-1}.$$

A surface-derivative form was used for the imaginary potential

$$W_N(r) = 4i\, a_I\, W_D \frac{d}{dr} f(r,r_I,a_I)$$

The spin orbit potential was

$$V_{SO}(r) = \frac{-\lambda_{SO}}{45.2} \frac{1}{r} \frac{d}{dr} V_N(r,r_{SO},a_{SO})$$

The parameter set used was Lisowski's solution for a neutron bombarding energy of E_n = 9 MeV as is indicated in table 6-2. Additionally, for the (p,γ) calculation, the coulomb radius was taken to be r_C = 1.3.

Eigenfunction solutions were computed for the bound state potential which satisfied the correct angular momentum and binding energy requirements. The parameters are shown in table 6-2. The overlap of these wave functions through the E-M operator with the continuum wavefunctions from the optical potential was computed to evaluate the transition matrix element for E1 and E2 radiation. The kinematic effective charges for EL radiation were computed according to the relations

$$Q_p = e\frac{1}{A^L} \left[(A-1)^L + (-1)^L(Z-1) \right],$$

and

Table 6-2 Parameters used for Direct calculation. a) Optical model parameters from n-^{3}He scattering. b) Parameters for bound-state calculation.

a)

V_0	= 57.2	W_D	= 1.9	λ_{SO}	= 5.47
r_0	= 1.25	r_I	= 1.75	r_{SO}	= 1.4
a_0	= 0.55	a_I	= 0.55	a_{SO}	= 0.65

b)

V_{WS}	= 64.2	r_{WS}	= 1.4	a_{WS}	= 0.65
V_{SO}	= 1.73	r_{SO}	= 1.4	a_{SO}	= 0.65

$$Q_n = eZ \left[-\frac{1}{A} \right]^L$$

For the case of capture to ^{4}He the effective charges are for E1: $Q_p = 1/2$, $Q_n = -1/2$, for E2 radiation $Q_p = 5/8$ and $Q_n = 1/8$. This result immediately implies that except for kinematic and penetrability factors the (dominant) E1 capture cross section for protons and neutrons going to ^{4}He are equal in magnitude except for Coulomb effects. This leads one to expect that any calculation using this model will produce proton and neutron cross sections which are about equal in the range of 24 to 34 MeV. This result can be seen in figure 6-4. Other ramifications of the effective charge are seen in the E2 cross sections. The ratio of the partial E2 cross section ($^1D_2$) of (p,γ) to (n,γ) should be about five. This is not borne out by experiment. Inspection of table 6-1 reveals this discrepancy. Of course, the large error in the (n,γ) $^1D_2$ amplitude precludes a firm analyses based on this point; one fifth of the (p,γ) $^1D_2$ amplitude is within the error of the (n,γ) $^1D_2$ cross section. However, both of them are larger in magnitude than the direct calculation would suggest. On the other hand, the agreement with the experimental relative phases is fairly good. The 180^o change in sign of the $^1D_2$ relative phase from (p,γ) to (n,γ) follows from the difference in sign of the effective charge for E2 radiation.

With regard to the E1 spin-flip matrix element, the direct calculation based on the optical model of Lisowski overestimates its magnitude. The spin orbit well depth was changed from $\lambda_{SO} = 9.80$ to $\lambda_{SO} = 5.47$ to more nearly reproduce the experimental (p,γ) b_2

Figure 6-4 Direct and direct-plus-charge-exhange calculations of photoproton and photoneutron cross sections.

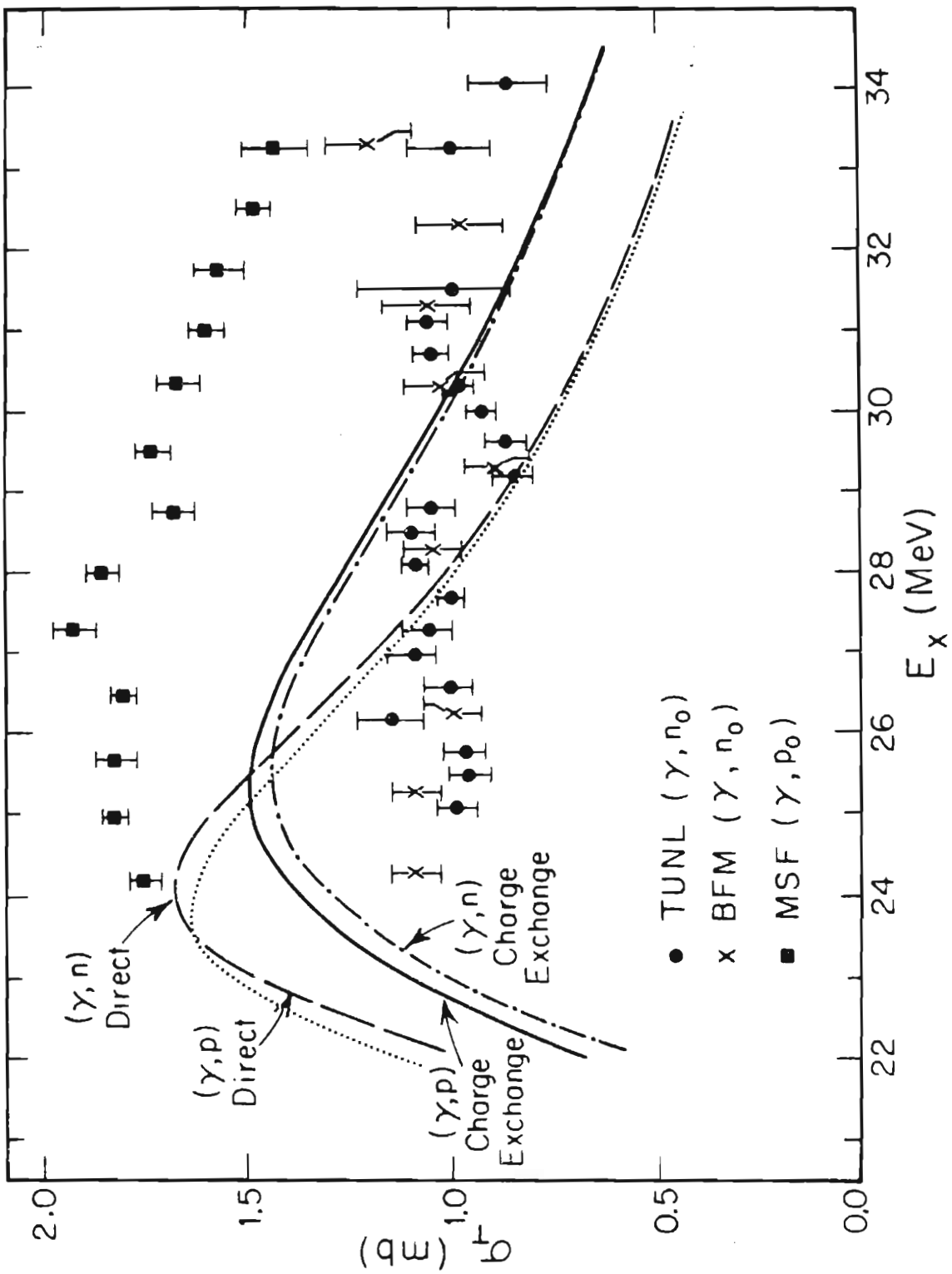
2.0
1.5
1.0
0.5
0.0
σ_T (mb)
22
24
26
28
30
32
34
E_x (MeV)
(γ,n) Direct
(γ,p) Direct
(γ,p) Charge Exchange
(γ,n) Charge Exchange
• TUNL (γ, n_o)
x BFM (γ, n_o)
■ MSF (γ, p_o)

coefficient. This produces agreement (within the large experimental error) with the (n,γ) result.

Much smaller errors in the case of the (n,γ) reaction must be obtained before definite conclusions about the ratio of the cross sections can be drawn from these reaction matrix elements. A useful analysis of these reactions lies in the comparison of the partial cross sections. Since the $^1P_1$ amplitude contributes ~ 97% of the cross section in both reactions, the effect which produces the ratio of 1.6 to 1.8 must operate through it. The other, smaller amplitudes may or may not exhibit this ratio of the two reactions.

In order to understand the resonant nature of the direct-capture process, an analysis of the optical model used to compute the distorted wave was performed. Investigation of the scattering phase shifts as a function of energy allows a demonstration of this channel resonance. Scattering phase shifts were calculated using the program Optics7A from the Lisowski optical model; the phase shifts as a function of bombarding energy were then converted to cross sections using the program Shoz. Figure 6-5 shows the behaviour of the absorption parameter and real phase shift along with the total scattering cross section for $\ell = 1$ as a function of energy. The rise in the capture cross section at $E_p = 5$ MeV corresponds to the single-particle resonance in the continuum channel as is demonstrated by the dip in the absorption curve, and the dramatic rise in the real phase shift. Figure 6-6 demonstrates the resonant-like behavior of the form factor for $\ell = 1$; initially the counterclockwise direction of the curve with increasing energy indicates this, but their behavior

Figure 6-5 Real phase shifts and absorption parameters, $\ell = 1$. Lisowski optical model parameters are used as discussed in text.

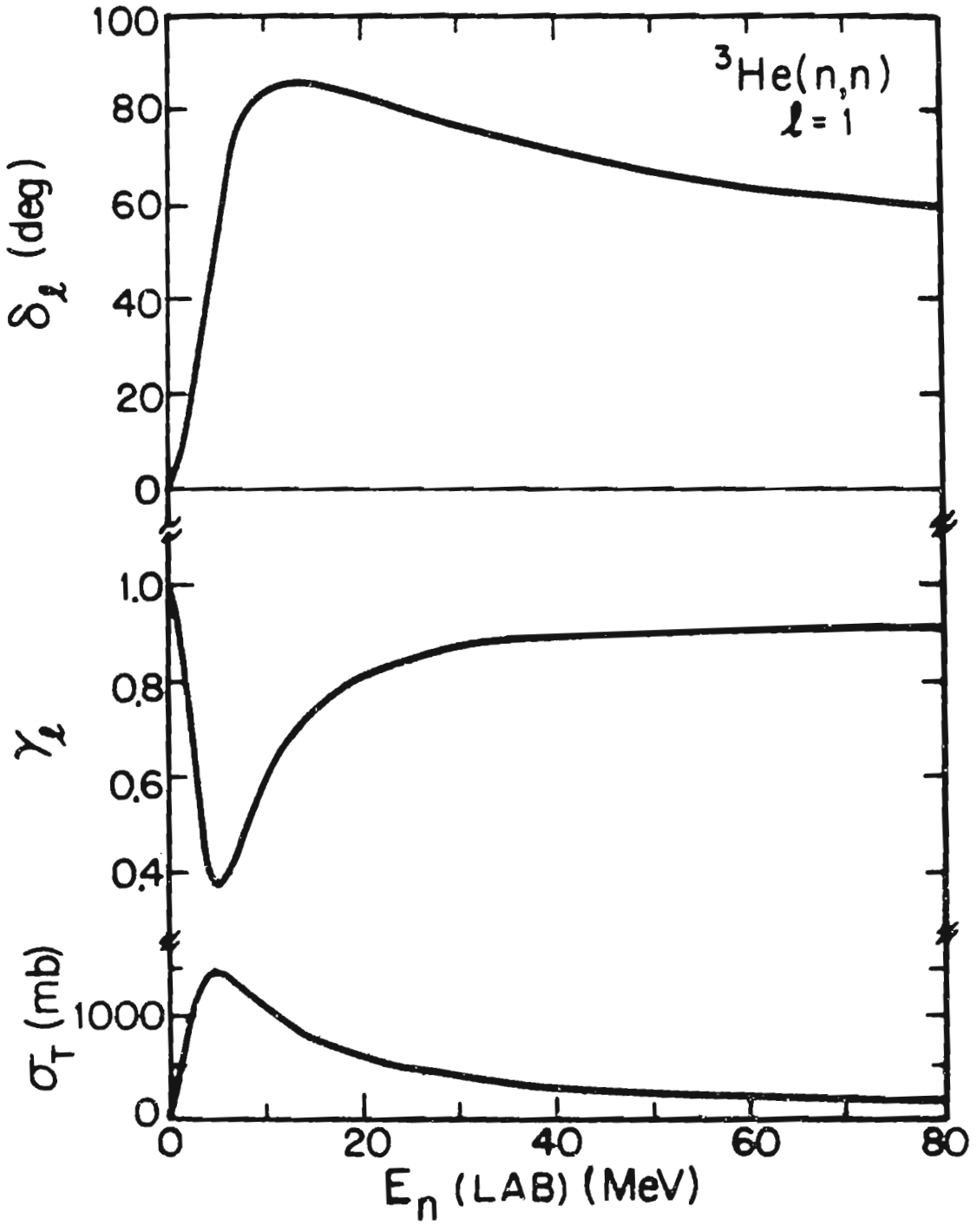
^{3}He(n,n)
$\ell = 1$
δ_ℓ (deg)
100
80
60
40
20
0
γ_ℓ
1.0
0.8
0.6
0.4
σ_T (mb)
1000
0
0
20
40
60
80
E_n (LAB) (MeV)

Figure 6-6 $\ell = 1$ n-^{3}He scattering amplitude in complex plane.

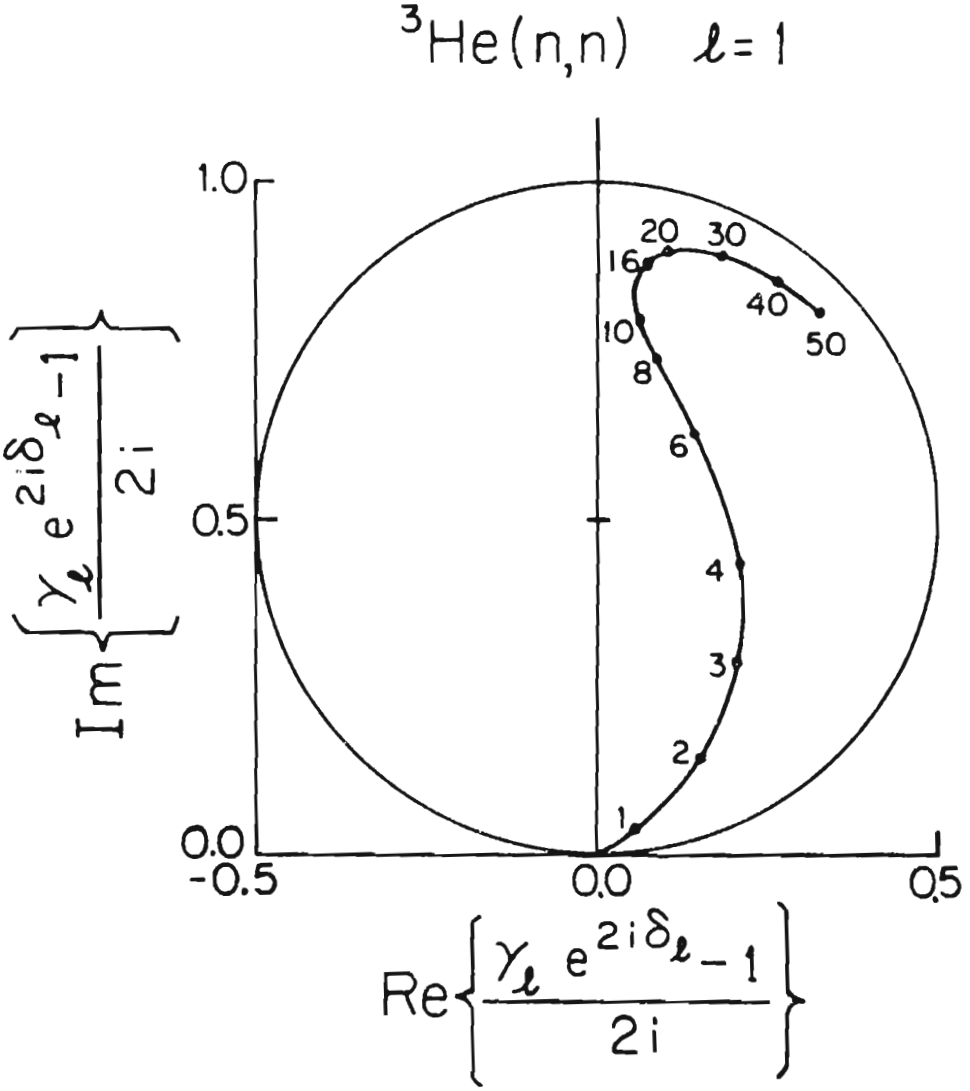
^{3}He(n,n) $\ell = 1$
1.0
0.5
0.0
-0.5
0.0
0.5
20
30
16
40
50
10
8
6
4
3
2
1
$\mathrm{Im}\left\{\frac{\gamma_\ell e^{2i\delta_\ell} - 1}{2i}\right\}$
$\mathrm{Re}\left\{\frac{\gamma_\ell e^{2i\delta_\ell} - 1}{2i}\right\}$

is overcome by the potential scattering at higher energies forcing the clockwise pattern. Similarly $\ell = 2$ waves exhibit this type of behavior with a much broader resonance-like shape centered near $E_p = 30$ MeV as is seen in figure 6-7. These results show that the direct capture model predicts a resonance like peak due to the single-particle resonance in the Optical potential describing the incident wave function.

6.2.2 Coupled channels calculation

While the direct mechanism is the simplest approach to understanding capture to ^{4}He, a two step mechanism incorporating the large (p,n) reaction cross section is a next step in describing the process. It has been demonstrated by Cotanch (1978) that a two-step charge exchange process can significantly compete with the one step single-particle direct capture process described earlier. He shows that for the case $^{16}O(\gamma,n_o)^{15}O$, the two-step process $^{16}O(\gamma,p)^{15}N(p,n)^{15}O$ plus direct can enhance the direct-only E1 cross section by ~ 30% in the region of the maximum cross section. It was felt that this might lead to a simple understanding of the (γ,p) to (γ,n) cross section ratio in ^{4}He. An effect which corrects the photodisintegration cross section by 30% could certainly produce the experimentally observed ratio if there were constructive interference in one reaction and destructive interference in the other reaction. Figure 6-8 shows schematically the difference in the two reactions. The two-step process first goes through a (γ,p) reaction to the isobaric analogue (^{3}H) of the residual nucleus (^{3}He), then through the (p,n) reaction to the final state. This charge exchange channel

Figure 6-7 Real phase shift and absorption parameter for $\ell = 2$.

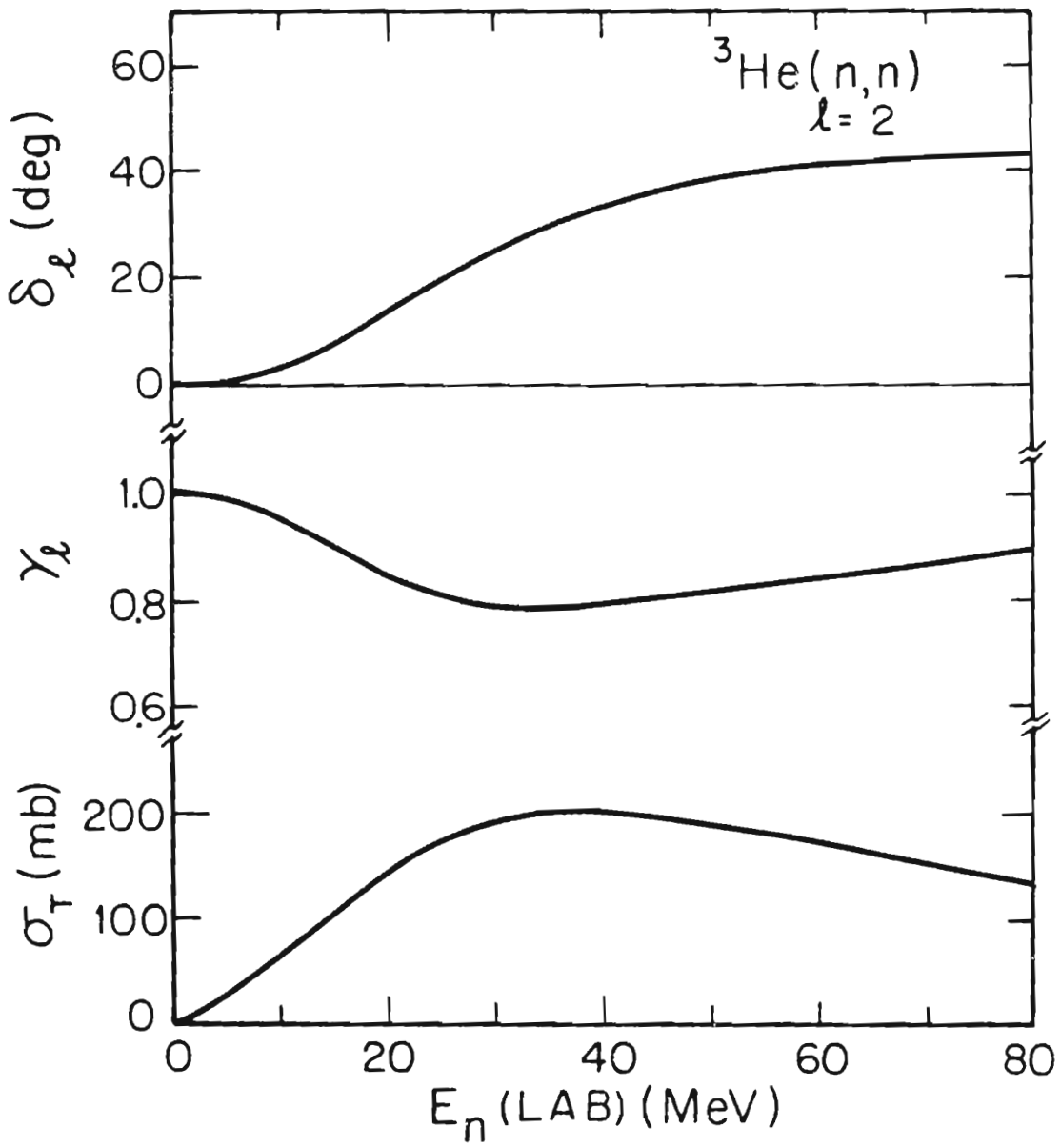
^{3}He(n,n)
ℓ = 2
δ_ℓ (deg)
60
40
20
0
γ_ℓ
1.0
0.8
0.6
σ_T (mb)
200
100
0
0
20
40
60
80
E_n (LAB) (MeV)

Figure 6-8 Schematic of two-step charge exchange process.

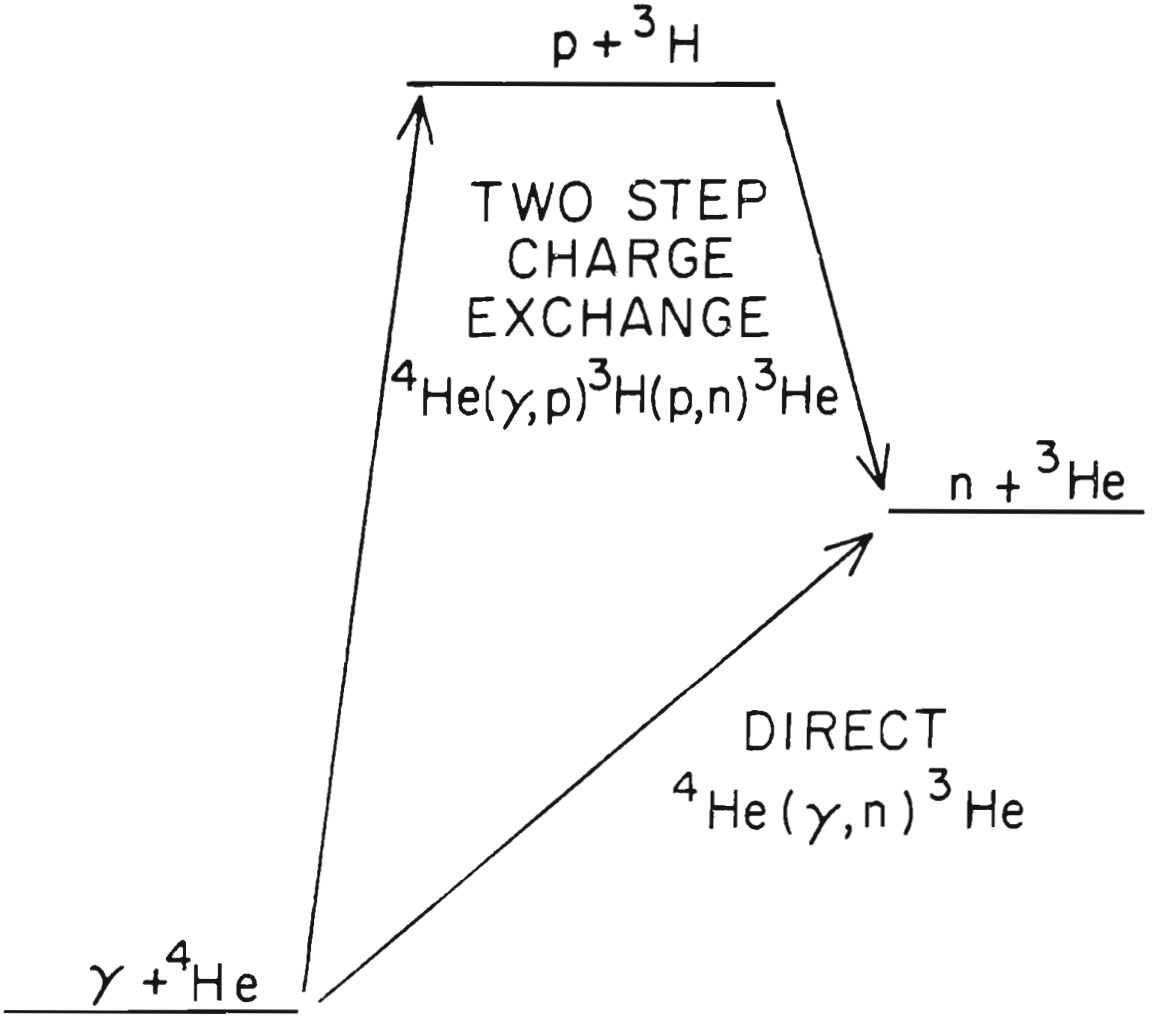
p + 3H
TWO STEP
CHARGE
EXCHANGE
4He(γ,p)3H(p,n)3He
n + 3He
DIRECT
4He(γ,n)3He
γ + 4He

allows the single particle nature of the direct calculation to be preserved. The Lane Model allows the (p,n) reaction to be parameterized within the framework of an optical model.

The calculations were performed (Hasan, 1981) using the code Excap with the same optical model parameters with the exception of the Lane model parameters V_1 = 25 MeV, r_1 = 1.25 and a_1 = 0.61 for the Lane potential which was of the form

$$V_1(r) = V_1 / [\ 1 + \exp(\frac{r-r_1}{a})\ ].$$

This well depth for the Lane potential is a reasonable estimate for heavier nuclei; it's applicability to the four nucleon system is uncertain. The large total $^3H(p,n)^3He$ cross section would argue for a large strength. The (p,n) cross section rises to ~500 mb at E_{pLAB} = 3 MeV (Drosg, 1978; Wilson, et al., 1961, and references therein). An analysis of p - ^{3}He and n - ^{3}H scattering optical models allows an estimate of the Lane potential for this (4 nucleon) system. (Podomore and Sherif, 1975; Sherif and Podomore, 1972; Sherif, 1979) Table 6-3 shows these parameters. The deduced Lane potential is V_1 = 0.6 MeV which seems too small to be consistent with the (p,n) cross section. Clearly a global fit of the (p,p), (n,n) and (p,n) scattering data should be performed to obtain a more consistent analysis.

Examination of figure 6-4 shows the effect of including the two step process. The shape of the calculated cross section is more nearly like that which experimentally observed than the direct only, but the ratio of the cross section for the two reactions is still

Table 6-3 Optical model parameters for scattering by A = 3 system.

	E_B	V_0	W_V	VSO
n - ^{3}H	9.0	47.36	1.49	2.47
p - ^{3}He	8.8	46.63	1.20	1.31

$r_0 = 1.488$ $r_i = 1.501$ $r_{SO} = 1.049$

$a_0 = 0.144$ $a_i = 0.378$ $a_{SO} = 1.049$

nearly unity. Inclusion of the two step process carries the calculation toward a more complete description of the experimental features, but fails to explain the ratio of the (γ,p) to (γ,n) cross section.

6.2.3 Shell model

Most recent theoretical approaches to the photodisintegration of ^{4}He have been in the form of continuum-recoil-corrected shell model calculations. (Halderson and Philpott, 1979; Delsanto et al., 1977; Chung et al., 1974) Londergan and Shakin, 1972). While they have been successful in reproducing some experimental aspects of this reaction, they fail to produce a ratio of photoproton to photoneutron cross sections much different from unity. That the ratio has not been more fully investigated is understandable in light of the experimental uncertainty which has surrounded this issue. Recently, a continuum shell model calculation was carried out by Delsanto (1981) with the intention of investigating the sensitivity of the photoproduction cross sections to various shell model parameters. The calculational technique was that of the natural boundary condition method (eigenchannel technique) with special procedures to select and remove the spurious center-of-mass states. (Delsanto et al., 1977)

In this shell model calculation, the nuclear potential parameters were adjusted to reproduce the experimenatally observed levels which correspond to the single-particle levels. Due to the broad nature of these levels in the case of ^{4}He, there is an uncertainty in their position to the extent that this usually definitive technique breaks down. The s1/2 oscillator level is observed as the ground state of

^{4}He; p-shell states are found in the A+1 nuclei ^{5}Li and ^{5}He for the proton and neutron well respectively. The level energies are observed relative to the unbound energy of the last nucleon. In the case of the s1/2 neutron state the level energy is the separation energy of ^{3}He-n, $(SE)_n$ = 20.578 which is a well-defined energy. Level energies for the p-shell states are not so well defined, as can be seen in Figure 6-9, which shows these levels relative to the unbound system. The ground state and first excited state of ^{5}Li and ^{5}He match the $p_{3/2}$ and $p_{1/2}$ single-particle levels. The first excited state of these nuclei are extremely broad. Particularly uncertain, however, is the first excited state in ^{5}Li.

For heavier nuclei, this technique of adjusting well parameters, primarily the well depth, to obtain the experimental spectrum produces a unique, well-defined set of parameters, and in fact the well depth for the protons is not generally equal to the well depth for neutrons. In the case of ^{12}C the observed levels in ^{13}C and ^{13}N are very narrow in width. To reproduce their spacing, the Woods-Saxon strengths for neutrons and protons differ by 2 MeV.

Levels in ^{5}He and ^{5}Li do not provide such a definitive test of the potential parameters. Their broad nature and uncertain position allow a variation in the parameters which would not be possible in most other nuclei. The investigation which has been carried out is intended to demonstrate the sensitivity of the ratio of the two-body photoproduction cross section to these parameters. Table 6-4 shows the parameters which were varied and the corresponding single-particle levels which can be compared to the experimentally observed levels.

Figure 6-9 Experimentally observed single-particle levels in ^{4}He well.

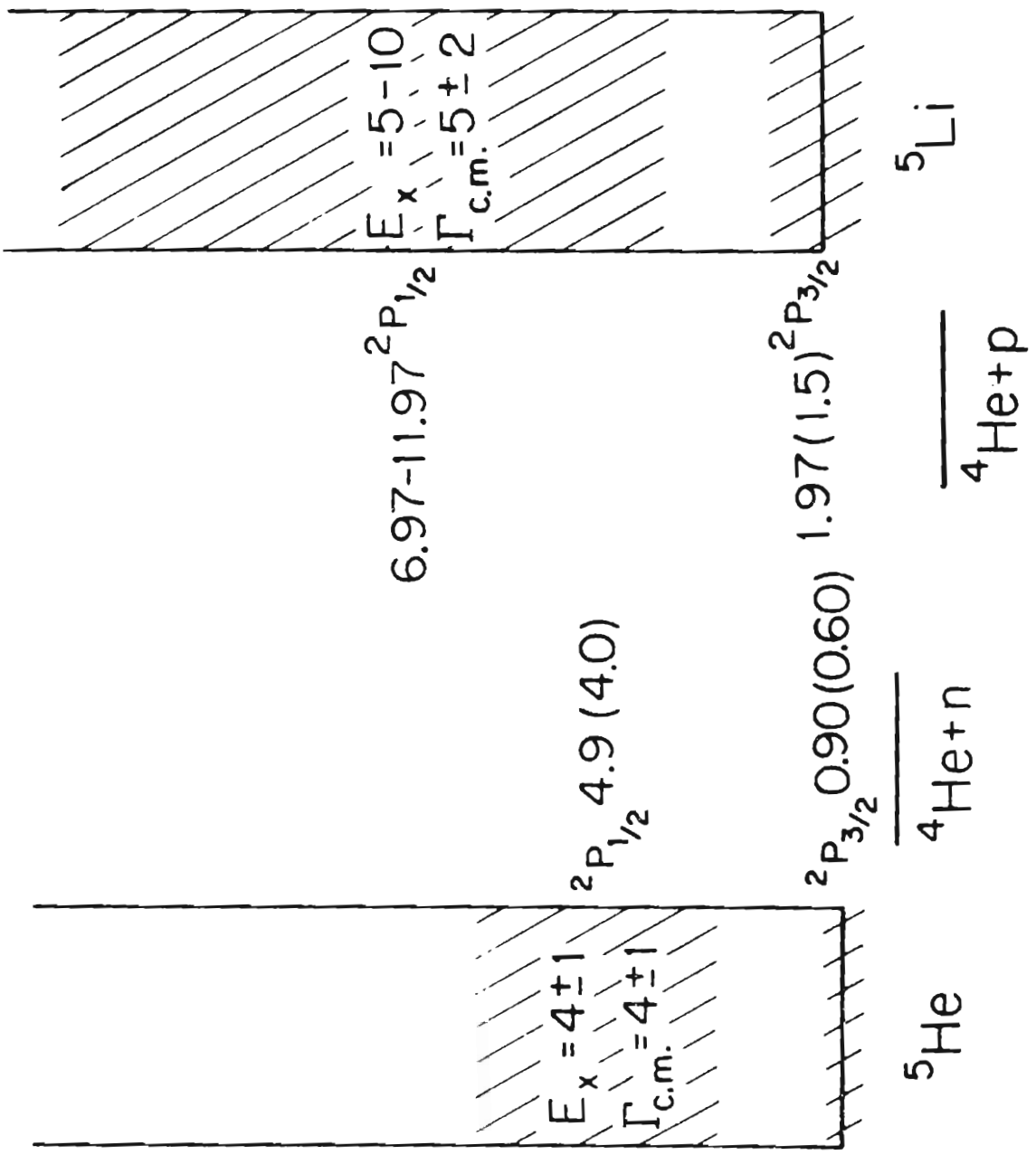
E_x =5-10
$\Gamma_{c.m.}$=5±2
6.97-11.97 $^2P_{1/2}$
1.97(1.5) $^2P_{3/2}$
^{5}Li
^{4}He+p
$^2P_{1/2}$ 4.9 (4.0)
$^2P_{3/2}$ 0.90(0.60)
^{4}He+n
E_x =4±1
$\Gamma_{c.m.}$=4±1
^{5}He

Table 6-4 Shell Model parameters and corresponding calculated single particle levels. Lower case letters on the left denote calculated (γ,p) to (γ,n) cross section ratios as indicated in figure 6-10. The form of the potential and notation are defined in Delsanto (1977).

	s State Energies		Woods-Saxon Well Depth	
	Proton	Neutron	Proton	Neutron
	$s_{1/2}$	$s_{1/2}$	U_0	U_0
	-19.84	-20.54	-58.17	-58.17

	p State Energies				Woods-Saxon Well Depth	
	Proton		Neutron		Proton	Neutron
	$p_{3/2}$	$p_{1/2}$	$p_{3/2}$	$p_{1/2}$	U_0	U_0
a	1.9	4.4	1.3	4.0	-62	-62
b	3.1	4.7	1.3	4.0	-57	-62
b	1.9	4.4	-0.3	3.4	-62	-67
c	1.9	4.4	-2.5	2.5	-62	-72

$R_0 = 2$ fm d = 0.25 fm

$\gamma = 12$

Residual Interaction

$V_0 = -600$ Mev fm^3 $a_0 = 0.7$ $a_\sigma = 0.3$

Matching Radius a = 10 fm

The $s_{1/2}$ levels (neutron and proton) are reproduced with the same value of the well depth, their energy difference is accounted for by the Coulomb potential. Changes in the p-state potential produce sizable effects in the ratio of the photoproton to photoneutron cross section. The values for this ratio which are produced are shown in figure 6-10. The Woods-Saxon parameters are indicated via the lower case letters which also appear on the left-hand side of table 6-4. A 5 MeV difference in the proton or neutron well changes the ratio by 60%, while the calculated levels in the A = 5 nuclei are reasonably well reproduced. Therefore the statements that have been made concerning the inability of a shell model calculation to produce a ratio much different than unity must be qualified. It is not unreasonable to adjust the well depths by several MeV and that is all which seems to be required to produce this higher value of the ratio. In fact, adjustments of this nature may very well be necessary to account for the inability of this model to describe the interaction of a 4-nucleon system. The Coulomb potential surely must deviate from a spherical geometry as is assumed. These differences in well depths may be due to isospin mixing. Whatever the mechanism, this calculation serves to parameterize the observed ratio.

Figure 6-10 Shell model predictions of ratio, $R = \sigma_T(\gamma, p_0) \; / \; \sigma_T(\gamma, n_0)$. Various well parameters were used in the calculation and are indicated by the lower-case letters which are explained in table 6-5.

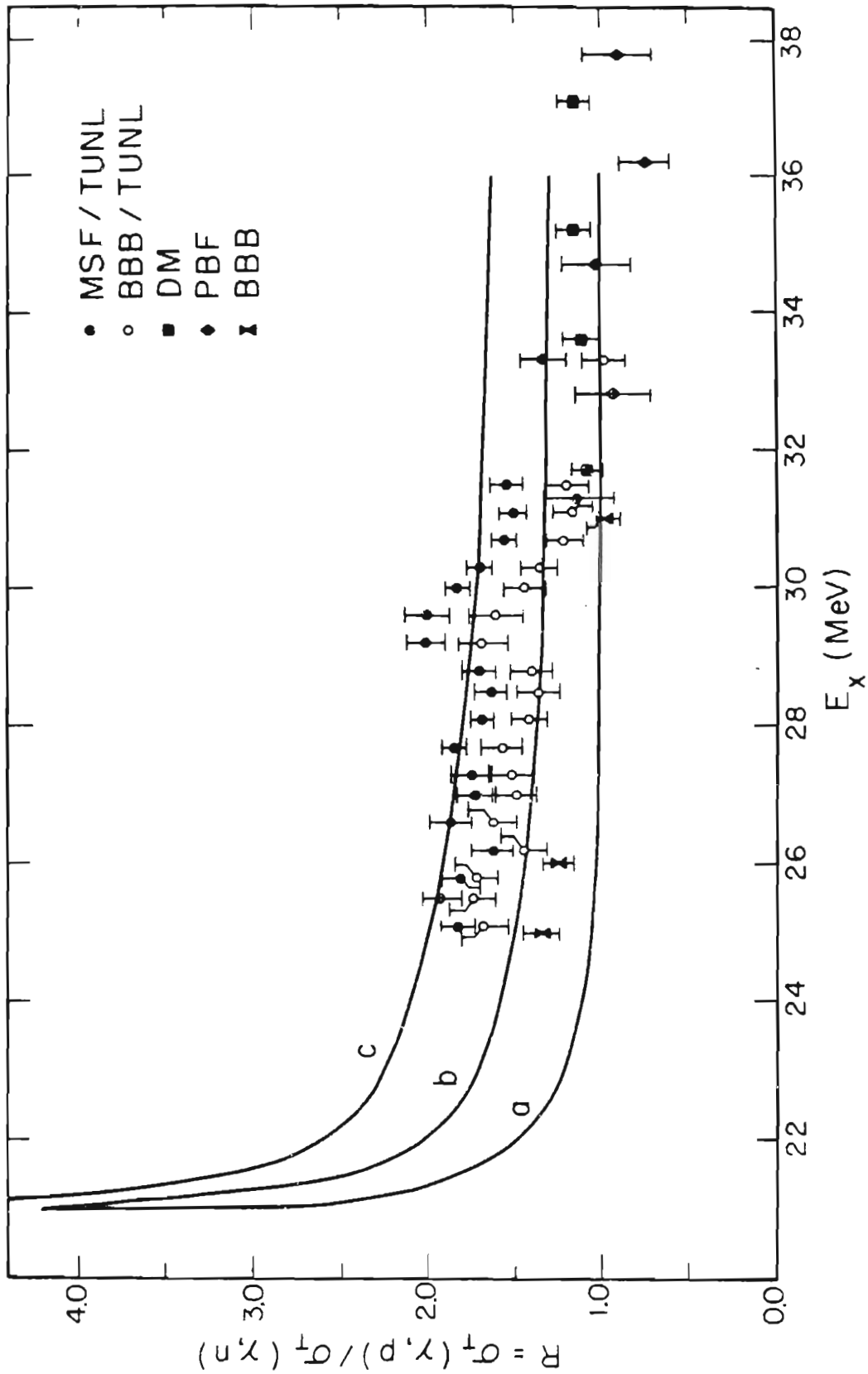
MSF / TUNL
BBB / TUNL
DM
PBF
BBB
a
b
c
$R = \sigma_T(\gamma,p)/\sigma_T(\gamma,n)$
E_x (MeV)
0.0
1.0
2.0
3.0
4.0
22
24
26
28
30
32
34
36
38

6.3 Isospin Mixing in ^{4}He

It is very tempting to extrapolate the data represented in figure 1-1 to a value of ~1 for the case of ^{4}He (A = 4). Particularly so, if the explanation of the monotonic increase of R as based on the observation that the Coulomb potential, hence mixing, increases with A. As mentioned earlier, the Coulomb potential is additive over the Z protons since it acts over a long range. If the Coulomb interaction is ruled out as a mechanism for producing an isospin mixing in ^{4}He which would produce a value of R = 1.6; this leads to the conclusion that it is produced by some asymmetry in the nucleon-nucleon short range interaction. In particular, recent arguments that the Coulomb interaction is not sufficiently strong enough to produce isospin mixing of the excited state wave functions seem compelling but are some what over stated. Using the formalism of Barker and Mann (equation (1.1)) a ratio R = 1.6 implies a T = 0 impurity of $\left| \frac{\alpha_0}{\alpha_1} \right| \simeq 0.014$. If first order perturbation theory applies then the Coulomb matrix element is determined by

$$\frac{|\alpha_0|}{|\alpha_0|} = \frac{|V_C|}{[(E_0 - E_1)^2 + \frac{\Gamma^2}{4}]^{1/2}}$$

Where E_0, E_1 are the energies of the T = 0,1 states with width, Γ which are mixed via the potential V_c. In this case, a Coulomb potential V = 0.5 MeV is required, which seems to be quite a large

mixing matrix element. However, there are several points which must be discussed. First order perturbation theory is not appropriate since these levels are not narrow well separated levels. It has been shown in the case of α capture that broad underlying T = 0 strength produces large isospin mixing as is reviewed by Segel (1966). A more appropriate calculation based on reasonable estimates of these wave functions needs to be performed.

There are examples of calculations in which the Coulomb perturbation is shown to produce mixing matrix elements of the order needed as in the case of ^{12}C and ^{16}O (Sato, et al., 1977; Castel, et al., 1980) In the case of ^{12}C, the authors invoke a Charge Symmetry Breaking (CSB) component of the nuclear Hamiltonian, but its matrix element is only 39 keV, much smaller than that due to the dominant one body Coulomb interaction. A three-level mixing model is involved in the ^{16}O calculations, producing a Coulomb matrix element of 150 keV. Table 6-5 allows a comparison of the states which are mixed, their characteristics and the mixing matrix elements which are deduced. The three-level calculations is appealing in the case of ^{4}He since there are three 1^- states in the GDR region. Gibson (1981) has remarked that a three-level mixing model is probably required to transfer the decay strength to the (γ,p) channel over the entire range as is observed experimentally. A two-level-mixing calculation would produce an interference-like effect in which the ratio is greater than unity on one side and less than unity on the other side of the average excitation energy. A shell-model based calculation of the energy-integrated cross section was performed by Gibson (1972) which,

Table 6-5 Isospin-mixed levels in ^{4}He, ^{12}C and ^{16}O.

	J^{π}, T, E_X	Γ/D	$\lvert \alpha_0/\alpha_1 \rvert$	V_C (EXP) (keV)	V_C (CONV) (keV)	V_{10} (keV)
^{4}He	1-, 1, 27.4	> 1	0.12	200 - 500	< 100	
	1-, 1, 30.5					
	1-, 0, 31.0					
^{12}C	1+, 0, 12.71	0.02	0.12	110 - 180	60	170
	1+, 1, 15.11					
^{16}O	2-, 1, 8.88	0.004	0.07	120 - 300	40 - 60	200
	2-, 0, 12.53					
	2-, 1, 12.97					

in fact, yields a ratio of ~1.6, but seems to handle the interference of the S = 0 and S = 1 wave functions improperly. It is quite possible that a detailed calculation which uses proper wave functions and handles the interference correctly will offer an explanation of the experimentally observed ratio.

7 SUMMARY

The ninety degree cross section was measured for bombarding energies of E_n = 6 to 18 MeV, corresponding to excitation energies of 24 to 34 MeV. From these data an integrated photoneutron cross section was inferred which is in agreement with a recent total photoneutron measurement, indicating that the photodisintegration cross section has a value of 1 mb from 24 to 34 MeV. Comparison of these results to the experimental photoproton cross section indicates that the value of the neutron cross section is significantly lower than the proton cross section below E_γ = 30 MeV in ^{4}He. This is contrary to the prediction of reaction theories as applied to these reactions. The experimentally determined ratio has a value of 1.6 at E_γ = 28 MeV while most theoretical predictions indicate that it is near 1.0 above about 24 MeV.

A seven-point angular distribution of cross section and a three-point angular distribution of polarization asymmetry were measured at E_n = 9 (E_γ = 28.1) MeV. These distributions were fit to Legendre and associated Legendre polynomials respectively. They were also used to obtain the amplitudes and relative phases of what are expected to be the three dominant transition matrix elements. This analysis indicates that a similar relative E2 strength is present in

the neutron and the proton channels. Within the large error the relative spin-flip E1 strength is also the same. The indication is that the total cross sections are not equal, but that the relative amount of these smaller components is the same for the two reactions.

To gain an understanding of this result, comparison was made to several model dependent calculations. The direct photodisintegration model predicts near equality for the cross sections of the two channels, and equal E1 spin-flip amplitudes. The E2 ($^1D_2$) relative cross section which it predicts is much smaller than experiment for both channels. A second step in calculating these cross sections was in the form of a coupled channels calculation which incorporates a competing direct plus charge exchange mechanism in the calculation. This modifies the shape of the cross section, but the ratio is still near unity. The third comparison was intended to demonstrate the variability in applying a shell model calculation to this system within the confines of standard techniques. A calculation was presented in which the Woods-Saxon parameters were varied, producing sizable effects in the cross section ratio. This calculation has apparently put the observed difference into a more fundamental form, namely a difference in the potential well depth for neutrons and protons in ^{4}He. The physical origin of this difference remains to be accounted for from first principles.

In conclusion, the seemingly straight-forward approach to understanding this relatively simple system fails to reproduce the experimentally observed cross section ratio. Incorporation of charge-exchange effects in the coupled-channels and standard shell

model calculations also fail. Within the structure of this simple system lies this enigmatic phenomenon for which a different theoretical approach must be taken, an approach in which the peculiarities of this system are handled correctly: a) the few number of nucleons, b) the broad nature of the so-called states and c) the high excitation energy. These affect the way in which one must understand the structure. The low number of nucleons affects the shape of the potentials, hence the wave functions of the neutron or proton outside the 'core'. The broad nature of the states limits the approximations which may be made concerning them. Their unbound nature dictates a behavior in which the long-range Coulomb interaction certainly plays an extremely significant role in the interaction of the last nucleon with the core. The application of the conventional isospin formalism becomes a risky one. Perhaps it would not be surprising for a high degree of mixing to occur due solely to Coulomb effects when they are treated properly. Whatever the origin of the ratio having this large value, the investigation of this phenomenon should lead to a greater understanding of the structure of nuclei and the approximations of conventional nuclear structure calculations.

Bibliography

Arkatov, Yu. M., P. I. Vatset, V. I. Voloshchuk, V. V. Kirichenko, I. M. Prokhorets and A. F. Khodyachikh, 1970, Sov. J. Nucl. Phys. 10 639.

Arkatov, Yu. M., P. I. Vatset, V. I. Voloshehuk, V. N Gur'ev V. A. Zolenko, I. M. Prokhorets and V. I. Chmil', 1976, Sov. J. Nucl. Phys. 21, 475.

Arkatov, Yu. M., P. I. Vatset, V. I. Voloshehuk, V. N Gur'ev and A. F. Khodyachikh, 1978, Ukr. Fiz. Zh. 23, 1818.

Balestra, F., E. Boilini, L. Basso, R. Garfagnini, C. Guarldo, G. Piragino, R. Scrimaglio and A. Zanini, 1977, Il Nuovo Cimento A38 145.

Barkas, W. H. and M. J. Berger, 1964, Nat. Res. Council Pub. 1133, and Nucl. Sci. Series Rept. 39, 103.

Barker, F. C. and A. K. Mann, 1957, Phil. Mag. 2, 5.

Berman, B. L., S. C. Fultz and M. A. Kelly, 1971, Phys. Rev. C 4, 723; Phys. Rev. Letters 25, 938.

Berman, B. L., F. W. K. Firk and C. P. Wu, 1792, Nucl. Phys. A179, 791.

Berman, B. L., D. D. Faul, P. Meyer, D. L. Olson, 1980, Phys. Rev. C 22, 2273.

Bevington, Philip R., in Data Reduction and Error Analysis for the Physical Sciences, 1969, (McGraw-Hill, New York), 200.

Braker, W., and A. L. Mossman, 1971, "Matheson Gas Data Book," 5th ed., 278.

Brown, G. E., L. Castillejo and J. A. Evans, 1961, Nucl. Phys., 22, 1.

Busso, L., R. Garfagnini, G. Piragino, S. Ronchi della Rocca, A. Zanini, 1971, Lettere al Nuovo Cimento 1, 941.

Buttlar, Haro von, 1968, in Nuclear Physics, an Introduction, (Academic Press, New York) pp. 410, 411.

Castel, B., R. Y. Cusson and L. Zamick, 1980, Nuclear Physics A341, 93.

Chung A. H., R. G. Johnson and T. W. Donnelly, 1974, Nucl. Phys. A235, 1.

Clegg, T. B., G. A. Bissenger and T. A. Trainor, 1974, Nucl. Instr. and Methods 120, 445.

Clerc, H. G., R. J. Stewart and R. C. Morrison, 1965, Phys. Letts. 18, 316.

Cotanch, S. R., 1978, Physics Letters 76B, 19.

Cotanch, S. R., 1979, Private Communication. Delsanto, P. P. 1981, private communication.

Delsanto, P. P., A. Pompei and P. Quarati, 1977, Journal of Phys. G 3, 1133.

Detch, Jr., J. L., R. L. Hutson, Nelson Jarmie, and J. H. Jett, 1971, Phys. Rev C 4, 52.

Dixon, D., 1960 in "Nuclear Forces and the Few-Nucleon Problem," ed. by T. C. Griffith and E. A. Power (Pergamon,New York), p. 295.

Dodge W. R. and J. J. Murphy, 1972, Phys. Rev. Letters 28, 839.

Drosg, M., 1978, Nuc. Sci. and Eng. 67, 190.

Eisenberg, J. M. and W. Greiner, 1970, Excitation Mechanisms of the Nucleus, (North-Holland, Amsterdam) p. 100.

Elliot, J. P. and B. H. Flowers, 1957, Proc. Roy. Soc. (London), A242, 57.

Ferguson, G. A., J. Halpern, R. Nathans and P. F. Yergin, 1954, Phys. Rev. 95, 776.

Ferrero, F., C. Manfredotti, L. Pasqualini, G. Piragino, P. G. Rama, 1966, Nuovo Cimento 45B, 273.

Feshbach, H., 1960, in Nuclear Spectroscopy, Part B, edited by Fay Ajzenberg-Selove, (Academic Press, New York), p. 628.

Fiarman, S. and W. E. Meyerhof, 1973, Nuclear Physics A206, 1.

Flowers, B. H. and F. Mandl, 1950, Proc. Roy. Soc. A206, 131.

Fuller, E. G., 1954, Phys. Rev. 96, 1306.

Fuller, E. G. and Evans Hayward, 1962, in Nuclear Reactions, Vol. 2, edited by P. M. Endt and P. B. Smith, (North-Holland, Amsterdam), p. 144.

Gardner, C. C., and J. D. Anderson, 1962, Phys. Rev. 125, 626.

Gemmel, D. S. and G. A. Jones, 1962, Nucl. Phys. 33, 102.

Gibson, B. F., 1972, Nucl. Phys. A195, 499.

Gibson, B. F., 1981, Nucl. Phys. A353, 85c.

Gorbunov, A. N. and V. M. Spiridonov, 1958, Sov. Phys. JETP 34, 596; 1958, Sov. Phys. JETP 6, 1958.

Gorbunov, A. N., 1968, Phys. Letts. 27B, 436.

Gorbunov, A. N., 1974, Proc. of P. N. Lebedev Phys. Inst. 71, 1.

Gunn, J. C. and J. Irving, 1951, Phil. Mag. 7-42, 1353.

Halderson, D. and R. J. Philpott, 1979, Phys. Rev. Lett. 42, 36.

Hanna, S. S., 1969, in Isospin in Nuclear Physics, ed. by D. H. Wilkinson, (North-Holland, Amsterdam), p. 591. Hasan, H., 1981, Private communication.

Irish, J. D., R. G. Johnson, B. L. Berman, B. J. Thomas, K. G. McNeill, and J. W. Jury, 1975, Can. J. Phys. 53, 802; 1973, Phys. Rev. C 8, 433.

Jackson, J. J., 1961, Classical Electrodynamics, 1st ed., John Wiley and Sons, New York, p. 401.

Jensen, M., 1980 private communication and 1980, TUNL Annual Report, p. 100.

Kankowsky, R., (unpublished Ph. D. dissertation, University of Erlangen-Nurnberg, 1972.)

King III, G. 1978, (unpublished Ph. D. Thesis, Stanford University).

King, S. E., N. R. Roberson, and S. A. Wender, 1981, Bull. Am. Phys. Soc. 26, 90.

Kinney, W. E., 1970, Nucl. Inst. and Methods 83, 15.

Lisowski, P. W., 1973, (Unpublished Ph. D. dissertation, Duke University)

Lisowski, P. W., R. L. Walter, C. E. Busch, T. B. Clegg, 1975, Nucl. Phys. A242, 298.

Londergan, J. T. and C. M. Shakin, 1972, Phys. Rev. Lett. 28, 1729.

Malcom, C. K., D. V. Webb, Y. A. Shin and D. M. Skopic, 1973, Phys. Lett. 47B, 433.

Marrs, R. E., E. G. Adelberger, K. A. Snover, M. D. Cooper, 1975, Phys. Rev. Lett. 35, 202.

McBroom, R. C., (1977, unpublished Ph. D. dissertation, University of Florida)

McBroom, R. C., H. R. Weller, S. Manglos, N. R. Roberson, S. A. Wender, D. R. Tilley, D. M. Skopik, L. G. Arnold and R. G. Seyler, 1980, 45, 243.

Meyerhof, W. E., Martin Suffert, and William Feldman, 1970, Nucl. Phys. A148, 211.

Milone, C., 1960, Phys. Rev. 120, 1302.

Ohlsen, G. G., 1970, Los Alamos Scientific Laboratory Report, LA-4451.

Perry, Jr., J. E. and J. S. Bame, Jr., 1955, Phys. Rev. 99, 1368; 1953, Phys. Rev. 90, 380.

Phillips, T. W., B. L. Berman and D. D. Faul, 1979, Phys. Rev. C 19, 2091.

Podomore, B. S., and H. S. Sherif, 1975, in "Few Body Problems in Nuclear and Particle Physics," ed. by R. J. Slobodrian, B. Cujec and K. Ramavataram (Laval Univ. Press, Quebec City, Canada), p. 517.

Sanada, J., M. Yamanouchi, N. Sakai and S. Seki, 1970, J. Phys. Soc. Japan 28, 573.

Sato, H. and L. Zamick, 1977, Phys. Lett. 70B, 285.

Segel, R. E., 1966, in Isobaric Spin in Nuclear Physics, ed. by D. Fox and Donald Robson, p. 194.

Seyler, R. G. and H. R. Weller, 1979, Phys. Rev. C 20, 453.

Sherif H. S. and B. S. Podomore, 1972, "Few Particle Problems in the Nuclear Interaction," ed. by I. Slaus, S. A. Moskowski, R. P. Haddock and W. T. H. Van Oers, (North Holland, Amsterdam), p. 691.

Sherif, H. S., 1979, Phys. Rev. C 19, 1649.

Storm, Ellery and Harvey I. Israel, 1970, Nucl. Data Tables A7, 565.

Tornow, W., E. Woye, G. Mack, R. L. Walter, C. E. Floyd, P. P. Guss and R. C. Byrd, 1981, "Small-Angle Neutron Polarization for the $^{2}H(d,n)^{3}He$ Reaction Near 8 MeV" Accepted for publication in Nucl. Inst. and Meth.

Turner, J. D., 1978 (Unpublished Ph. D. dissertation, Duke University

Walter, R. L., 1979, private communication.

Warburton, E. K. and J. Weneser, 1969, in Isospin in Nuclear Physics ed. by D. H. Wilkinson, (North-Holland, Amsterdam), p. 174.

Weller, H. R. and N. R. Roberson, 1980, Rev. of Mod. Phys. 52, 699.

Wender, S. A., N. R. Roberson, M. Potokar, H. R. Weller and D. R. Tilley, 1978, Phys. Rev. Letts. 41, 1217.

Wilson, W. E., R. L. Walter and D. B. Fossan, 1961, Nucl. Phys., 27, 421.

Zurmühle , R. W., W. E. Stephens and H. H. Staub, 1963, Phys. Rev. 132 751.